EXAFS Study of Amorphous Selenium

A Thesis Submitted to the

College of Graduate Studies and Research

in Partial Fulfillment of the Requirements

for the degree of Master of Science

in the Department of Physics and Engineering Physics

University of Saskatchewan

Saskatoon

By

John A. McLeod

Permission to Use

In presenting this thesis in partial fulfilment of the requirements for a Postgraduate degree from the University of Saskatchewan, I agree that the Libraries of this University may make it freely available for inspection. I further agree that permission for copying of this thesis in any manner, in whole or in part, for scholarly purposes may be granted by the professor or professors who supervised my thesis work or, in their absence, by the Head of the Department or the Dean of the College in which my thesis work was done. It is understood that any copying or publication or use of this thesis or parts thereof for financial gain shall not be allowed without my written permission. It is also understood that due recognition shall be given to me and to the University of Saskatchewan in any scholarly use which may be made of any material in my thesis.

Requests for permission to copy or to make other use of material in this thesis in whole or part should be addressed to:

Head of the Department of Physics and Engineering Physics
116 Science Place
University of Saskatchewan
Saskatoon, Saskatchewan
Canada
S7N 5E2

Abstract

An overview of synchrotrons and synchrotron radiation is presented, along with the theory and practical considerations behind several types of X-ray spectroscopy. The theory and practical considerations of density functional theory are also given, with direct reference to some specific software packages.

Some synchrotron-excited X-ray spectroscopy measurements and density functional theory calculations of selenium and arsenic-doped selenium films are then outlined. The physical structure of crystalline and amorphous selenium and the electronic structure of amorphous selenium are discussed and comparison is made to the experimental results.

A weak feature in the conduction band is identified as a "fingerprint" of the degree of crystallization in amorphous selenium from X-ray absorption measurements. Similarly, a weak feature corresponding to lone-pairs in the valence band is identified as a "fingerprint" of the arsenic concentration from X-ray emission measurements.

Finally a detailed model of the structure of amorphous selenium is explained, and compared to experiment. This model is tested both by direct calculations and by a reverse Monte Carlo approach. The implications of this model with respect to the structure of amorphous and arsenic-doped amorphous selenium are discussed. Calculations suggest that simply randomizing the arrangement of "perfect" trigonal selenium is unable to reproduce the measurements of amorphous selenium; a moderate variation in the bond angle of "perfect" trigonal selenium is also necessary.

Acknowledgements

I would like to gratefully acknowledge my thesis supervisor, Dr. Alexander Moewes, for his support and guidance. I would also like to thank Dr. Safa Kasap and Dr. Robert Johanson of the Electrical Engineering Department for their assistance, and in particular thank Dr. George Belev and Dr. Dan Tonchev, also of the Electrical Engineering Department, for fabricating the samples used in this research.

I would like to acknowledge all the members of the Beamteam for their assistance given during the measurements, and the advice given during numerous fruitful discussions.

I am grateful for the help of Ning Chen, of the Canadian Light Source, for his tireless assistance in helping me take measurements at the Hard X-ray Microprobe Analysis beamline.

I would also like to thank Dr. Alex Kolobov of the National Institute for Advanced Industrial Science and Technology (Japan) for his advice and helpful discussions about my research.

This project was supported by funding from the National Science and Engineering Research Council (NSERC), the Canada Research Chair program, and the Anrad Corporation (www.anrad.com). Some of the research was performed at the Advanced Light Source at the Lawrence Berkeley National Laboratory. The Advanced Light Source is supported by the Director, Office of Science, Office of Basic Energy Sciences, of the U.S. Department of Energy under Contract No. DE-AC02-05CH11231. The bulk of the research described in this thesis was performed at the Canadian Light Source, which is supported by NSERC, the National Research Council (NRC), the Canadian Institutes of Health Research (CIHR), and the University of Saskatchewan.

Contents

List of Tables

List of Figures

List of Abbreviations

ALS	Advanced Light Source
APW	Augmented Plane Wave
aSe	Amorphous Selenium
BL8	Beamline 8.0.1
CLS	Canadian Light Source
cSe	Crystalline Selenium
DCXID	Direct Conversion X-ray Imaging Detector
DFT	Density Functional Theory
DOS	Density of States
EXAFS	Extended X-ray Absorption Fine Structure
FPXID	Flat Panel X-ray Imaging Detector
GTO	Gaussian Type Orbitals
HXMA	Hard X-ray Microprobe Analysis
LAPW	Linearized Augmented Plane Wave
LCAO	Linear Combination of Atomic Orbitals
LO	Local Orbital
mSe	Monoclinic-phase Selenium
pSe	Polycrystalline Selenium
RMC	Reverse Monte Carlo
SGM	Spherical Grating Monochromator
SXF	Soft X-ray Fluorescence
SXS	Soft X-ray Spectroscopy
tSe	Trigonal-phase Selenium
TEY	Total Electron Yield
TFY	Total Fluorescence Yield
UHV	Ultra High Vacuum
UPS	Ultra-violet Photoemission Spectroscopy
VLS-PGM	Variable Line Spacing - Planar Grating Monochromator
XANES	X-ray Absorption Near Edge Structure
XAS	X-ray Absorption Spectroscopy
XES	X-ray Emission Spectroscopy
XPS	X-ray Photoemission Spectroscopy
XRD	X-ray Diffraction

Chapter 1

Introduction

Amorphous selenium (aSe) is a well known photoconductive chalcogenide, and the inherent ability of aSe to generate charge carriers under exposure to X-rays has been known for quite some time [1–3]. Research into the electronic and opto-electronic properties of aSe has been the subject of continuous interest for many years [4–9]. Indeed, the first commercial application of aSe was for xerography (photocopying), which occurred in the early 1950s [10, 11]. However it was only recently that aSe found commercial application in direct conversion X-ray image detectors (DCXIDs) for medical use [12]. One of the sponsors of my research, the Montreal-based Anrad Corporation, is a world leader in flat-panel X-ray detectors and currently manufactures five different models for mammography and real-time imaging (fluoroscopy) [13, 14]. Compared to conventional X-ray imaging equipment which typically use phosphor films, aSe DCXIDs have greater portability, offer real-time X-ray imaging, and have higher resolution [15]. In aSe, as with any direct conversion photoconductor, ultrahigh resolution is possible since the photoelectrons created by the X-rays travel directly to a pixel read-out [15]. In a phosphor or column channel detector the heterogeneous nature of the material causes significant lateral dispersion of the photoelectrons before they are read by the pixel array [16, 17]. In aSe the resolution is limited mainly by quality control of the bulk aSe material [18]. Current commercial detectors made by Anrad have resolutions of 85 μm [19], but in principal resolutions as good as 2 μm could be obtained [16]. Figure 1.1 shows the Anrad SMAM, a 17 cm $\times$ 24 cm flat panel DCXID for digital mammography.

Besides the amorphous phase, selenium at ambient temperatures has two crystalline (cSe) phases: trigonal (tSe) and monoclinic (mSe). The former phase is often

Figure 1.1: Anrad SMAM DCXID for digital mammography (Figure from www.anrad.com).

referred to as "grey" or "metallic" selenium [20] due to its appearance. tSe is not actually metallic, however; it has a bandgap of ∼1.5 to 2 eV [5,21]. The latter phase is often referred to as as "red" selenium [20]. tSe is formed of a helical arrangement of Se_∞ chains [22], and mSe is formed of Se_8 rings. Technically there are (at least) three crystalline arrangements of mSe, termed the α-, β-, and γ-phases [23]. These three phases are essentially the same [24], the only difference being subtle changes in the Se_8 ring packing arrangement [20]. Since this research only uses mSe as a reference standard, for simplicity only the α-phase is used. mSe is known to spontaneously change phase to tSe [25]. A third crystal structure of rhombohedral phase Se_6 rings has been found, but it is quite unstable at ambient conditions [26,27]. The structures of tSe and (α-phase) mSe are shown in Figure 1.2 and the crystallographic details (obtained from Reference [28]) are summarized in Tables 1.1 and 1.2.

One outstanding problem with aSe DCXID technology is that aSe spontaneously crystallizes into tSe [22]. Crystalline materials are not suitable for direct X-ray conversion, and the gradual crystallization of aSe manifests as "dead" pixels in the DCXID image [29]. The process of crystallization is irreversible, and eventually the aSe DXCID must be discarded. To improve the life-span of a DXCID "stabilized" aSe is used. Stabilized aSe is normal aSe alloyed with 0.2% to 0.5% As and doped with Cl to concentrations of a few parts per million [30]. Adding arsenic to aSe greatly

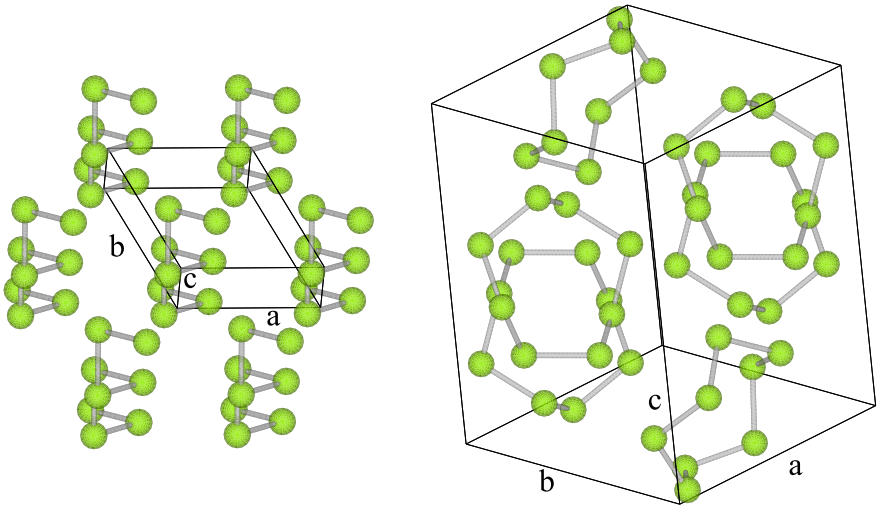

Figure 1.2: The crystal structure of tSe (on the left) and mSe (on the right). The unit cells and crystal axes are also indicated.

Table 1.1: The crystal structure of tSe and mSe. The space group is indicated using the Hermann-Mauguin notation. The tSe structure has one inequivalent site, the mSe structure has eight inequivalent sites.

Crystal	Spacegroup	a [Å]	b [Å]	c [Å]	α [rad]	β [rad]	γ [rad]
tSe	$P3_221$	4.36	4.36	4.95	90	90	120
mSe	$P2_1/n$	9.05	9.07	11.61	90	90.767	90

Table 1.2: The coordinates of the inequivalent atoms in tSe and mSe. tSe has only one inequivalent site, mSe has eight. Coordinates are given in fractions of unit cell lengths.

Atom Site	x	y	z	Atom Site	x	y	z
$tSe_{(1)}$	0.217	0	0.16667	$mSe_{(5)}$	-0.081	0.686	0.521
$mSe_{(1)}$	0.321	0.486	0.237	$mSe_{(6)}$	-0.156	0.733	0.328
$mSe_{(2)}$	0.427	0.664	0.357	$mSe_{(7)}$	-0.084	0.520	0.229
$mSe_{(3)}$	0.317	0.637	0.535	$mSe_{(8)}$	0.131	0.597	0.134
$mSe_{(4)}$	0.134	0.820	0.556				

retards the rate of crystallization, but introduces charge traps which reduce the photoconductivity of aSe [4, 16]. Doping with Cl helps restore the photoconducting ability of the arsenic-doped selenium alloy (aSe:x%As) [31, 32]. Since charge traps are very detrimental to image resolution [16], a detailed understanding of the role of arsenic in retarding the rate of crystallization is necessary to identify strategies to prolong the life-time of aSe DCXIDs without creating charge traps.

In this research I used synchrotron sources of X-rays to characterize the physical and electronic structure of aSe, and the local structure of the arsenic dopants. While the structure of pure a-Se has been studied repeatedly [5, 6, 8, 33–35], the exact structure is still somewhat contested [36]. It is accepted that the structure of aSe involves helical chains and/or Se_8 rings, but the exact breakdown between the two was somewhat controversial [6, 37]. Currently the prevailing theory is that aSe is mainly composed of tangled and distorted helical chains, similar to the trigonal phase [38, 39], and that the structure has very few Se_8 rings [36, 40]. Finally, to my knowledge there has been no study of the structure of aSe:x%As thus far. The ultimate goal of this research was:

1. to determine the local structure near arsenic dopants,
2. to identify the mechanism behind the retardation of crystallization, and
3. to find or establish methods to suppress crystallization.

This thesis is organized as follows: Chapter 2 outlines the basic operating principles of synchrotrons and the creation of synchrotron radiation. A brief synopsis of the capabilities and performance of the beamlines used in this research is also presented. Chapter 3 outlines the theory behind X-ray interactions with matter, and explains each spectroscopic technique used in this research. Chapter 4 is devoted to an in-depth look at the theory and practice of Extended X-ray Absorption Fine Structure spectroscopy, the main spectroscopic technique used herein. Chapter 5 outlines the basic principles behind Density Functional Theory calculations and elaborates on the capabilities of some of the software packages used in this research. Chapter 6 outlines the sample preparation method and provides a basic overview

of the X-ray spectroscopy measurements that were performed. Chapter 7 provides a detailed analysis and summary of all the hard X-ray spectroscopy measurements performed, and relates these measurements to theoretical models of the structure of amorphous selenium. Chapter 8 discusses the electronic structure of amorphous selenium, summarizes the soft X-ray spectroscopy measurements, and relates them to the theoretical density of states of amorphous selenium. Chapter 9 discusses structural models of amorphous selenium and tunes these models to match measured spectra. Finally, Chapter 10 outlines the principles and approaches to reverse Monte Carlo modeling, and discusses the preliminary results obtained from this technique.

Chapter 2

Synchrotron Radiation

Synchrotrons, sources of intense and monochromatic X-rays, are an ideal tool for studying the electronic and physical structure of materials. In a synchrotron electrons moving at relativistic speeds are accelerated around a large polyhedron. At each turn the electrons produce a broad energy range of intense electromagnetic radiation. Additional apparatus in the straight sections, called "insertion devices" can produce even more intense radiation. The radiation is piped tangentially from bending magnets and insertion devices in a "beamline", terminating in the experimental apparatus, or "endstation". The following sections briefly describe the key components of a synchrotron and the beamlines at the Canadian Light Source (CLS) at the University of Saskatchewan and the Advanced Light Source (ALS) at the Lawrence Berkeley National Lab used to take measurements for this research.

2.1 Linear Accelerator

To generate free electrons for use in the synchrotron, a linear accelerator (linac) is often used. These typically start with an electrode gun where a metal cathode is pulsed with high frequency oscillating current. This causes electrons to be ejected from the surface of the cathode. A series of RF cavities are used to further accelerate the electrons. Additional cavities may also provide some rudimentary shaping to the electron beam. At the ALS, for example, the linac has a 124.914 MHz cavity, a 499.654 MHz cavity, and a 3 GHz cavity which are used to shape the pulsed electrons into from their initial 2.5 ns bunch width to bunches 20 ps wide [41]. The end result of the CLS and ALS linacs are 250 MeV and 50 MeV electrons, respectively.

2.2 Booster Ring

The booster ring is a compact ring used to accelerate the electrons to operating energies. In both the ALS and the CLS (and in many other synchrotrons) the booster ring is positioned inside circumference of the larger storage ring. It is from the operation of the booster ring that the synchrotron gets its name. The electrons are "boosted" in speed by radiowave pulses which are synchronized with the electron orbit.

At the CLS the 200 to 250 MeV electrons are boosted to the 2.9 GeV operating energy. There are 28 quadrupole and 20 dipole magnets in an oval ring with a major radii of 18.8 m and a minor radii of 12.7 [42]. The electrons are accelerated to the operating energy in about 0.2 s, during which the dipole fields increase from 0.115 T to 1.333 T [42]. The RF cavity which drives the electrons runs at 500 MHz and 1.5 MV [42].

At the ALS the 50 MeV electrons are boosted to the 1.9 GeV operating energy. There are 20 sextupole, 32 quadrupole, and 24 dipole magnets [43] in a roughly circular ring of 4 curved sections and 4 straight sections, with a circumference of 75 m [44]. The electrons are accelerated to the operating energy using a 499.654 MHz RF cavity [44].

The operation of the linear accelerator and the booster ring also causes the beam of electrons to change from a continuous stream to a sequence of discrete bunches. This is due to the fact that the energy boost supplied by the RF cavities is based on the electron velocity; faster electrons gain more energy, pushing them ahead, and slower electrons gain less, causing them to lag behind.

2.3 Storage Ring

The storage ring is the main part of the synchrotron. Here electrons are maintained at the operating energy by RF cavity klystrons. The CLS storage ring is 170.88 m in circumference, with twelve 5.2 m straight sections and twelve curved sections. Each

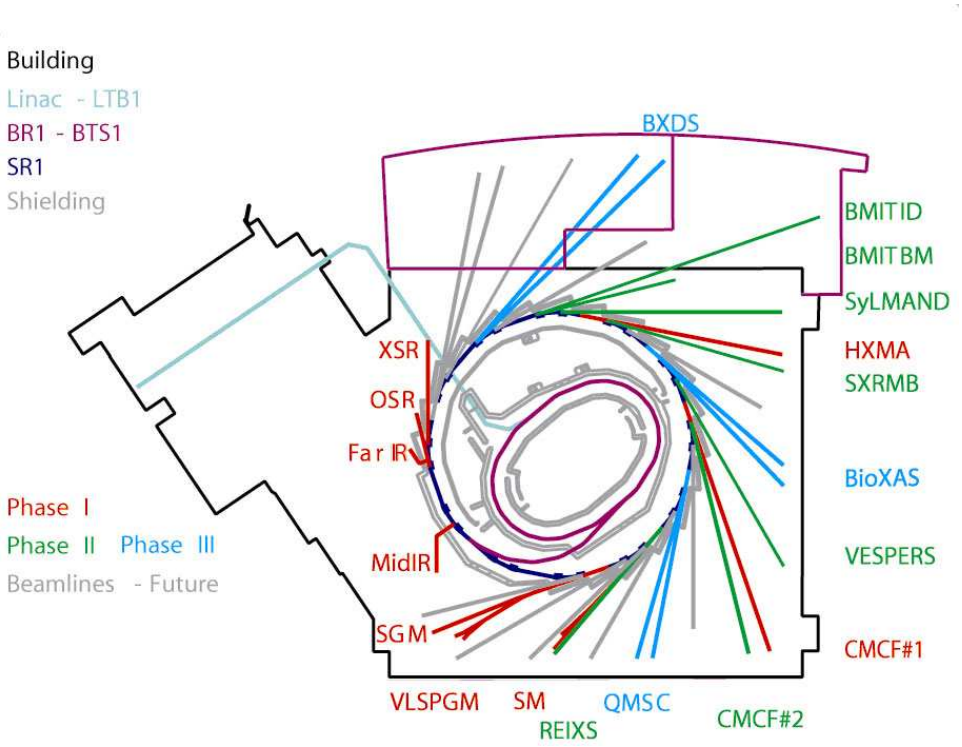

Figure 2.1: The floor plan for the CLS. The linac, booster ring, storage ring, and beamlines are colour coded. (Figure from www.lightsource.ca)

curved section has 2 dipole bend magnets, 6 quadrupole magnets, and 3 sextupole magnets. One straight section contains a superconducting RF cavity and one straight section is used to connect the storage ring to the booster ring [45]. The layout of the CLS storage ring is shown schematically in Figure 2.1.

The ALS storage ring is is 196.8 m in circumference, and composed of twelve 5 m straight sections and twelve curved sections. Nine of the curved sections have 3 dipole bend magnets, 6 quadrupole magnets, and 4 sextupole magnets. The remaining three curved sections have a dipole superbend magnet (a dipole made from superconducting magnets) replacing one of the normal bend magnets, and 2 additional quadrupole magnets. One of the straight sections contains 2 RF cavities and one straight section is used to connect the storage ring to the booster ring. The other 10 sections are available for beamlines [46].

At the operating energy the electrons are accelerated to speeds extremely close

to that of the speed of light. While the acceleration of low-speed electrons causes radiation to be emitted in a toroidal profile, the radiation emitted by relativistic electrons is highly collimated into forward and backward facing cones. The angular spread of these cones of radiation is about $\frac{1}{\gamma}$. At the CLS, with an operating energy of 2.9 GeV, the beam width is only about 2.5 mm at a 20 m distance.

2.4 Bending Magnet

A large dipole magnet is used to bend the electron beam around the corner at each vertex of the polyhedral storage ring or booster ring. When the electrons are bent, they emit full spectrum electromagnetic radiation in a horizontal fan shape. The vertical divergence of this radiation is again about $\frac{1}{\gamma}$.

The radiation from a bending magnet covers a broad range in energy. The most important parameter characterizing this radiation is the critical energy, E_c. This is the threshold where half the radiation power lies below the critical energy, and half lies above. The E_c for a bending magnet is given by Equation 2.1, where ρ is the bend radius, B_0 is the peak magnetic field (in T), and E is the electron energy (in GeV). The condensed form of Equation 2.1 gives E_c in keV. It is usually possible to get sufficient levels of photon intensity for absorption experiments using energies up to $4E_c$.

$$E_c = \frac{3\hbar c\gamma^3}{\rho} = 0.665 B_0 E^2 \tag{2.1}$$

In plane with the ring, bend magnets produce horizontally polarized light. The light that diverges above and below the plane is elliptically polarized, and becomes circularly polarized at $\frac{1}{\gamma}$ above the plane.

2.5 Undulator

To gain even more intensity at a particular energy insertion devices are used. An undulator is an array of alternating permanent magnets built into a straight section

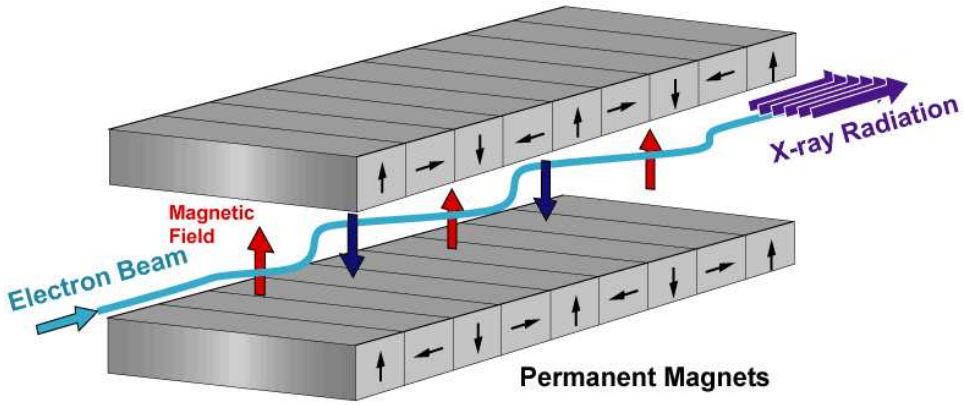

Figure 2.2: A simple representation of an undulator. The X-ray radiation produced from each pair of magnets adds coherently to form an intense X-ray beam. (Figure from www-xfel.spring8.or.jp)

of the storage ring. This array causes the electron beam to oscillate sinusoidally in the plane of the ring, as shown in Figure 2.2. The figure of merit K, given by Equation 2.2 is used to describe an undulator; typically $K \sim 1$. Here B_0 is the undulator magnetic field, λ_p is the length of the periodicity in the undulator magnets, and of course e and m_e are the charge and mass of an electron.

$$K = \frac{eB_0\lambda_p}{2\pi m_e c} \tag{2.2}$$

The magnet spacing and the magnetic field of an undulator are tuned to provide coherent interference for a particular bandwidth of radiation. In practice the magnet spacing is fixed once the undulator is constructed, so only the magnetic field is varied. This is often achieved by simply changing the gap spacing between the top and bottom magnets. The coherent interference in the radiation emitted at each set of dipole magnets means that the spectrum from an undulator is quasi-monochromatic; only a narrow bandwidth and subsequent harmonics are produced.

$$\lambda_n = \frac{\lambda_p}{2n\gamma^2}\left(1 + \frac{K^2}{2} + \gamma^2\theta_{obs}\right) \tag{2.3}$$

The wavelength (and harmonics) produced by an undulator are given by Equation

2.3. Here λ_n is the wavelength of the n^{th} harmonic, λ_p is the periodicity in the undulator magnets, θ_{obs} is the observation angle in the horizontal plane, and K is from Equation 2.2. Because of the summation of coherent light from each period in the undulator, in principle an undulator of N periods can supply N^2 times the photon flux at a given energy as a bending magnet. The basic design of an undulator provides horizontally polarized light. Two additional magnetic arrays can provide elliptical polarization. Undulators are often used for soft X-ray beamlines which require a relatively limited range in energy and demand a large amount of photon flux.

2.6 Wiggler

A wiggler is an insertion device following essentially the same design as an undulator, but in a wiggler a smaller array of more powerful electromagnets or superconducting electromagnets is used. Unlike an undulator, a wiggler is not designed for coherent interference from the radiation from each set of magnetic poles. A wiggler is characterized by the same figure of merit, K, as an undulator (refer again to Equation 2.2), but for a wiggler $K \gg 1$. This causes overlap between the harmonics, especially at high energies, and therefore in the X-ray region a wiggler has essentially the same spectral output as a bending magnet - but a wiggler with N magnetic poles will produce $2N$ times the photon flux as a bending magnet.

Wigglers are often used as sources for hard X-ray beamlines, especially EXAFS beamlines, where a broad range of X-rays is required. The photon flux intensities from several undulators and a superconducting wiggler from CLS are shown in Figure 2.3.

2.7 Monochromators

For use in an experiment, the bandwidth of the X-ray beam from a bend magnet or an insertion device must be further reduced. To achieve this, a grating or crystal

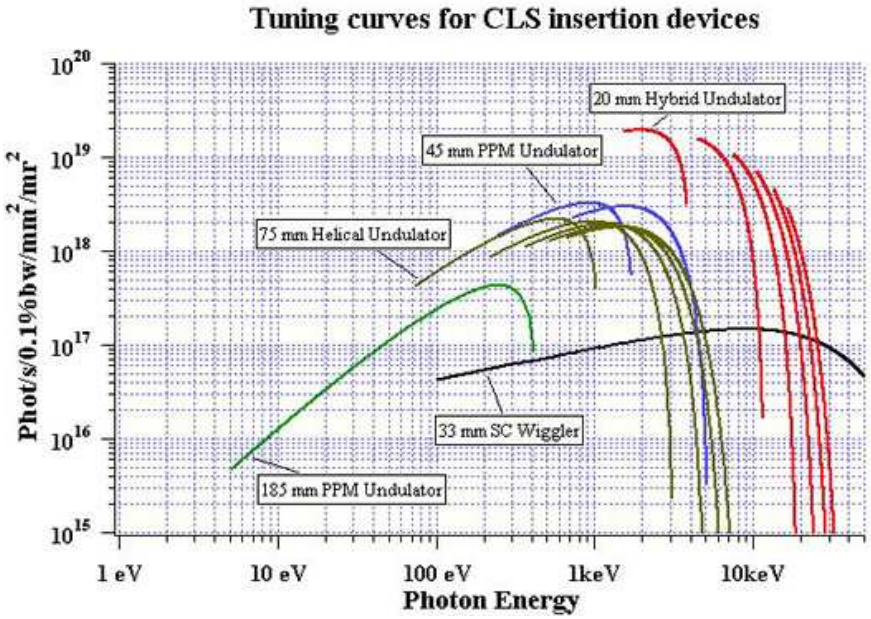

Figure 2.3: The brightness of several CLS insertion devices as a function of energy. Note that while undulators all have higher flux intensities, wigglers operate over a much larger energy range. (Figure from www.lightsource.ca)

monochromator is used. The basic design involves two offset gratings or crystals rotated in a manner that fulfills the Bragg diffraction condition for the desired energy, producing a monochromatic beam.

A grating is often used for soft X-ray beamlines, while cleaved crystal faces are used for hard X-ray beamlines. Monochromators do not reject harmonics of the desired energy, and often additional optics, such as harmonic rejection mirrors, are used. On hard X-ray beamlines harmonic rejection is also sometimes achieved by detuning the monochromator - moving the second crystal slightly out of alignment with the first. While this reduces the intensity of the primary harmonic, it provides a much larger reduction in the higher harmonics.

2.8 Hard X-ray Microprobe Analysis Beamline

The Hard X-ray Microprobe Analysis (HXMA) beamline at the CLS was the primary tool used to investigate the structure of amorphous selenium. As the name suggests, the HXMA beamline uses "hard" X-rays, in the energy range of 5 to 40 keV. The source for the X-rays is a 63 pole, 2 T wiggler with $K \simeq 5.91$ [47]. The appropriate energy is selected using a crystal monochromator. At the time of this research Si(111) and Si(220) crystals were available. The beamline also uses a collimating mirror with an Rh or Pt stripe. At 10 keV, with an Si(111) crystal and Rh mirror, the beamline delivers 1.2×10^{13} photons per second per mm^2 to the sample with a resolving power $E/\Delta E$ of 5×10^3 [47]. The layout of the beamline optics for HXMA is shown in Figure 2.4.

HXMA allows measurements in either transmission or fluorescence mode. The experimental setup for transmission measurements is very simple, using only three ion chambers. An ion chamber is a cavity filled with a mixture of H, N_2, and Ar between two metal plates, which is placed in the X-ray beam. Transparent Be windows allow the beam to pass through the chamber. A large voltage is created between the two plates. The passage of X-rays through the chamber ionizes some of the gas, which creates a current between the metal plates. The magnitude of this

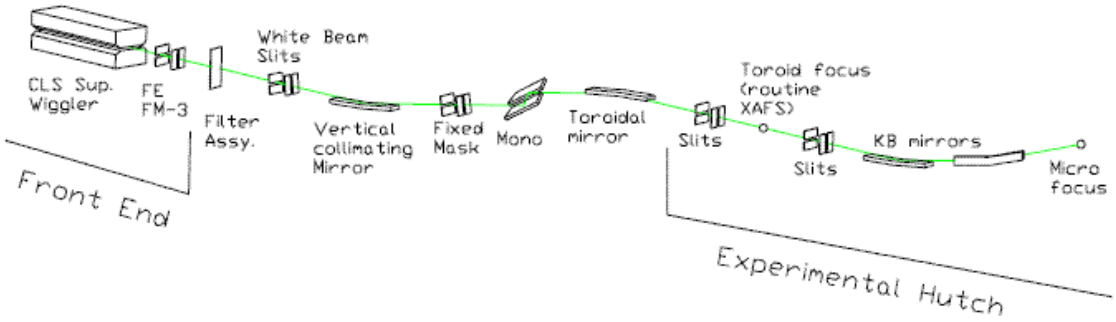

Figure 2.4: The layout of the X-ray optics, slits, and other devices for the HXMA beamline. (Figure from www.lightsource.ca)

current is proportional to the intensity of the beam. In a transmission measurement, one ion chamber measures the beam intensity before the sample and one chamber measures the beam intensity after passing through the sample. Typically a reference foil is positioned after the second ion chamber, and a third ion chamber is placed after that. Because measurements at HXMA often take place over a very long energy range it is important to have a reference standard for calibration measured simultaneously with the experimental data.

The setup for a fluorescence measurement is similar to that of a transmission measurement, save for the addition of a fluorescence detector usually placed near the sample perpendicular to the X-ray beam. HXMA has three types of fluorescent detectors available: a Lytle detector, a Saturn-Vortex detector, and 32-element Ge detector. The Lytle detector is based on an ion chamber, but is usually filled with a denser gas (Ar or even Xe). This detector is not very sensitive, and is best used for concentrated samples. The Saturn-Vortex detector is a single channel semiconductor drift detector. An incident X-ray can create a high energy conduction electron, which in turn can cascade creating several lower energy conduction electrons. This current is read by the detector. Extremely high count rates can saturate these kinds of detectors, and so they are best used for dilute samples. The 32-element Ge detector is like a Saturn-Vortex detector, save that it has 32 channels. Since fluorescent

measurements often have a low signal-to-noise ratio multiple measurement are needed to get good data. The 32-element Ge detector can effectively repeat a spectrum 32 times in one measurement, which greatly helps in reducing the noise. Like the Saturn-Vortex, the 32-element Ge detector is prone to saturating when exposed to concentrated samples. The 32-element Ge detector must also be cooled with liquid nitrogen while in use.

Because hard X-rays have no trouble penetrating the atmosphere, HXMA measurements are often performed at ambient conditions. All the experimental apparatus is housed in a steel hutch, which must be sealed prior to measuring to protect the users from the X-ray radiation. HXMA also has a liquid helium or liquid nitrogen cooling system for low temperature measurements. This is a chamber which sits in the path of the beam, with the sample inside.

2.9 Spherical Grating Monochromator Beamline

The Spherical Grating Monochromator (SGM) beamline at the CLS was used for a completeness study of the X-ray absorption edges of selenium. The SGM uses "soft" X-rays in the energy range of 250 to 2000 eV. The source for the X-rays is a permanent magnet undulator with a 45 mm period [48]. The appropriate energy is selected by a spherical grating monochromator, as suggested by the beamline name. There are three different interchangeable gratings corresponding to low, medium, and high energy ranges with rulings of 600, 1100, and 1700 lines/mm, respectively [48]. On the low energy grating at 400 eV with the entrance and exit slits of the monochromator set to 5 μm and 25 μm, respectively, the beamline delivers 10^{11} photons/s of flux. At energies below 800 eV the SGM has a resolving power $E/\Delta E$ better than 10^4 [49].

The SGM allows for measurements in either fluorescence yield or electron yield mode. The experimental setup is the same for both techniques: the sample is affixed (usually with carbon tape) to a copper backplate and is placed in an ultra-high vacuum (UHV) chamber. Soft X-rays are easily absorbed by atmosphere, so UHV is essential. The vacuum in the SGM endstation is typically better than 10^{-7} torr.

The fluorescence yield is measured with a graphite channeltron, which operates in essentially the same manner as the drift detectors discussed in the previous section. The electron yield is measured by monitoring the current flowing into the sample to replace the electrons ejected by X-ray absorption. The incident X-ray intensity is measured with a highly transparent gold mesh upstream of the endstation. The X-ray induced electric current in the mesh is proportional to the incident X-ray intensity.

2.10 Variable Line Spacing - Plane Grating Monochromator Beamline

The Variable Line Spacing - Plane Grating Monochromator (VLS-PGM) beamline at the CLS was used to help characterize the electronic structure of selenium. The VLS-PGM uses X-rays in the energy range of 5 to 250 eV, even "softer" than the X-rays from the SGM. The source for the X-rays is a permanent magnet undulator with a 185 mm period [50]. The appropriate energy is selected by a planar grating monochromator with variable line spacing as suggested by the beamline name. There are three different interchangeable gratings corresponding to low, medium, and high energy ranges with central line densities of 500, 1000, and 600 lines/mm, respectively [51]. The VLS-PGM delivers on the order of 9×10^{11} photon/s of flux per 100 mA of ring current on all three gratings with 50 μm slits, and the resolving power $E/\Delta E$ is better than 10^4 [50].

Like the SGM, the VLS-PGM allows for measurements in either fluorescence yield or electron yield mode. The samples are prepared in a manner similar to that used for the SGM, and the measurements are conducted in UHV. Since the VLS-PGM operates at quite low X-ray energies UHV is essential, and there is often quite a bit of background noise to the measurements. The incident X-ray intensity at the VLS-PGM is measured by a highly transparent nickel mesh.

2.11 Beamline 8.0.1

The soft X-ray fluorescence (SXF) endstation of beamline 8.0.1 (BL8) at the ALS was also used in this research. BL8 has an energy range of 70 to 1200 eV. The source for the X-rays is a permanent magnet undulator with a 50 mm period [52]. The appropriate energy is selected by a spherical grating monochromator. There are three different interchangeable gratings corresponding to low, medium, and high energy ranges with rulings of 150, 380, and 925 lines/mm, respectively [52]. At maximum flux, BL8 delivers on the order of 10^{15} photons per second per mm^2 with a resolving power $E/\Delta E$ of roughly 10^4 [52].

Like the previous two beamlines, BL8 allows for measurements in either fluorescence yield or electron yield mode. Unlike the other beamlines BL8 has a spherical grating spectrometer to perform high resolution analysis of the X-ray fluorescence. The spectrometer is a grazing incidence detector with Rowland circle geometry [52]. There are 4 spherical gratings corresponding to different energy ranges; the low and mid-low energy gratings have a 5 m radius and have 600 and 1500 lines/mm, respectively. The mid-high and high energy gratings have a 10 m radius and have 600 and 1500 lines/mm, respectively [52]. Again, the measurements are performed in UHV. Like the SGM, the incident X-ray intensity is measured with a highly transparent gold mesh.

Chapter 3

Experimental Techniques

The interactions between X-rays and matter are the primary mechanism used to study the material properties of a-Se:x%As in this research. X-rays have a wavelength comparable to the size of an atom, and have energies in the range of most binding energies for core electrons. Because of these properties X-rays are an ideal tool for *in situ* probing of material properties in a non-destructive and element specific manner. There are three main measurement techniques that are used: X-ray Absorption Near Edge Structure (XANES), Extended X-ray Absorption Fine Structure (EXAFS), and X-ray Emission Spectroscopy (XES). The following sections describe how X-rays interact with matter, and how each of the three aforementioned techniques provides structural and/or electronic information about the material.

3.1 X-ray Interactions with Matter

When an X-ray penetrates matter there are three possible outcomes: the X-ray may be transmitted, without any change to its energy or momentum, and without any effect to the substance, the X-ray may undergo a change in momentum (elastic scattering) and possibly a reduction in energy (inelastic scattering), or the X-ray may be absorbed by the substance. Obviously the first situation is of little interest for X-ray spectroscopy. Of the latter two, X-ray absorption is the technique most relevant for the research carried out in this thesis.

The phenomenon of X-ray absorption follows Fermi's Golden Rule, where the interaction Hamiltonian is the appropriate operator for an electromagnetic wave. The X-ray absorption, μ, is given by Equation 3.1 where $\vec{e}$ is the electromagnetic field

of the incident X-ray, $\vec{p}$ is the electron momentum vector, $\vec{k}$ is the X-ray wavevector, $\vec{r}$ is the position vector in the appropriate coordinate system for the material (usually taken as $\vec{z}$), and the subscripts i, f denote the initial and final states, respectively. The summation is carried out over all possible initial and final states.

$$\mu \propto \sum_{i,f} \left| \langle \psi_i | \left(\vec{e} \cdot \vec{p} \right) \exp \left(i\vec{k} \cdot \vec{r} \right) | \psi_f \rangle \right|^2 \tag{3.1}$$

When working with Equation 3.1, the usual convention of expanding the exponential into a power series is usually followed. Although X-rays have very small wavelengths, the spatial distribution of a core electron is often much smaller: sufficiently small to make a first order approximation of the exponential adequate to describe most experimental spectra. In this case, Equation 3.1 reduces to the dipole approximation:

$$\mu \propto \sum_{i,f} \left| \langle \psi_i | \left(\vec{e} \cdot \vec{p} \right) | \psi_f \rangle \right|^2 \tag{3.2}$$

This approximation suggests that all X-ray induced electron transitions $|\psi_i\rangle \rightarrow |\psi_f\rangle$ are induced by the oscillating electric field of the X-ray. Due to the small effective radius of the core electrons, the electric field of the X-ray is effectively constant across the entire orbital. Angular momentum is a "good" quantum number for both the core and bound final states and therefore the total angular momentum must be preserved. Since a photon has a spin of ± 1, dipole transitions are therefore limited to a final state angular momentum of $\ell \pm 1$ where ℓ is the angular momentum of the initial state.

In terms of bound state quantum numbers, the change in primary quantum number Δn is not constrained in a radiative process. The change in angular momentum $\Delta \ell$ is ± 1, as previously mentioned. The change in total angular momentum, $\Delta j = 0, \pm 1$ where $j = \ell \pm s$ for spin $s = \frac{1}{2}$. However a transition between two states both with $j = 0$ is not allowed [53]. For historical reasons the labels denoting X-ray transitions to or from a core state are often in a different set of symbols than are typically used to describe atomic orbitals. These are summarized in Table 3.1.

Table 3.1: Summary of notation used for identifying specific atomic orbitals, X-ray transitions to or from those orbitals, and the corresponding quantum numbers.

n	ℓ	j	Atomic Orbital	X-ray Transition
1	0	$\frac{1}{2}$	$1s$	K
2	0	$\frac{1}{2}$	$2s$	L_1
2	1	$\frac{1}{2}$	$2p_{1/2}$	L_2
2	1	$\frac{3}{2}$	$2p_{3/2}$	L_3
3	0	$\frac{1}{2}$	$3s$	M_1
3	1	$\frac{1}{2}$	$3p_{1/2}$	M_2
3	1	$\frac{3}{2}$	$3p_{3/2}$	M_3
3	2	$\frac{3}{2}$	$3d_{3/2}$	M_4
3	2	$\frac{5}{2}$	$3p_{5/2}$	M_5
4	1	$\frac{1}{2}$	$4s$	N_1
			...	

By convention the symbol for the lowest energy level in an X-ray transition is used to denote the process. Usually a Greek letter is subscripted to the symbol to denote a specific transition, these letters proceed alphabetically from the most intense to the least intense transition. For example a $2p \rightarrow 1s$ transition is denoted by the symbol K_α, a $3p \rightarrow 1s$ transition is denoted by the symbol K_β, and so on [53]. Sometimes the effect of the second order term in the power series expansion of Equation 3.1 is visible as low energy and low intensity features in an X-ray absorption measurement. These features are due to quadrupole transitions, and incorporating them requires adding an additional term to Equation 3.2:

$$\mu \propto \sum_{i,f} \left| \langle \psi_i | \left(\vec{e} \cdot \vec{p} \right) \left(1 + \vec{k} \cdot \vec{r} \right) | \psi_f \rangle \right|^2 \tag{3.3}$$

A quadrupole transition allows the final state to have angular momentum $\ell \pm 2$. Quadrupole transitions occur mostly in transition metals when the $1s$ electrons are excited. Since many transition metals have a large number of partially occupied d states near the Fermi level, quadrupole features are sometimes visible. Neither selenium nor arsenic have any unoccupied $3d$ states, and the $4d$ states are too high in energy. Any excitation to a $4d$ state is masked by the much more intense transitions to unoccupied $4p$ states. Because of this no quadrupole features are present in neither the spectra of selenium nor arsenic.

3.2 X-ray Absorption Near Edge Spectroscopy

X-ray Absorption Near Edge Spectroscopy (XANES) is conducted by monitoring the absorption of X-rays at energies close to the binding energy of a particular core electron. The incident energy is gradually increased and the effect on the sample is monitored. When the core electron absorbs an incident photon that electron can get excited to a vacant state in the conduction band (according to the aforementioned dipole selection rules). At any given incident X-ray energy, E, the amount of photons absorbed - and consequently the amount of excited core electrons - is proportional to the partial unoccupied density of states at an energy E relative to the core electron.

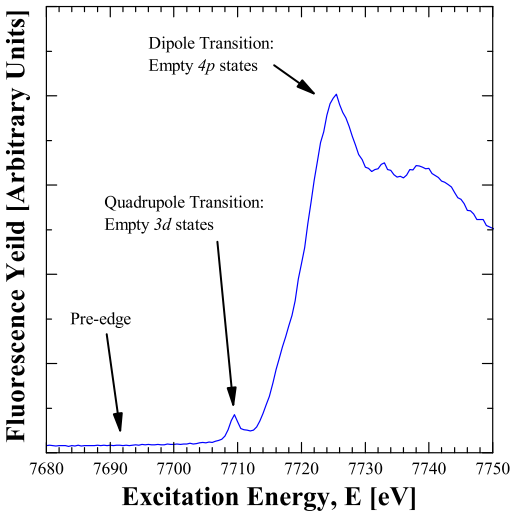

Figure 3.1: A small, pre-edge quadrupole transition in the Co K XANES of Co-doped sapphire. Note the intensity of the quadrupole transition relative to the much more prominent dipole transitions.

The absorption of X-rays with energies near the binding energy of a particular core electron is therefore a probe of the partial (or projected) unoccupied density of states (DOS).

The final state of an electronic transition determines the shape of the spectrum (the "final state rule"). Because of this a XANES measurement is rarely a probe of the normal conduction band. In an absorption measurement the final state is one with an electron in a normally unoccupied level, and a hole in a core level. This core-hole can severely distort the normal unoccupied density of states, and accordingly a XANES measurement might not be a useful probe of the ground-state electronic structure. The core-hole decreases the screening of the nuclear charge, and in some cases can be modeled by increasing the atomic number by one. In general, however, detailed calculations are needed to accurately account for the effects of the core-hole.

The actual practice of measuring the absorption of the X-ray beam may be accomplished by several different techniques. The best technique is a transmission measurement, where the intensity of the incident X-ray beam is measured before entering and after passing through the sample. The X-ray beam attenuates expo-

nentially inside the sample, and the X-ray absorption coefficient μ is simply the logarithm of the two intensities, as shown in Equation 3.4, where t is the sample thickness, I_0 is the incident X-ray intensity, and I_t is the transmitted X-ray intensity. A transmission measurement avoids many of the problems associated with other absorption techniques, and a good measurement gives an actual measure of the X-ray absorption with the proper intensity. However creating a homogeneous sample with the proper thickness is often a challenge.

$$\mu(E) = \frac{1}{t} \ln\left(\frac{I_0(E)}{I_t(E)}\right) \tag{3.4}$$

Both X-ray fluorescence yield and X-ray electron yield are easier measurements to perform than X-ray transmission measurements. The core-hole created by absorbing an incident X-ray is extremely short-lived, and very quickly another electron decays to fill the core state. This process releases energy, which can be in the form of an X-ray or exciting another electron or electrons to an unbound state. The former technique is fluorescence yield, detected with a high voltage channelplate, a germanium detector, or possibly a grating spectrometer (refer back to Chapter 2 for more detail). The latter technique is electron yield, detected simply by measuring the current that flows into the sample to replace the charge that was ejected from the surface. This ease of measurement comes with draw-backs. For both techniques the X-ray absorption coefficient μ can, at best, only be determined within a constant of proportionality by dividing the intensity of the fluorescence yield I_f or electron yield I_e with the incident intensity I_0, as shown in Equation 3.5. Without additional information comparing absolute intensities between different samples or even different measurements is impossible.

$$\mu(E) \approx \frac{I_x}{I_0};\ x = f, e \tag{3.5}$$

Finally, fluorescence yield measurements can suffer from self-absorption; the material attenuates the fluorescent signal. As pointed out in the previous discussion on transmission measurements the attenuation is dependent on μ, and in the case of fluorescence, the source X-rays (i.e. the X-rays from fluorescence) are proportional

to μ. The basic effect of self-absorption is given in Equation 3.6, where μ_i is the absorption coefficient of the absorbing element, μ_{tot} is the total absorption coefficient of the sample, E is the energy of the incident X-ray beam, E_f is the energy of the fluorescence transition, and t is the thickness of the sample. Since neither μ_i nor μ_{tot} is known self-absorption is impossible to correct without rather large approximations. The end result of self-absorption is a spectrum where the normally sharp and prominent features are smoothed out and reduced in intensity. The only definite way to check for self-absorption is to continually reduce the thickness and/or dilute the sample until the spectra become consistent, or to compare the fluorescent yield spectra with transmission or electron yield spectra.

$$\frac{I_f}{I_0} \propto \frac{\mu_i(E)}{\mu_{tot}(E) + \mu_{tot}(E_f)} \left(1 - \exp\left(-t\left(\mu_{tot}(E) + \mu_{tot}(E_f)\right)\right)\right) \tag{3.6}$$

Electron yield measurements are free from self-absorption effects but are very sensitive to the surface of the sample. Only electrons from a few angstroms deep can escape from the sample. Sometimes this is desired: in the case of thin films, for example, a surface sensitive probe can be advantageous. Insulating samples are additionally sensitive to charging: the electrons cannot be replaced as fast as they are ejected and the sample starts to build up a large positive charge. This makes it increasingly difficult to eject electrons. Charging causes the quality of the spectra to steadily degrade as the measurement progresses.

For hard X-ray measurements a crystal monochromator is typically used. Unlike grating monochromators, crystal monochromators produce "glitches" at energies specific to the crystal cut. A glitch occurs when the wavelength of the incident X-ray matches multiple crystal planes, allowing diffraction in multiple directions. A glitch manifests in the incident X-ray intensity I_0 as a sudden, sharp discontinuity. While normalizing the spectra by I_0 in the appropriate manner will remove most of the effects of the discontinuity, the real problem with a monochromator glitch is that it affects higher order components in a non-linear manner. Since the I_0 intensity measures the entire incident X-ray beam (i.e. all harmonic energies selected by the monochromator), but the absorption μ is only affected by a particular order of energy

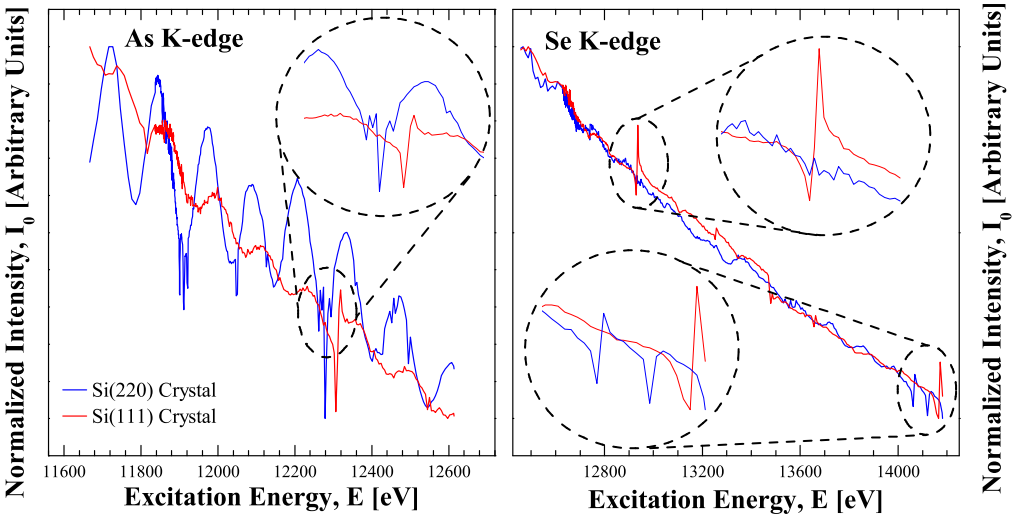

Figure 3.2: Glitches near the As and Se K edges from a Si(111) and Si(220) crystal

(usually first order), the non-linear effects of the glitch can manifest as discontinuities even in the normalized μ. Monochromator glitches always show up in regions specific to the crystal cut, and are easily recognizable. If possible, a monochromator crystal with minimal or no crystal glitches in the energy range of interest should be chosen. If glitches are unavoidable, the data points corresponding to a glitch should be excluded from the spectra. Both crystals available at the HXMA beamline have some glitches near the As and Se K XANES region, but neither have glitches right at the actual absorption edge, as shown in Figure 3.2.

3.3 Extended X-ray Absorption Fine Structure Spectroscopy

For energies above (or higher than) the XANES region the photo-excited electrons are essentially free electrons moving in a wave-like manner through the crystal lattice. The energy of these electrons is given by the difference between the energy of the incident X-rays and the binding energy of the core electron. An Extended X-ray

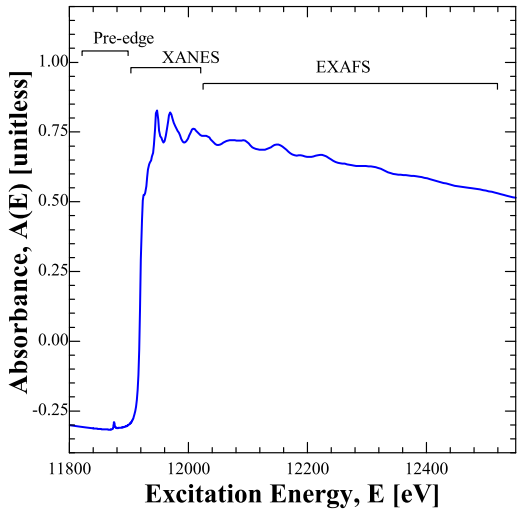

Figure 3.3: An L_3 EXAFS spectrum from a gold reference foil. The pre-edge, XANES, and EXAFS regions are labelled.

Absorption Fine Structure (EXAFS) measurement is made by continuing to increase the incident X-ray energies above the XANES region, as shown by Figure 3.3. The free electrons created by photon absorption can scatter off of neighbouring atoms, and the amount of scatter is based on the electron momentum and the distance to the neighbouring atom. This scatter introduces fluctuations in the EXAFS spectra, which can be used to deduce local structure information.

Returning to Fermi's Golden Rule (refer back to Equation 3.1), for EXAFS we can approximate the final state as: $|\psi_f\rangle = |0\rangle + |\psi_s\rangle$, where $|0\rangle$ is the free electron state, and $|\psi_s\rangle$ is the scattered state. To a first order approximation we have the result given by Equation 3.7, where μ_0 is the background absorption from an isolated atom and the "EXAFS oscillation", χ, is the effect of scattering.

$$\begin{aligned}\mu &\propto |\langle\psi_i| (\vec{e}\cdot\vec{p}) |\psi_f\rangle|^2 \\ &\propto \langle\psi_i| (\vec{e}\cdot\vec{p}) |0\rangle + \langle\psi_i| (\vec{e}\cdot\vec{p}) |0\rangle\langle\psi_i| (\vec{e}\cdot\vec{p}) |\psi_s\rangle \\ &\propto \mu_0 + \mu_0\chi \end{aligned} \tag{3.7}$$

EXAFS measurements are very sensitive, and a high signal-to-noise ratio is im-

portant. Therefore the best measurements are usually transmission measurements (assuming a suitable sample can be prepared). Fluorescence yield is also possible, but electron yield is usually not suitable for EXAFS. A fluorescence yield measurement typically makes use of a filter to screen out background radiation. The filter is typically a screen a few microns thick, made of material one atomic number below that of the material being measured. The filter must be chosen such that the elastically scattered beam is strongly absorbed but the sample fluorescence is mostly transmitted. With fluorescence measurements self-absorption can also effect the EXAFS oscillations, reducing the intensity in the same manner as with XANES.

To obtain good statistics with a transmission measurement, the sample thickness should be chosen such that the maximum absorbance $A = \mu t$ is roughly 2 [54]. This edge jump is usually estimated from calculated background absorption cross-section tables such as those by Henke [55]. The X-ray cross-section, σ, times the density of the material ρ is the absorption coefficient $\mu = \sigma\rho$. For heterogeneous materials the X-ray cross-section for each phase should be weighted by the mass fraction of that phase, the sum of each weighted cross-section is then used as the total cross-section for the material. The ideal sample thickness is then $t = \frac{2}{\sigma\rho}$ for the cross-section just above the absorption edge. For *3d* metals and heavier elements the transmission thickness for the K absorption edge is often thick enough to cause self-absorption effects if measured in fluorescence mode.

For transmission measurements small pin-holes or cracks in the sample cause problems for EXAFS measurements. In principle this issue is also a problem with XANES measurements as well. If the sample is not homogeneous across the incident beam, then the spatial variation in sample thickness cannot be decoupled from the absorption coefficient μ. Pin-holes increase the transmission of X-rays and cause a corresponding decrease in the absorption intensity of intense features in the EXAFS (or XANES) spectra. A pin-hole therefore causes the observed transmission intensity I_t to be a sum of the "real" transmission intensity I_r scaled by some factor β and the incident intensity scaled by $(1 - \beta)$. The observed absorption μ_{obs} is therefore related to the true absorption μ as shown in Equation 3.8, where t is the assumed

sample thickness, and α is the effect of the pin-hole. Actually determining α from a single measurement in order to estimate the true absorption is not possible, and attempting to "fit" α to get a good spectrum is a dubious practice. A sample full of pin-holes is essentially unsuitable for a transmission measurement.

$$\begin{aligned} I_t &= \beta I_r + (1-\beta)\, I_0 \\ \frac{I_0}{I_t} &= \frac{I_0}{\beta I_r + (1-\beta)\, I_0} \\ \mu_{obs} t &= \ln\left(\frac{1}{\beta \exp\left(-\mu t\right) + (1-\beta)}\right) \\ \alpha &= \frac{1-\beta}{\beta} \\ \mu_{obs} &= \frac{1}{t}\ln\left(\frac{1+\alpha}{\exp(-\mu t) + \alpha}\right) \end{aligned} \tag{3.8}$$

The energy scales of X-ray spectra are calibrated through comparison with known standards measured at the same time on the same beamline with the same settings. Usually the measured energy scale of these standards is simply linearly shifted to agree with tabulated values. However since EXAFS measurements cover such a large energy range, a more precise method of calibrating is necessary. Instead of determining a linear energy shift by comparing the location of a feature of a measured reference standard with a tabulated value, the angular correction is calculated. The monochromator angle for the measured and tabulated energies are calculated using Bragg's law, given by Equation 3.9. Here E is the X-ray energy in eV, d is the spacing of the crystal planes or lines on the grating in angstroms, and θ is the angle of the monochromator.

$$E = \frac{(12398.4\ \text{eV Å})}{2d \sin\theta} \tag{3.9}$$

The difference in angle between the energies of the tabulated and measured feature is calculated, and this correction is added to the angles of all the measured data points. The angles are then converted back to energies using Equation 3.9. This technique of energy calibration is in fact more correct than simply linearly shifting

the energies even for XANES measurements, however since XANES measurements cover a much smaller energy range than EXAFS measurements the difference between a linear correction and an angular correction to the energy scale is smaller than the uncertainty in the monochromator energy, and therefore not worth the additional effort.

3.4 X-ray Emission Spectroscopy

If a grating spectrometer is used to measure the fluorescent yield, the high resolution of the equipment can give useful information about the occupied partial DOS. An X-ray emission spectroscopy (XES) measurement uses a grating spectrometer to observe the decay of valence electrons to the core level. In principle an absorption measurement produces an emission spectrum for each absorption energy, but in practice the low fluorescent yield of most materials coupled with the optical inefficiencies of the grating spectrometer mean that collecting a complete emission spectrum for each point in the absorption spectrum is not practical. A typical (non-resonant) emission spectrum involves exciting a core electron to just outside the XANES region, and observing the decay from the valence region. Here the energy dispersive detector collects the energies of the fluorescent X-rays produced by the decay transitions; the incident energy is fixed and a wide range of fluorescence energies are examined.

In an emission measurement the end result is a filled core state and a hole in the valence band. Because of the aforementioned "final state rule", there is no core-hole effect to distort the valence DOS, and thus an XES measurement is an accurate probe for the occupied states. The hole in the valence band has a negligible effect on the material. The process of XANES and XES are visualized by Figure 3.4.

XES measurements suffer from much greater lifetime broadening than absorption measurements. In an absorption measurement the excited electron can last for a relatively long time in the conduction band, improving the resolution of the energy of the transition (recall that energy and time scale are bound by an uncertainty

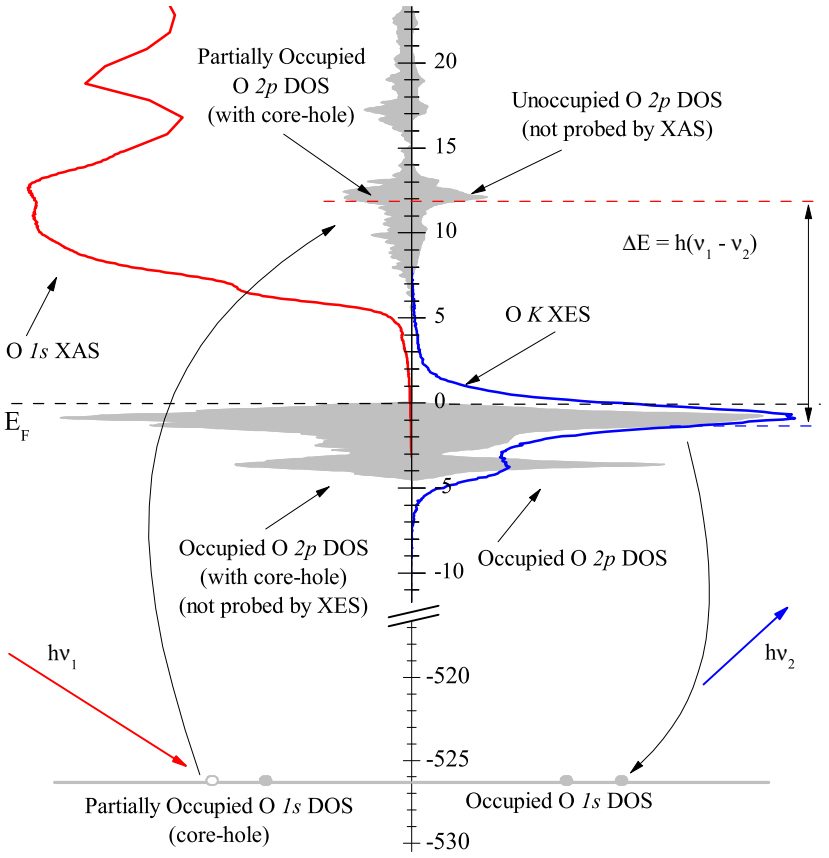

Figure 3.4: A simple representation of O *K* XANES and XES transitions for MgO. Note the slight change in the DOS due to the O *1s* core hole. In heavier elements this change is far more pronounced.

relationship similar to that of momentum and position). In an emission measurement the core-hole state is filled extremely quickly, making the natural line width due to life-time broadening of the transition much larger than the line widths in a XAS spectrum. Therefore XES spectra suffer from very broad features, regardless of the resolution of the equipment.

Chapter 4

Extended X-ray Absorption Fine Structure

Since EXAFS is an integral part of this research, a more in depth look a the theory behind it is in order. While the structural sensitivity of EXAFS, originally known as "Kronig structure" has been recognized since the 1930s, it was only in the early 1970s that Dale Sayers, Farrel Lytle, and Ed Stern recognized how to relate the spectrum to structural information [56]. A detailed look at the theory, experimental practice, and physical meaning of EXAFS, as understood by Sayers, Lytle and Stern is given in References [57–59]. The key to interpreting EXAFS lies in modelling the electron scattering from neighbouring atoms and in doing so, reproducing the experimental spectrum. This process is relatively straight forward and can be done with minimal computer resources.

4.1 Electron Scattering Theory

When an incident X-ray of energy $h\nu$ is absorbed by a core electron with a binding energy E_0 (where $E_0 < h\nu$, of course), the electron is excited to a free state with a kinetic energy of $E_f = h\nu - E_0$ [58]. These free electrons radiate outwards in a wave-like manner and scatter off of neighbouring atoms. If this coherent interference is constructive the EXAFS oscillations χ increase in amplitude and, conversely, if the interference is destructive then χ decreases in amplitude. The nature of the interference is dependent both on the wavenumber k of the free electron and the distance between the core and scattering atoms. Although these oscillations are

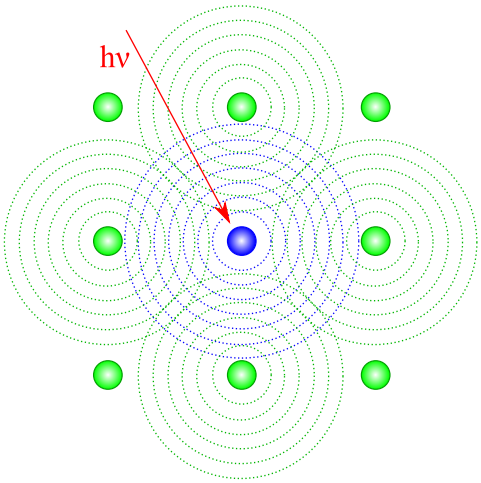

Figure 4.1: A simple representation of an X-ray excited free electron scattering off of neighbouring atoms.

extremely minute, with high intensity synchrotron X-ray radiation they are readily detectible.

As discussed in Chapter 3, the EXAFS oscillations $\chi(k)$ can be decoupled from the absorption coefficient $\mu(E)$ to first order by involving the atomic absorption coefficient $\mu_0(E)$. In slightly more detail, the probability of X-ray absorption by a *1s* photon in the dipole approximation is given in Equation 4.1, where $|i_s\rangle$ is the initial *1s* state, $|f_p\rangle$ is the final p-like state, ω is the angular frequency of the X-ray, and $\rho(E_f)$ is the final density of states at the final electron energy E_f [57, 60].

$$W = \frac{2\pi^2 e^2}{\omega c^2 m^2} \left|\langle f_p | \vec{e} \cdot \vec{p} | i_s \rangle\right|^2 \rho(E_f) \tag{4.1}$$

In EXAFS analysis it is assumed that at energies sufficiently far above the near-edge region, the density of states $\rho(E)$ becomes that of a free electron of energy $\frac{\hbar^2 k^2}{2m} = E_f - E_0$, since band effects are negligible [57]. Therefore the energy dependent features in $\chi(k)$ are due to the matrix elements of the dipole transition. The Hamiltonians of the initial and final state are written in terms of the external potential from the surrounding atoms and the internal potential from the ground state

and excited core atom. In the simple EXAFS formulation, both the internal and external potentials in the final state are treated as static; this is appropriate for cases where the lifetime of the excited state is either long or short compared to the time constant for the rearrangement of screening charge due to the core hole [57]. Indeed, the EXAFS oscillations require coherence between outgoing and backscattered waves and therefore it is likely that the external potential is fully relaxed, since transient effects tend to greatly reduce coherence lengths [61].

In an isolated atom, an excited electron originating from the *1s* ground state must have a wavefunction with p symmetry. In a solid this wavefunction will have additional symmetries mixed in, however only the p symmetric part will show the interference effects characteristic for the EXAFS oscillations $\chi(k)$ [57]. Therefore if we assume that the potential from the excited core atom is short ranged and spherically symmetric (basically the "muffin-tin" approximation) the outgoing part of the excited electron wavefunction is of the form $\psi_k^z(r) = \frac{z}{r}U_k(r)$ [57], where $U_k(r)$ is the regular radial solution of the Schrödinger equation for the excited atom [62]. The additional components along the x- and y-axes are found simply by replacing z, if appropriate (i.e. the X-ray is not polarized or the material is amorphous or polycrystalline). The p portion of the scattered wavefunction is given by Equation 4.2 where $T_k(\vec{r}, \vec{r\prime})$ is the scattering matrix [62].

$$\begin{aligned} \psi_{sc} &= \frac{3mkz}{8\pi^2\hbar^2 r} i U_k(r) I_z(k) \\ I_z(k) &= \int U_k(r') \frac{z'}{r'} T_k\left(\vec{r}', \vec{r}''\right) U_k(r'') \frac{z''}{r''} d^3r' d^3r'' \end{aligned} \tag{4.2}$$

The dipole transition matrix is therefore given by Equation 4.3, where M_0 is the matrix element with no scattering (i.e. $T_k = 0$) which varies monotonically above the absorption edge [57]. The total absorption is then given by Equation 4.4, where W_0 is the absorption of an isolated atom (i.e. $T_k = 0$, again), and the contributions from p states with x and y components have been added.

$$M_{fs} = \langle f_p | \vec{e} \cdot \vec{p} | i_s \rangle$$

$$M_{fs}^k = M_0 \left(1 + \frac{3mkz}{8\pi^2\hbar^2 r} i I_z(k) \right) \tag{4.3}$$

$$W_k = W_0 \left(1 - \frac{3mk}{4\pi^2\hbar^2} \Im \left\{ \sum_{\hat{r}} |\vec{e} \cdot \hat{r}|^2 I_r \left(\vec{k} \right) \right\} + \frac{9m^2k^2}{32\pi^4\hbar^4} \sum_{\hat{r}} |\vec{e} \cdot \hat{r}|^2 |I_r(k)|^2 \right) \tag{4.4}$$

From Equation 4.4 it is obvious that the first term is not dependent on electron momentum k, and therefore is not part of $\chi(k)$. Likewise the last term has smooth variation in k (due to the $|I_r(k)|^2$ component) and will not contribute to the EXAFS oscillations [57]. From inspection, then, $\chi(k)$ is defined by the middle term.

$$\chi(k) = \frac{3mk}{4\pi^2\hbar^2} \Im \left\{ \sum_{\hat{r}} |\vec{e} \cdot \hat{r}|^2 I_r \left(\vec{k} \right) \right\} \tag{4.5}$$

In actual practice Equation 4.5 is rarely used in the given form. In the high-energy limit (where the energy of the electron is above about 50 eV) the crystal is fairly transparent and the main effect of scattering will be to reduce the amplitude of the outgoing wave in an incoherent manner [61]. Using this approximation, and expanding $U_k(r)$ in terms of spherical harmonics Equation 4.5 is reduced to the form given by Equation 4.6, where P_ℓ is a Legendre polynomial, A_i is the attenuation factor from the above high energy scattering approximation, N_i is the number of atoms at distance R_i from the core, ϕ is the phase shift between the incoming and outgoing waves, and δ_ℓ is the atomic phase shift [61].

$$f(\theta) = \frac{1}{2ik} \sum_{\ell=0}^{\infty} (2\ell + 1) \left(\exp(2i\delta_\ell) - 1 \right) P_\ell(\cos\theta)$$

$$\chi(k) = f(\pi) \sum_j A_j(k) \frac{N_j}{R_j^2} \exp(2i\phi) \exp(2ikR_j) \tag{4.6}$$

The expression for $\chi(k)$ most often used is rather phenomenological in nature. Since it was recognized that the EXAFS oscillations are essentially a summation of $\sin(2kR)$ terms caused by backscatter from neighbouring atoms [56], $\chi(k)$ was first expressed in the form given by Equation 4.7 [63].

$$\chi(k) = S_0^2 \sum_j \frac{N_j f_j(k)}{kR_j^2} \exp\left(-2k^2\sigma_j^2\right) \exp\left(-\frac{2R_j}{\lambda}\right) \sin\left(2kR_j + \phi_j(k) + \delta(k)\right) \quad (4.7)$$

In Equation 4.7 S_0^2 is the total amplitude reduction factor, $f_j(k)$ is the EXAFS amplitude function, $\exp\left(-2k^2\sigma_j^2\right)$ is the Debye-Waller factor where σ_j is the root-mean-square thermal displacement of atom j, and $\exp\left(-\frac{2R_j}{\lambda}\right)$ is a damping function where λ is the mean free path of the electron.

Equation 4.5 shows the exact expression for EXAFS oscillations within the one-electron, single scattering, plane-wave, muffin-tin potential model. Shortly after Sayers, Lytle, and Stern published their theory of EXAFS it was pointed out that the mechanism of electron scattering was equivalent to the process of low-energy electron diffraction (LEED), save that electron scattering occurs with full spatial freedom while in experimental practice LEED is a surface effect [61]. In short, the core atom behaves like the electron gun in a LEED experiment, and the surrounding neighbour atoms provide a 3D diffraction lattice [64]. Indeed Lee and Pendry [64] were able to essentially reproduce Equation 4.5 by modifying LEED theory.

Since it is known multiple scattering is required to accurately reproduce LEED measurements [65, 66], it is important to include multiple scattering in crystalline materials. To accomplish this Ashley and Doniach [61] developed a modification to the Green's function formulation of Equation 4.5, while Lee and Pendry [64] simply used Equation 4.5 repeatedly for each "leg" in the scattering path. Multiple scattering in EXAFS is less important than in LEED, however [67], and in amorphous materials or crystals with low symmetry the single scattering model often suffices [61].

Early EXAFS theory focussed on comparing the Fourier transform of Equation 4.7 with known reference standards. Since the sinusoidal components of $\chi(k)$ include a phase shift, a direct Fourier transform will not reproduce the desired positions of the backscatterer atoms. The correct technique is a "phase-shifted" Fourier transform given by Equation 4.8 [56].

$$\chi(r) = -\sqrt{\frac{2}{\pi}} \int \frac{\chi(k)}{kS_0^2 f_\alpha(k)} \sin\left(2kr + \phi_\alpha(k) + \delta(k)\right)$$
$$= \frac{1}{2} \sum_j \frac{N_j}{R_j^2 \sigma_j} \exp\left(-\frac{2R_j}{\lambda}\right) \exp\left(-\frac{2\left(r - R_j\right)^2}{\sigma_j^2}\right) + \Delta(r) \qquad (4.8)$$

When applied in the correct circumstances, the error term $\Delta(r)$ is negligible. It is important to point out that Equation 4.8 will only produce the correct radial distances for systems where the backscatterer atoms are all of the same species, i.e. $f_j(k) = f(k)$ and $\phi_j(k) = \phi(k)$. Otherwise this method will produce the correct radial distances only for atom species α. It is also important to point out that this method of analysis can not incorporate the multiple scattering effects.

4.2 Calculating EXAFS

Because of the aforementioned limitations on analysing $\chi(k)$, rather than using a measured $\chi(k)$ to obtain a structural model in modern practice it is common to assume some structural model and calculate the theoretical $\chi(k)$. Modern software packages such as FEFF, developed by John Rehr at the University of Washington, can fully accommodate multiple atomic species, multiple scattering, relativistic effects from the potentials of heavy atoms, and also conduct a full curved-wave treatment of scattering (i.e. where the incident X-ray is not treated as a plane wave and the core state is not treated as a delta function) [68,69]. In FEFF multiple scattering is treated in technique used by Lee, discussed above [64, 70].

FEFF calculates $\chi(k)$ for a specified absorber atom surrounded by a cluster of neighbours. No crystal symmetry or periodic boundary conditions are taken into account, and if there are multiple absorber sites then the results of multiple calculations will have to be combined to reproduce the experimental spectra. FEFF calculates individual scattering paths, each composed of two or more legs. Each leg represents the motion of the electron from one atom to another; the entire path represents the full motion of the electron as it leaves the core, backscatters off of one

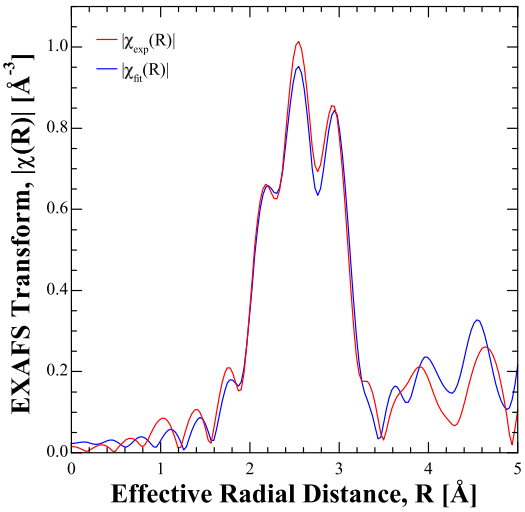

Figure 4.2: The theoretical EXAFS from gold fit to a measurement from a gold reference foil.

or more neighbouring atoms, then reflects back to the core modifying the absorption coefficient.

In practice FEFF is used to calculate the EXAFS amplitude function $f_j(k)$, the electron mean free path $\lambda(k)$, and the phase shifts $\phi_j(k)$ and $\delta(k)$. The assumed crystal structure provides the number of nearest neighbours N_j and the distances R_j. The root mean square component of the Debye-Waller factor σ_j (referred to hereafter as simply "the Debye-Waller factor", following the convention common in EXAFS literature) and the overall amplitude reduction factor S_0^2 are free parameters. The latest editions of FEFF can calculate σ_j and S_0^2 theoretically [71], but the work in this thesis used the older FEFF6L and these parameters must be chosen beforehand. An example of an EXAFS calculation and a measured EXAFS from a gold reference foil is shown in Figure 4.2. (Note that the fitting in Figure 4.2 is not particularly good by the standards of EXAFS, this is mostly because the reference foil was measured concurrently with an aSe:x%As film as a calibration for the As K-edge. In particular the energy range of the EXAFS scan was optimized for the As K-edge, not the Au L_3 edge, so the reference foil EXAFS is not of very high quality.)

The calculated $\chi_{calc}(k)$ is usually compared to the experimental $\chi_{exp}(k)$ through least-squares fitting, minimizing ξ^2 in Equation 4.9 [72]. In Equation 4.9 N_k is the number of independent points in k-space, N_I is the total number of independent points (see Equation 4.11, below), and ε is the estimated average uncertainty in the measurement. In this fitting approach S_0^2, σ_j are varied to obtain the best fit. Additionally an energy correction term ΔE_0 which modifies k, and a distance correction term ΔR_j which modifies R_j are often included to modify the phase and length of the calculated scattering path, respectively. Finally at high temperatures the thermal disorder is not strictly Gaussian, as was assumed in Equation 4.7, and in that case a third cumulant $-\frac{4}{3}k^3C_3$ may be added to the sin() and a fourth cumulant $-\frac{2}{3}k^4C_4$ may be added to the Gaussian exponent [72].

$$\xi^2 = \frac{N_k}{2N\varepsilon^2}\sum^{N_k} i = 1\left[\left(\Re\left(\chi_{exp}(k_i) - \chi_{fit}(k_i)\right)\right)^2 + \left(\Im\left(\chi_{exp}(k_i) - \chi_{fit}(k_i)\right)\right)^2\right] \quad (4.9)$$

The actual fitting process is conducted with IFEFFIT, a command-line interface written by Matt Newville [73], and the *Horae* suite of programs written by Bruce Ravel [74] which provide a graphical interface to IFEFFIT. The quality of the fit may be gauged by the $\mathcal{R}$-factor given by Equation 4.10 (where k^n indicates the k-weight n), for which values below ~ 0.02 indicate statistically good fits [75].

$$\mathcal{R} = \frac{\sum_{i=1}^{N_k}\left[\left(\Re\left(k^n\chi_{exp}(k_i) - k^n\chi_{fit}(k_i)\right)\right)^2 + \left(\Im\left(k^n\chi_{exp}(k_i) - k^n\chi_{fit}(k_i)\right)\right)^2\right]}{\sum_{i=1}^{N_k}\left[\left(\Re\left(k^n\chi_{exp}(k_i)\right)\right)^2 + \left(\Im\left(k^n\chi_{exp}(k_i)\right)\right)^2\right]} \quad (4.10)$$

In principle the six fitting variables S_0^2, σ_j, ΔR_j, ΔE_0, C_3 and C_4 may be floated for each scattering path, however this should be avoided. Since $\chi(k)$ is effectively oscillatory the Nyquist limit provides a boundary on the number of independent data points in an EXAFS spectrum [76]. The number of independent data points N is given by equation 4.11 where δk and δR are the useful ranges of the spectrum in k-space and its transform in R-space, respectively.

$$N = \frac{2}{\pi}\delta k\delta R \quad (4.11)$$

Because of the information limit it is important that the number of fitted parameters not exceed the number of independent data points given by Equation 4.11. This is often desirable: If each path is fitted independently the results do not give much information about the actual material structure, and if it is necessary to float each path independently to fit the data to the experiment then the original assumed structure is probably incorrect. It is far better practice to link the paths together with common fitting variables. For example it usually makes physical sense to keep S_0^2 and ΔE_0 consistent for all fitting paths. Similarly the Debye-Waller factors σ_j might be consistent for all atoms of the same species, and the changes in path length ΔR_j might be fixed as proportional to the original distance R_j. The relationship between the variables in each path should be indicative of the expected distortions in the crystal structure [72].

4.3 Background Subtraction and Data Preprocessing

The EXAFS oscillations $\chi(E)$ are obtained from the measured absorption via Equation 3.7. The background absorption coefficient μ_0 can be calculated as the absorption from an isolated atom. Ideally this atomic absorption follows the Victoreen formula given by Equation 4.12 for X-ray wavelength λ [77, 78]. The coefficients C and D can be obtained from standard tables or from fitting to the pre-edge absorption spectrum.

$$\mu \sim C\lambda^3 + D\lambda^4 \tag{4.12}$$

In practice this method is rarely used. Instead the measured μ is normalized by fitting a polynomial to the pre-edge portion and an n-point cubic spline to the post-edge portion. This is done automatically using the AUTOBK program written by M. Newville [79], which is part of IFEFFIT [73]. An example of an EXAFS spectrum, the background, and the EXAFS oscillations are shown in Figure 4.3.

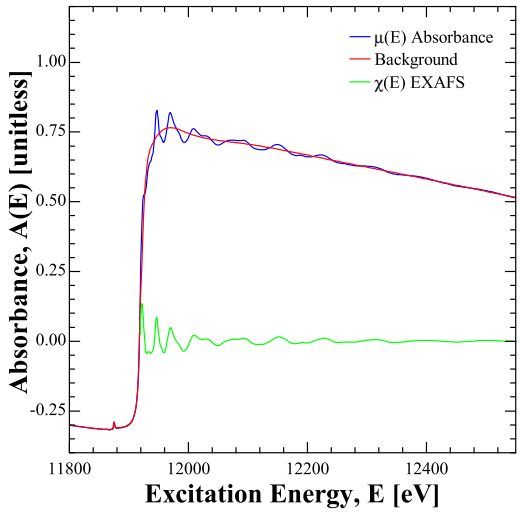

Figure 4.3: An L_3 EXAFS $\mu(E)$ spectrum of gold. The background was calculated with IFEFFIT, and the extracted EXAFS oscillations $\chi(E)$ are shown.

The EXAFS $\chi(E)$ is easily extracted from the normalized $\mu(E)$ simply by subtracting 1 and ignoring the low-energy XANES features. χ is usually expressed in terms of electron momentum $k = \sqrt{\frac{2m_e}{\hbar^2}(E - E_0)}$, where E_0 is the energy of the absorption threshold. The exact position of E_0 is usually not clear from the spectra: there can often be large pre-edge features which represent transitions to bound states. Therefore it is common to take the energy of the peak of the first derivative at the absorption threshold as E_0. Since EXAFS fitting involves the floated parameter ΔE_0 the exact position of E_0 is not crucial and can be refined after fitting.

For display purposes the EXAFS oscillation $\chi(k)$ is often weighted by k^n for $n = 1, 2, 3$. This process visually enhances the oscillations at high k which are usually extremely weak but are also fairly important for EXAFS analysis. Indeed the calculated weighted $k^n\chi(k)$ is often fitted to the weighted experimental data; this has the effect of enhancing the contribution of distant neighbours. A rigourous EXAFS fit should be independent of the choice of k-weighting, so comparing fittings with multiple k-weights can sometimes help in decoupling the fitting parameters.

4.4 First Shell Fitting

One of the benefits of calculating the individual scattering paths (the technique that FEFF uses) is that an EXAFS fit can be performed in either k- or R-space (an expression analogous to Equation 4.9 for R-space is obtained by simply replacing k with R). As long as the R-space fit is made with both the real and imaginary parts the two fits are essentially equivalent.

One advantage in fitting in R-space is that it allows fitting a structure to a selected distance range. One technique that is often used for preliminary characterization of a data set is "First shell fitting". Here the R-space fit is limited to the nearest scattering atoms at low R. First the useful range in k-space is chosen such that the low energy XANES features and high energy noise are excluded. The limited k range is then transformed to R-space, and the data is fit to the R-space transforms of the scattering paths. Since they are calculated, the R-space transforms of the scattering paths are just as accurate as the calculated paths in k-space, and the information loss encountered by transforming the measured spectra is minimal.

First shell fitting is a relatively easy way to estimate the type and number of nearest neighbours without trying to obtain the longer ranged structure. Although the limited R-range often significantly reduces the number of independent data points given by equation 4.11, there are usually sufficient data points to accurately fit a single scattering path. Since this thesis deals with amorphous materials with very little long-range order, first shell fitting is a useful technique for easily characterizing the differences between samples.

Chapter 5

Density Functional Theory

Density functional theory (DFT) is a fairly efficient and flexible technique for calculating the band structure and electronic properties of materials. While the bulk of this research has focused on EXAFS, which is accurately calculated by a single electron model with "muffin-tin" potentials, the XANES and XES data acquired in this project was interpreted with the aid of DFT calculations performed using the WIEN2k [80] and StoBe [81] software packages. The following sections briefly describe the theoretical basis and practical approach to DFT calculations using the aforementioned software packages.

5.1 A Self-Interacting Electron Gas

The many-body problem of finding the ground state energy of a system of many electrons and atomic nuclei is obviously a very complex one. For N_i number of atoms of species i with atomic number Z_i and n species of atoms the problem involves finding simultaneous solutions for $\sum_i^n N_i (1 + Z_i)$ particles (under the assumption that the nuclei can be treated as a single particle). Indeed, the full many-body Hamiltonian for this system is given by Equation 5.1 [82].

$$\begin{aligned}\mathbb{H} = &- \frac{\hbar^2}{2}\sum_i \frac{\nabla^2_{\vec{R}_i}}{M_i} - \frac{\hbar^2}{2}\sum_i \frac{\nabla^2_{\vec{r}_i}}{m_e} - \frac{1}{4\pi\epsilon_0}\sum_{i,j}\frac{e^2 Z_i}{\left|\vec{R}_i - \vec{r}_j\right|} \\ &+ \frac{1}{8\pi\epsilon_0}\sum_{i\neq j}\frac{e^2}{|\vec{r}_i - \vec{r}_j|} + \frac{1}{8\pi\epsilon_0}\sum_{i\neq j}\frac{e^2 Z_i Z_j}{\left|\vec{R}_i - \vec{R}_j\right|}\end{aligned} \tag{5.1}$$

In Equation 5.1, R_i and M_i are the position and mass of nucleus i, respectively,

and r_i and m_e are the position and mass of electron i, respectively (obviously the mass is the same for all electrons). The last three terms in Equation 5.1 describe the Coulomb interactions between the nuclei and the electrons, and the presence of the double sum in each makes this Hamiltonian intractable. A reasonably accurate solution to the Hamiltonian may be acquired, however, under some simplifying approximations.

The first major step in solving this problem came from Hohenberg and Kohn [83, 84]. Following their procedure, we consider the case of a self-interacting electron gas under some external potential $V(\vec{r})_{ext}$, described by Equation 5.2 [85]. Here $\mathbb{T}$ and $\mathbb{U}$ are the electron kinetic energy and electron-electron interaction operators, respectively, as described by the second and fourth terms in Equation 5.1, respectively.

$$\mathbb{H} = \mathbb{T} + \mathbb{U} + \sum_i V(\vec{r}_i) \tag{5.2}$$

For a ground state wavefunction $|\psi_0\rangle$, the ground state particle density is given by $n(\vec{r}) = \sum_i \langle\psi_0|\delta(\vec{r} - \vec{r}_i)|\psi_0\rangle$ [84]. In terms of the ground state density, the dynamics of the system are described by Equation 5.3.

$$\begin{aligned} E[n] &= \langle\psi_0|\mathbb{T} + \mathbb{U}|\psi_0\rangle + \int d\vec{r} n(\vec{r}) V_{ext}(\vec{r}) \\ &= F[n] + \int d\vec{r} n(\vec{r}) V_{ext}(\vec{r}) \end{aligned} \tag{5.3}$$

An immediate result of Equation 5.3 is that contribution to the total energy from the kinetic energy and mutual interaction of the electrons is contained in the functional $F[n]$, and this functional is independent of the external potential. In other words, the functional $F[n]$ is the same for *any* material, regardless of its crystal structure. The most important theory of Hohenberg and Kohn, however, is that the ground state density has a one-to-one correspondence to the external potential [85]. The proof is as follows (see Reference [85] for more detail): consider two different external potentials $V_1(\vec{r})$ and $V_2(\vec{r})$ (i.e. V_1 and V_2 differ by more than just a constant), with associated Hamiltonians $\mathbb{H}_1$ and $\mathbb{H}_2$ and associated ground state

wavefunctions $|\psi_0^1\rangle$ and $|\psi_0^2\rangle$. Assume for the moment that somehow the ground state densities are the same for both systems. Since $|\psi_0^{(1,2)}\rangle$ are the the ground state wavefunctions, they have the minimum energy for each system (E_1 and E_2, respectively). Therefore the energy of Hamiltonian $\mathbb{H}_1$ operating on wavefunction $|\psi_0^2\rangle$ is greater than E_1:

$$\begin{aligned} E_1 &= \langle\psi_0^1|\mathbb{H}_1|\psi_0^1\rangle \\ &< \langle\psi_0^2|\mathbb{H}_1|\psi_0^2\rangle \end{aligned} \tag{5.4}$$

Since $\mathbb{H}_1$ and $\mathbb{H}_2$ differ only by the external potentials, we can write:

$$\begin{aligned} E_1 &< \langle\psi_0^2|\mathbb{H}_2 + V_1 - V_2|\psi_0^2\rangle \\ &< E_2 + \int d\vec{r}\,(V_1(\vec{r}) - V_2(\vec{r}))\,n(\vec{r}) \end{aligned} \tag{5.5}$$

Following the same procedure with the alternative indices we obtain:

$$E_2 < E_1 - \int d\vec{r}\,(V_1(\vec{r}) - V_2(\vec{r}))\,n(\vec{r}) \tag{5.6}$$

Adding Equations 5.5 and 5.6 suggests that $E_1 + E_2 < E_1 + E_2$, a clear contradiction. Therefore a distinct external potential is sufficient to define a unique ground state density, and conversely each ground state density is sufficient to define a unique external potential. The ramifications of this theory are profound: if the inter-electron dynamics ($F[n]$) are a functional of the ground state density, which is uniquely defined by the external potential, then *any* observable of the system can be derived from $n(\vec{r})$. Soon after Hohenberg and Kohn's work was published Mermin generalized their results to finite temperatures [86].

5.2 Electrons in a Solid

In some respects the electrons in a solid can be treated as an inhomogeneous, self-interacting electron gas which has an additional interaction with the atomic nuclei.

Since the atomic nuclei are considerably more massive than the electrons, they are often treated as static charges (the Born-Oppenheimer approximation) [83]. The nuclear kinetic energy term in Equation 5.1 is then zero, and the nuclear self-interaction term is simply a constant. If the Born-Oppenheimer approximation is used then the effect of the nuclei is simply an external potential, and the electron gas of Hohenberg and Kohn is recovered. Unfortunately while Hohenberg and Kohn illustrate the importance of $n(\vec{r})$, they offer no prescription for finding it [82]. The end result of Hohenberg and Kohn is Equation 5.7, where $n_1(\vec{r},\vec{r}')$ is the one-particle density matrix, and $C_2(\vec{r},\vec{r}')$ is the two-particle correlation function [85]. This equation still cannot be solved analytically.

$$
\begin{aligned}
E[n] &= \int d\vec{r} V_{ext}(\vec{r}) n(\vec{r}) + \frac{e^2}{8\pi\epsilon_0} \int d\vec{r} d\vec{r}' \frac{n(\vec{r}) n(\vec{r}')}{|\vec{r}-\vec{r}'|} + T[n] + E_{xc}[n] \qquad (5.7)\\
T[n] &= \frac{\hbar^2}{2m_e} \int d\vec{r} d\vec{r}' \nabla_{\vec{r}} \nabla_{\vec{r}'} n_1(\vec{r},\vec{r}')|_{\vec{r}=\vec{r}'}\\
E_{xc}[n] &= \frac{\hbar^2}{2m_e} \int d\vec{r} d\vec{r} \frac{C_2(\vec{r},\vec{r}')}{|\vec{r}-\vec{r}'|}
\end{aligned}
$$

A method for solving Equation 5.7 was provided by Kohn and Sham [87] based on two approximations summarized as follows [84]:

1. The ground state density is equivalent to the ground state of a collection of non-interacting particles in an auxiliary system.

2. The Hamiltonian for the auxiliary system is constructed with the normal kinetic energy operator, but the auxiliary potential is treated as an effective local potential.

These approximations work best for $n(\vec{r})$s which are smooth and slowly varying [87], however they work quite well in a number of practical applications [84]. The new Hamiltonian is given by Equation 5.8, where the electron-electron repulsion is given by the Hartree-Fock potential.

$$\mathbb{H} = -\frac{\hbar^2}{2m_e}\sum_i \nabla^2_{\vec{r}_i} + \frac{e^2}{4\pi\epsilon_0}\int d\vec{r}' \frac{n(\vec{r}')}{|\vec{r}-\vec{r}'|} + V_{xc} + V_{ext} \tag{5.8}$$

$$V_{xc} = \frac{\delta E_{xc}[n]}{\delta n}$$

$$E_{xc}[n] = \int d\vec{r} n(\vec{r})\epsilon_{xc})$$

With the above Hamiltonian, a process for solving the system is available. The basic theory obtained by Kohn and Sham theory suggests that the *exact* ground state density of an N-electron system $n(\vec{r})$ can be assembled from a set of single-particle wavefunctions $\phi_i(\vec{r})$ which are the N lowest-energy solutions to the Hamiltonian in Equation 5.8 [82]. Since the new Hamiltonian makes a set of linear Schrödinger equations, we have an approach for an analytic solution. It is important to point out that the single-particle wavefunctions $\phi_i(\vec{r})$ are *not* the actual wavefunctions of the electrons. The "single-particles" they represent are fictitious and only the combination of all the fictitious "single-particle" wavefunctions produces a physically relevant result [82].

In order to solve Equation 5.8, we need an expression for the exchange-correlation potential, ϵ_{xc}. One of the simplest, and yet quite accurate, approximations for ϵ_{xc} is the local density approximation (LDA). Here ϵ_{xc} is a function of $n(\vec{r})$ only. An extension to LDA is the generalized gradient approximation (GGA), where ϵ_{xc} is a function of both $n(\vec{r})$ and $\nabla_{\vec{r}} n(\vec{r})$. Using the actual gradient $\nabla_{\vec{r}} n(\vec{r})$ directly is actually worse than LDA, because the approximated gradient tends to behave in an unphysical manner at very small and very large values of $\vec{r}$ [88]. The "generalized" gradient fixes these problems, and as a result usually produces better results than LDA [84]. The exact process of "generalizing" a gradient is not unique, however, and several different versions exist. See References [89–91] for example.

The actual method of solving Equation 5.8 is an iterative process. An initial guess of $n_0(\vec{r})$ is made, and the single-particle wavefunctions $\phi_i(\vec{r})$ are decomposed into a suitable basis set [82]. The equations are solved using the guessed $n_0(\vec{r})$, and the resulting $\phi_i(\vec{r})$ are obtained. These can then be used to construct a $n_1(\vec{r})$, which

is then reinserted into the Hamiltonian in Equation 5.8 to solve for a new set of $\phi_i(\vec{r})$ wavefunctions. This process continues until the difference between successive ground states $n_i(\vec{r})$ and $n_{i-1}(\vec{r})$ is within some pre-defined tolerance [84].

It is of interest to point out that while the work of Hohenberg and Kohn on the dynamics of an inhomogeneous electron gas and the use of the Born-Oppenheimer approximation by Kohn and Sham lead to the formulation of DFT; DFT itself is not limited to those constraints. DFT has also been applied to proton-neutron "gases" to construct models of atomic nuclei, and the Born-Oppenheimer approximation can be dropped altogether to model lattice distortions or materials with very light elements [82].

5.3 WIEN2k Software

The WIEN2k program, developed by Karlheinz Schwarz and Peter Blaha at the Technische Universität Wien, is an augmented plane wave (APW) and local orbital (LO) approach to DFT calculations [80]. WIEN2k is designed for crystalline materials, and takes full advantage of crystalline symmetry and periodic boundary conditions to reduce the complexity of the problem.

In WIEN2k the basis functions are APWs [80]. These functions take the form of spherical harmonics within a characteristic radius of the nuclei (referred to as the "muffin-tin" radius, R_{MT}), and smoothly transition to Bloch-type plane waves in the regions between nuclei (the interstitial region), given by Equation 5.9 [82].

$$\phi_{\vec{K}}^{\vec{k}}(\vec{r},E) = \begin{cases} \frac{1}{\sqrt{V}} \exp\left(i\left(\vec{k}+\vec{K}\right)\cdot\vec{r}\right) & r \notin R_{MT}^{i} \\ \sum_{\ell,m} A_{\ell,m}^{i,\vec{k}+\vec{K}} \mu_{\ell}^{i}(r,E)\, Y_{m}^{\ell}(\hat{r}) & r \in R_{MT}^{i} \end{cases} \tag{5.9}$$

In the above equation V is the unit-cell volume, μ_ℓ^i is the radial portion of the spherical wave, Y_m^ℓ is the spherical harmonic, and R_{MT}^i is used as a short-hand for denoting when $\vec{r}$ is within the "muffin-tin" radius of nuclei i or in the interstitial region. Both $A_{\ell,m}^{i,\vec{k}+\vec{K}}$ and energy E are parameters that are calculated during the iterative cycles.

The presence of the unknown energy E in the radial portion μ_ℓ^i makes these equations fairly difficult to solve, and in practice linearized augmented plane waves (LAPWs) are almost always used instead. Here the term "linearized" refers to the fact that a first order expansion of the radial component μ_ℓ^α about a known energy E_0 is used, making the equation linear in energy E as shown in Equation 5.10 [82].

$$\phi_{\vec{K}}^{\vec{k}}(\vec{r},E)=\begin{cases}\frac{1}{\sqrt{V}}\exp\left(i\left(\vec{k}+\vec{K}\right)\cdot\vec{r}\right) & r\notin R_{MT}^i\\ \sum_{\ell,m}A_{\ell,m}^{i,\vec{k}+\vec{K}}\left(\mu_\ell^i\left(r,E_0\right)+\left(E_0-E\right)\frac{\partial}{\partial E}\mu_\ell^i\left(r,E\right)\big|_{E=E_0}\right)Y_m^\ell\left(\hat{r}\right) & r\in R_{MT}^i\end{cases} \tag{5.10}$$

In principle all electrons can be treated with a (L)APW basis, but it is usually only used for valence states. The core electrons are very tightly bound to the nuclei, are always within R_{MT}, and are essentially the same as those in a free atom (although they may have a slightly different binding energy than the free atom case). To save time the free atom orbitals are often used for these states. To treat "semi-core" states which are not valence level but still extend quite close to R_{MT} (such as, for example, Se *3d* states) the LAPW (or APW) basis set can be further modified by adding local orbitals (LOs) to it. These are like those in Equation 5.10 save there are no plane waves (i.e. $\phi(\vec{r})=0$ for $\vec{r}\notin R_{MT}^i$) and an additional radial function with a second energy E_2 is added to the part inside R_{MT}^i. LOs usually represent semi-core states very accurately, and are much quicker to compute than the large number of regular LAPW functions it would take to describe such a state [82].

Setting up a WIEN2k calculation is fairly straightforward. The unit cell needs to be described, and the R_{MT}^i values chosen. Usually these are selected in such a way that the atomic spheres from neighbouring atoms are almost touching, as this greatly reduces the number of plane-wave components required without significantly affecting the accuracy of the calculation. As suggested by Equation 5.10, the actual iterative cycles are conducting in reciprocal space ($\vec{k}$-space). A grid of $\vec{k}$ points must be specified; the calculation will only be evaluated at these points and interpolated in between. In the calculations I performed, about 1000 $\vec{k}$ points are typically used, corresponding to a $10\times10\times10$ grid for a cubic unit cell. Finally the maximum

expansion of plane waves must be specified. The best figure-of-merit for plane wave expansion is fixing the product of the maximum wave vector K_{max} and the minimum atomic sphere R_{MT}^{min} to a specific value [82], usually ~ 7 is sufficiently accurate [80].

WIEN2k is a very flexible program; it is scalar relativistic and can perform spin-polarized LSDA or GGA calculations, fixed-spin calculations, and antiferromagnetic calculations. It can also incorporate Hubbard-like potentials (the so-called LSDA+U or GGA+U calculations), spin-orbit interactions, and hybrid exchange functionals (usually Hartree-Fock like on-site exchange functionals) for correlated systems [80]. In the context of this research a simple GGA calculation using the form derived by Perdew, Burke, and Ernzerhof (commonly called PBE96) [91] was sufficient.

5.4 StoBe Software

The StoBe-deMon program, developed primarily by Klaus Hermann of the Fritz-Haber-Institut der Max-Planck-Gesellschaft and Lars Pettersson of Stockholm University, is a linear combination of atomic orbitals (LCAO) using a Gaussian type orbitals (GTO) approach to DFT calculations [81]. StoBe is designed for clusters and molecules, and takes advantage of the vacuum surrounding isolated geometries to truncate basis function expansions.

The basis sets used by StoBe are basically the same as the spherical wave functions used by WIEN2k, save the radial component involves a Gaussian (recall that for a free atom the radial component involves a $\sim \exp(-cr)$ term), as described by Equation 5.11 [92].

$$\phi_{\ell,m}^{i}(\vec{r}) = \sum_{\ell,m} A_{\ell,m}^{i} r^{\ell} \exp\left(-\alpha r^{2}\right) Y_{m}^{\ell}\left(\hat{r}\right) \tag{5.11}$$

While it takes a large number of GTOs to accurately describe electron behaviour near the nuclei, since they quickly truncate at large $\vec{r}$, they are particularly suitable for isolated systems.

Like WIEN2k, StoBe is a very flexible program for calculating cluster, surface,

and molecular systems. The exchange-correlation potential can be specified in three parts; the overall type (local, non-local, or mixed), the type used for the exchange potential, and the type used for the correlation potential (the latter two are typically standard GGA forms like PBE96, as previously discussed). The basis sets for each atom and angular symmetry must be specified for valence (using the "auxiliary" keyword, basis sets for both charge density and exchange-correlation must be provided), core (using the "orbital" keyword), and model core potentials (using the "potential" keyword) states.

For the purposes of this research, StoBe was used to model the XAS from small clusters of disordered ring-like or chain-like Se. The non-local Becke [89] potential was used for the exchange potential, and the non-local Perdew [93] potential was used for the correlation potential.

5.5 Core-hole Effect

The X-ray absorption or emission spectra can be calculated with WIEN2k by multiplying the dipole-allowed DOS with the transition probabilities [94]. The ground state calculation works well for XES, but properly treating the core-hole effect in XAS requires a bit more effort. The most straightforward, and probably the best, method of including the effect of the core-hole is to generate a supercell (at least $2 \times 2 \times 2$ normal cells) and remove the appropriate core electron from one of the absorbing atoms. This electron can be placed in the conduction band for a near-edge XAS calculation (for "pre-edge states), or added as a background charge for higher energy XAS states (nearing the EXAFS region).

While X-ray spectra is merely a side-feature of WIEN2k, it is one of the main aspects of a StoBe calculation. In this respect the core-hole effect is, perhaps, dealt with more accurately in StoBe. For a proper XAS spectra three calculations are performed; a ground state model, a transition model, and an excited state model. Because of the choice of orbital functions and pseudopotentials in StoBe calculations a fractional core-hole is often a better choice than removing an electron completely.

Chapter 6

Sample Preparation and X-ray Measurements

Over 300 X-ray spectra have thus far been obtained in this research. Amorphous, polycrystalline, and crystalline selenium as well as arsenic-selenium alloys with 0.2%, 0.5%, 2%, 6%, 10%, 19%, and 39% were synthesized and studied. The following sections outline the preparation and measurement of the samples.

6.1 Sample Preparation

The selenium films were prepared by members of Safa Kasap's group, specifically George Belev and Dan Tonchev, in the Department of Electrical Engineering at the University of Saskatchewan. The samples were prepared by vapour deposition of pure (99.999%) selenium and arsenic-selenium alloys on 0.5 mm polycarbonate or aluminum foil substrates [95]. The different arsenic concentrations in the arsenic-selenium alloys were 0.2%, 0.5%, 2%, 6%, 10%, 19%, and 39% (the last is arsenic triselenide; As_2Se_3) by atomic composition. The process occurred as follows: a crucible of selenium or arsenic-selenium alloy was heated to a boil in a low pressure chamber. The resulting vapour rose to the top of the chamber where it cooled and solidified on the underside of the substrates. This vapour deposition process formed homogenous films and the process lasted until the films were between 24 μm and 35 μm thick. This range of thickness was chosen to give an absorption step of roughly 2 at the the selenium K-edge. The thickness of the films was checked afterwards with a micrometer by averaging several thicknesses across the sample face. A metal

mask was used to create specific geometries of film; the most common one used was a circle of 5 mm diameter.

Most of the samples were deposited on room-temperature substrate, although some were deposited on cold (held at $\sim 5^\circ$ C) or hot (held at $\sim 50^\circ$ C) substrate. The substrate temperature has a significant impact on the hole lifetime and mobility [4, 32]. A cold substrate decreases the transition time between the vapour phase and the amorphous solid phase, and is therefore expected to make the sample "more amorphous" [96]. Conversely, a heated substrate increases the transition time between the vapour phase and the solid phase, and is expected to increase the homogeneity surrounding defect sites [95].

Pure crystalline tSe and mSe crystals were grown for use as reference standards. The tSe crystals were grown from vapour produced from the sublimation of pure selenium kept at a temperature of 200°C in a closed glass vessel for 7-10 days. The crystals grown by this method have needle-like shape that is typical for tSe [97]. mSe crystals were grown by a saturated solution of selenium in methylene iodide (CH_2I_2) [98]. The tSe crystals were ground into a fine powder (less than 50 μm grain size). The mSe crystals were essentially grown in powder form, and were not further modified since mechanical stress is known to induce conversion to the trigonal phase [99]. These powders were homogeneously mixed with boron nitride to obtain sufficient volume to measure easily while keeping the optimal absorbance (note boron nitride is essentially transparent to hard X-rays). The ratio of selenium to boron nitride was chosen to produce a similar absorption step to that of the arsenic-selenium alloy films. Unfortunately the finest grain size for the tSe powder and the grain size of the mSe crystals were larger than the ideal thickness for selenium K-edge EXAFS, and the irregularity in the grains caused significant pin-hole effect problems in transmission measurements.

To examine the process of crystallization, some of the film samples were annealed in a convection oven. The film samples with 6% or less arsenic were annealed at 100°C for 24 hours. The annealing temperature was substantially higher than the highest glass transition temperature for these materials (about 80°C for the Se:6%As alloy).

The films with 10% and 19% arsenic were annealed for about 100 hours at 110°C (the maximum temperature of the furnace). This temperature was only slightly higher than the highest glass transition temperature (about 106°C for Se:19%As). Finally, aSe and aSe:10%As films were measured as prepared, and then remeasured immediately after annealing at 60°C, 80°C, and finally 100°C for three hours each.

6.2 X-ray Spectroscopy Measurements

These materials were extensively measured at various times and at various beamlines over a two year period. The basic outline of these measurements is given in Appendix A. The EXAFS and XANES measurements from the HXMA beamline were the most useful in this research. Of these, the room temperature transmission measurements of the Se K-edge, starting at 12 658 eV [100], were of excellent quality, with very low noise out to ∼1600 eV above the absorption edge ($k_{max} \sim 20$). Low temperature transmission measurements of the Se K-edge were also of good quality, but the added mechanical noise from the cryostat added a significant amount of noise to the spectra above $k \sim 16$. In all cases the Se data were calibrated to a common Se reference film measured jointly with the sample. Typically each measurement was repeated 2 or 3 times to check for consistency. To improve statistics the 2 or 3 scans were then averaged together. For the room temperature measurements, the reference was placed behind the sample and measured with a third ion chamber. In the case of low temperature measurements the reference was placed before the I_0 ion chamber at a very shallow grazing incidence to the beam, with a photodiode directly behind it. The absorption threshold E_0 was set to 12 658 eV [100] using the peak of the first derivative near the absorption edge.

The As K-edge starts at about 11 867 eV [100], which is unfortunately quite close to the Se K-edge. These measurements could only extend as far as $k_{max} \sim 14$. The concentration of As was sufficient to obtain transmission measurements for concentrations of 2% or more. These concentrations were still relatively low, and the poor statistics increased the noise in the spectrum occasionally further reducing the

useful k-range. Several scans with the 32-element germanium detector produced a decent quality measurement for the 0.2% and 0.5% As samples. The Saturn-Vortex measurements were all of rather poor quality. In all cases the As data were calibrated to a common Au reference film (for obvious health reasons a pure As reference was not available) set up in the same geometry as described for the Se reference film. The absorption threshold of the Au L_3 edge was set to 11 919 eV [100] using the peak of the first derivative near the absorption edge.

The tSe and mSe crystalline standards did not give very good transmission or fluorescence measurements. In the former case the grain sizes were too large for a homogenous sample, in the latter the high concentration of selenium caused excessive dead-time in the detector. The tSe data is of some use, while the detector dead-time caused the intensities of the EXAFS features to be supressed, the features do occur at the proper positions allowing some quantitative analysis. For mSe the noise in the spectrum precludes any EXAFS analysis, and these measurements are of qualitative value only.

Additional rather thin ($\sim$ 10 μm) and rather thick ($\sim$ 80μm) aSe films were measured to test the accuracy of the tabulated X-ray absorption cross-sections from the McMaster [101], Henke [55], Elam [100], Chantler [102], and Cromer-Liberman [103] databases. The measured absorption step was essentially the same as the predicted absorption step, as shown in Figure 6.2[1]. This result is not surprising. The slight discrepancy at the thin end is probably caused by pin-holes or fractures in the fragile film, which would have the effect of creating a smaller average thickness across the X-ray beam profile. The discrepancy at the thick end is probably caused by the thick film buckling against the substrate (the thicker films did not adhere well to the polycarbonate). When measured with a micrometer this would make the film appear thicker. Any cavities between the film and the substrate would be transparent to hard X-rays and have no effect on the absorption.

[1]Although obviously the Chantler database is significantly different than both the other four databases and my measurements. The Chantler database was, however, focused on improving accuracy for energies from 30 to 3000 eV, or above 30 keV [102], and the poor results at 13 keV are probably due to a simplistic extrapolation between the two extremes.

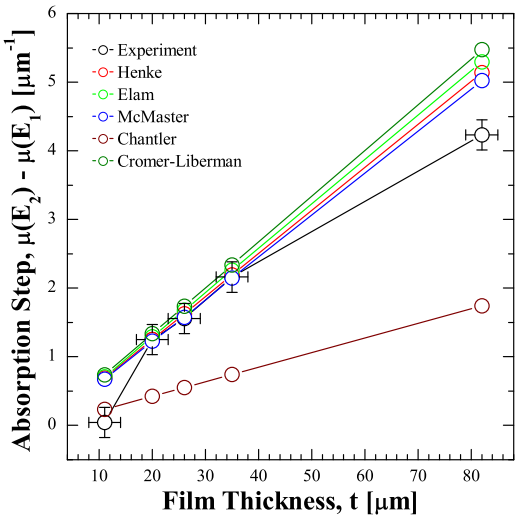

Figure 6.1: A comparison of the X-ray absorption step with respect to sample thickness derived from measurement and several X-ray databases. Here the absorption step was calculated as the difference $\mu(E_2 = E_0 + \Delta E) - \mu(E_1 = E_0 - \Delta E)$ where E_0 is the *1s* absorption threshold of Se (at 12658 eV) and $\Delta E = 30$ eV.

For the sake of interest the Se $L_{2,3}$-edge XANES was measured at the SGM beamline. The Se L_3- and L_2-edges occur at 1433.9 eV and 1474.3 eV [100], respectively. The Se $L_{2,3}$ spectra do not show any interesting features, nor do they show any sensitive dependence on crystallinity or arsenic concentration. I was unable to get a signal from the As $L_{2,3}$-edge XANES at 1323.6 eV and 1359.1 eV [100], probably due to the comparatively low concentrations of As (at the time As_2Se_3 samples were unavailable). This lack of spectral information is not unexpected; the valence states of Se and As are the $4p$ electrons, and by dipole selection rules the $2p$ absorption measurement would only probe the relatively unimportant and completely empty $4d$ states. The available literature on the Se $L_{2,3}$-edge only reports interesting results when the selenium is near a transition metal [104] or has hybridized states from a surrounding molecular system [105]. These measurements were not accurately calibrated since at the time I did not have a good reference sample for that energy range and the spectra were not used in any analysis. They are reported here only

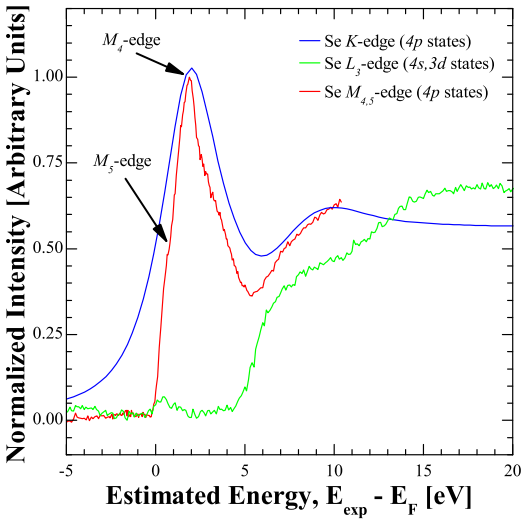

Figure 6.2: The Se K-, L_3-, and $M_{4,5}$-edge XANES for an aSe film. The spectra are aligned on a common energy scale by subtracting the theoretical binding energy from each measurement. This is only an estimate, a proper analysis would require core-level XPS measurements to determine the exact binding energy of the core electrons.

for completeness.

Finally the Se $M_{4,5}$-edge XANES and XES were measured at the PGM beamline and BL8, respectively. The Se $M_{4,5}$-edge occurs at 54.6 and 55.5 eV [100], an unusual energy range for soft X-ray beamlines. The $M_{4,5}$-edge is of interest since it excites $3d$ electrons which will, by the dipole selection rules, probe the $4p$ valence states. To that end the $M_{4,5}$-edge spectra will give complementary information to the K-edge spectra, but the $M_{4,5}$-edge spectra will have a much higher energy resolution. The Se K-, L_3-, and $M_{4,5}$-edge XANES are shown in Figure 6.2. The Se L_2-edge XANES is essentially the same as the L_3-edge XANES and is not shown. Note the similarity between the K- and $M_{4,5}$-edge XANES spectra.

The shape of the Se $M_{4,5}$-edge XANES measurement agree with the only available spectra in the literature [106]. The As $M_{4,5}$ edge has a similar shape to that of Se, the As $M_{4,5}$ edge occurs at $\sim$ 42 eV. The Se $M_{4,5}$ edge of tSe was calibrated to the values in the Elam database [100] which are the same as those reported by Givens [106].

The other spectra were then calibrated to tSe. Unfortunately the Se $M_{4,5}$-edge XES was not calibrated. Due to the limitations of the beamline, the grating spectrometer was centred on the Se $M_{4,5}$-edge but the monochromator could not go to that energy range. Instead the monochromator was tuned to $\sim$ 170 eV to hit the Se $M_{2,3}$-edge (*3p*-states) which could excite *3d*-states through their decay process. There was the additional benefit that the small amount of third order light from the undulator would be of the correct energy to excite the $M_{4,5}$ edge. Since there is no known spectrum of the Se $M_{4,5}$-edge available in the literature, and the absorption and emission spectra were measured at different beamlines, the XES data could not be calibrated. Because of this the XES is only used to provide a qualitative comparison to the calculated valence states.

Chapter 7

Structural Analysis

Determining a consistent long range structure for aSe:x%As is not a trivial task. Since aSe spontaneously crystallizes at room temperature, the amorphous structure should not be too far removed from the trigonal crystalline structure. However it is also clear that the structure of aSe should not have any long range order. The following sections outline the preliminary analysis of the EXAFS spectra and the implications the spectra have on the possible structure of aSe.

7.1 First Shell Analysis

The first shell, loosely defined as the region in R-space from 1 Å to 3 Å, was fit for all EXAFS data sets. The fitting was performed in R-space (using the full real and imaginary data sets) with a k-weight of 2. Only a single path was fit — the single scattering path between the core atom and its nearest neighbour. Since the arsenic concentrations in all samples except As_2Se_3 was quite low, the scattering from an Se core atom was assumed to be off an Se neighbour. Obviously some of the scattering paths in the As-doped materials will be from Se to As atoms, but since the scattering factors of As and Se are almost identical [107] this simple model is sufficient for a first shell analysis. Since the structure of As_2Se_3 consists of a "web" with the As coordinated to 3 Se atoms and with the Se atoms coordinated to 2 As atoms [108], for As_2Se_3 an Se to As scattering path was assumed.

For each data set four parameters were floated and determined by the fit. These were NS_0^2, σ^2, Δr, and ΔE_0. Here the term NS_0^2 is used because the multiplicity of the scattering path, N (i.e. the number of nearest neighbours) cannot be decoupled

from the amplitude reduction factor S_0^2 (expected to be somewhere between ~ 0.6 and ~ 1.0). The variable σ^2 represents the mean (Gaussian) displacement of the scattering atoms. This is usually due mostly to thermal vibrations, but can also be caused by minor structural disorder [69]. The variable Δr represents the average deviation from the ideal bond length, which was assumed to be 2.32 Å in the calculated scattering paths [28]. Finally ΔE_0 represents the shift from the absorption threshold energy, assumed to be located at the peak of the first derivative at the absorption edge. Although the ΔE_0 parameter is of no physical interest, choosing the E_0 energy by inspecting the first derivative of the absorption is arbitrary, and the true E_0 is almost always at higher energies. However E_0 cannot be accurately determined by merely inspecting the spectrum, and therefore ΔE_0 should be a floated parameter. It should be pointed out that it might be reasonable to assume that the S_0^2 parameter should be the same for all Se K-edge (or As K-edge) measurements, or perhaps for all Se K-edge (or As K-edge) measurements at a specific temperature. Keeping S_0^2 consistent across multiple datasets would allow it to be decoupled from the number of nearest neighbours (represented by N). However even in an ideal case EXAFS can only determine the number of nearest neighbours to within an error of $\sim \pm 25\%$ [109], and since these measurements were taken at several different times each with slightly different equipment set-up, it is probably best to keep the two variables coupled together.

First shell fitting of the entire EXAFS data set is an important check on the fidelity of the data. We expect similar samples to have similar bond lengths, structural and thermal disorder, and number of nearest neighbours. Since Se and As have 4 and 3 *4p* valence electrons, respectively, we expect Se and As to be bonded to 2 and 3 neighbours, respectively (on average, anyway). Numerically, the Debye-Waller factor σ^2 should be greater than ~ 0.0006 Å^2 [110] and ΔE_0 should be positive. If the results for a data set deviate from these values, or are far from the results from similar materials, this is an indication that perhaps something was wrong with the sample or the measurement and that data set should be discarded from further analysis.

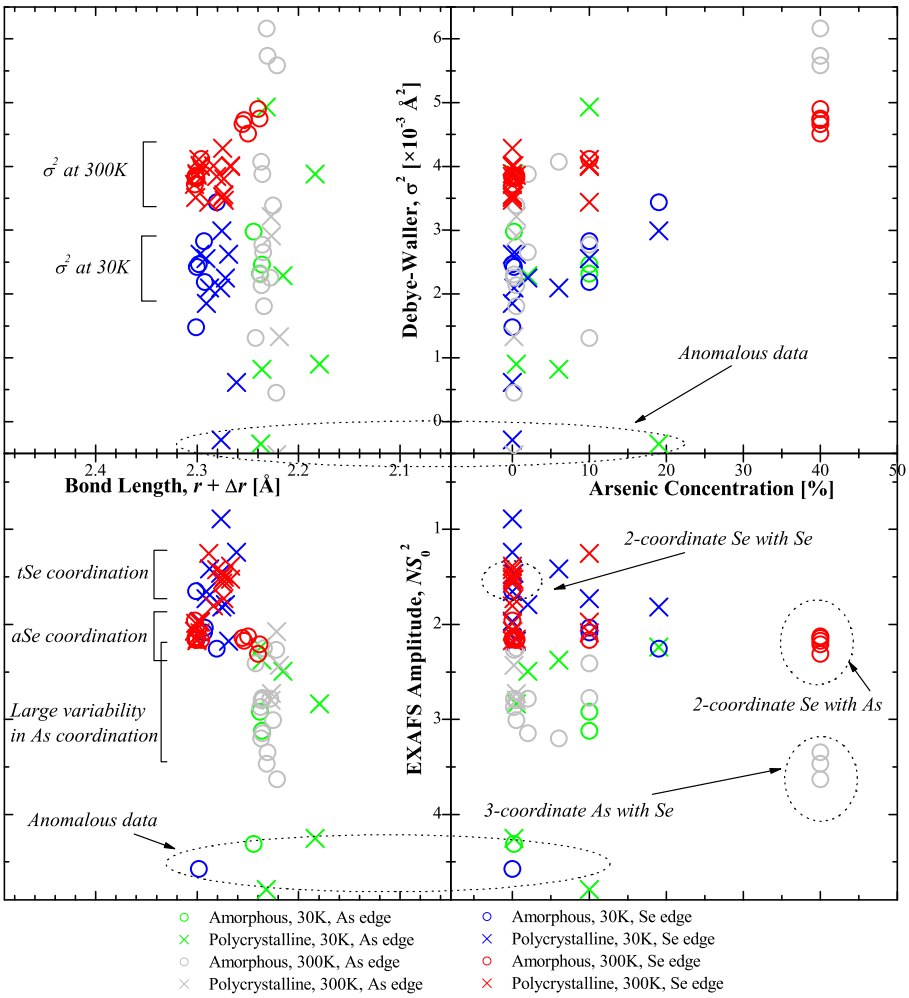

Figure 7.1: The fitting values for first shell fitting of all datasets. Each point represents a complete EXAFS measurement. Important clusters of points are labeled. Data points that have anomalously low σ^2 or anomalously high NS_0^2 values are also identified. In this figure, all samples that have been annealed are labeled as "polycrystalline".

The fitted structural parameters NS_0^2, σ^2, and $r + \Delta r$ and the arsenic concentration for all datasets are shown in Figure 7.1. Here each datapoint represents a complete measurement, and each measurement is shown in each of the 4 panels of the graph. Plotting the results in this manner makes visual analysis of the results easy. For example, since the Debye-Waller factor partially measures thermal disorder, we expect the σ^2 values for low temperature (T $\sim$ 30 K) measurements to be smaller than room temperature (T $\sim$ 300 K) measurements. Looking at the top half of Figure 7.1 we see this is indeed the case for Se K-edge measurements.

In the top half of Figure 7.1, we see that there appears to be a slight difference in bond length between As-Se bonds probed by As K-edge EXAFS, and Se-Se bonds probed by Se K-edge EXAFS. Note that the cluster of 5 points from room temperature Se K-edge EXAFS that overlap with the As-Se bond length are from amorphous As_2Se_3 (trace horizontally across the common σ^2 axis to see that these points contain 40% As), so indeed these are As-Se bonds. As previously mentioned, this quadrant shows a clear grouping of room temperature and low temperature σ^2, as we expect. The σ_2 disorder around As atoms, however, varies quite a bit and shows no dependence on temperature.

In the bottom half of Figure 7.1 we see that there is a separation in the coupled amplitude reduction and number of neighbours parameter (the NS_0^2 variable) based on polycrystallinity in the Se K-edge EXAFS. This is somewhat expected; previous reports on the subject suggest that aSe has a higher coordination number than tSe [8]. There is no real temperature dependence, which is good; lowering the temperature should not increase the number of nearest neighbours. There is still a significant spread in NS_0^2, especially for pure polycrystalline Se. This either suggests a significant variability in the length of helical chains in the crystal structure or that many of the samples have cracks or pin-holes. For the first case, since a Se atom at the terminal end of a chain has only 1 bonded neighbour, many short chains would therefore reduce the average number of neighbours for the material from the ideal value of 2, and therefore would affect NS_0^2. For the second case, cracks and pinholes transmit more light and therefore reduce the amplitude of EXAFS oscillations from

their ideal value, again affecting NS_0^2. Just as we expected, As has a larger NS_0^2 than Se suggesting that As is bonded to more neighbours than Se (since we expect S_0^2 to be roughly equivalent in each case). There is, however a large variation in NS_0^2 for As K-edge EXAFS and this suggests that there is a wide variation in possible bonding environments for As that are sensitive to the method of sample preparation. There is no clear trend in NS_0^2 for As based on As concentration. In one sense this is reassuring, since the similarity in spread of NS_0^2 for very small As concentrations (0.02% and 0.05%) to larger concentrations (6% and 10%) indicate that the measurements of low As concentrations are "good" (the signal-to-noise ratio obviously increases for higher concentrations of As). On the other hand, this suggests that perhaps sample inhomogeneity is a larger factor in the As bonding environment than the overall concentration. The data from As_2Se_3 can be used as a fingerprint of what As bonded to 3 Se, and Se bonded to 2 As looks like. Since the As K-edge NS_0^2 for the other materials is between that of the Se K-edge NS_0^2 and the As K-edge NS_0^2 for As_2Se_3, we can therefore conclude that the measurements show that As-dopants have between 2 and 3 nearest neighbours — which is more or less what was expected.

Figure 7.2 shows the comparison of NS_0^2 with σ^2 and the comparison of the bond length with the As concentration — the two possible comparisons not included in Figure 7.1. The first plot, NS_0^2 against σ^2 merely reveals the well-known correlation between σ^2 and NS_0^2. This is another reason why accurately determining the number of nearest neighbours with EXAFS is difficult [109]. The second plot, bond length against arsenic concentration, suggests that the Se-Se or Se-As bond length is independent of the As concentration — which again is more or less what was expected.

The fit values are summarized in Table 7.1. The results for each data set were averaged together according to measurement temperature, measurement edge, and state (amorphous or polycrystalline). The "anomalous" datasets indicated in Figure 7.1 were not included. Apart from a single poor fit (the As K-edge of pSe:2%As, measured at 30 K, with a $\mathcal{R}$-factor of 0.2) all the fits are quite good. These results suggest that the Se-Se bond length is slightly longer than the Se-As bondlength (the

Table 7.1: Summary of fitting parameters. The "K-Edge" column denotes the measurement edge (either Se or As K-edge) and includes the temperature and state of the material. Here "a" indicates an amorphous material and "p" indicates a polycrystalline (or annealed) material. The "sets" column indicates the number of datasets available for the given type of measurement. The $\mathcal{R}$-factor indicates the quality of the fit, values below $\sim$2% indicate statistically good fits. Note that both As_2Se_3 and tSe measurements were only taken at room temperature.

K-Edge	Sets	ΔE_0 [eV]	$r + \Delta r$ $\pm$ 0.01 [Å]	NS_0^2	σ^2 [$\times 10^{-3}$ Å^2]	$\mathcal{R}$-factor [%]
Se (30 K, a)	5	6.4 ± 0.5	2.29	2.0 ± 0.2	2.5 ± 0.7	1.2 ± 0.8
Se (30 K, p)	8	7 ± 1	2.28	1.7 ± 0.3	2.4 ± 0.4	1.9 ± 0.7
Se (300 K, a)	10	5.7 ± 0.2	2.30	2.1 ± 0.1	3.9 ± 0.1	0.67 ± 0.05
Se (300 K, p)	14	6.0 ± 0.8	2.30	1.8 ± 0.3	3.8 ± 0.2	0.9 ± 0.3
As (30 K, a)	3	5 ± 1	2.24	3.5 ± 0.7	2.6 ± 0.3	2 ± 1
As (30 K, p)	2	6 ± 2	2.22	2.4 ± 0.1	2 ± 1	10 ± 10
As (300 K, a)	10	6 ± 1	2.23	2.8 ± 0.3	2.7 ± 0.9	1.5 ± 0.5
As (300 K, p)	3	6 ± 1	2.22	2.7 ± 0.2	2 ± 1	2.1 ± 0.8
Se (As_2Se_3)	5	4.7 ± 0.5	2.25	2.19 ± 0.07	4.7 ± 0.1	1.6 ± 0.3
As (As_2Se_3)	3	5.9 ± 0.7	2.23	3.5 ± 0.1	5.8 ± 0.3	0.9 ± 0.1
Se (tSe)	4	6.6 ± 0.6	2.27	1.5 ± 0.1	3.8 ± 0.4	2.1 ± 0.5

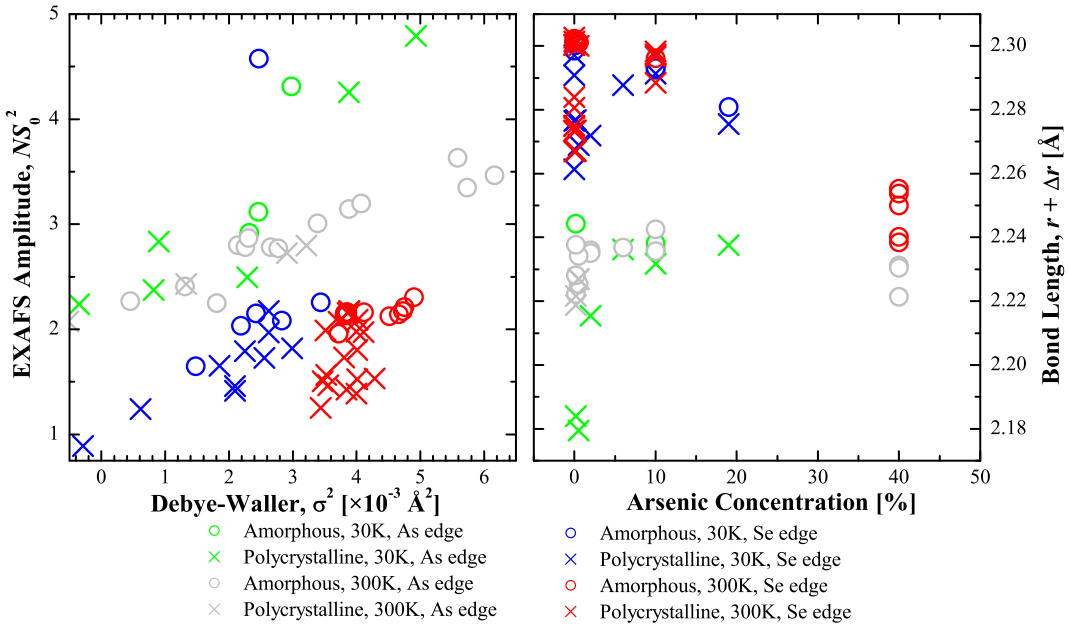

Figure 7.2: The fitting values for first shell fitting of all datasets. This Figure shows the two comparisons not included in Figure 7.1. This Figure follows the same conventions as Figure 7.1.

total average Se-Se[1] bond length is 2.29 ± 0.01 Å while the total average Se-As bond length is 2.24 ± 0.01 Å).

Table 7.1 illustrates a potential problem with the measurements. If S_0^2 is fairly consistent for all measurements (a reasonable assumption), then there is much more variability in coordination number (number of nearest neighbours, N) than previously reported. For example, it was previously reported that aSe had a coordination number of about ∼2.1, or roughly 5% higher than tSe. If we take our pSe measurements as the standard for 2 nearest neighbours, then aSe has about 17% more neighbours than pSe. Based on the statistics from the available data this is quite a

[1]Thus far *all* scattering neighbours of Se are assumed to also be Se, save in the case of As_2Se_3. Obviously with the inclusion of As dopants some of these bonds will be Se-As bonds. If indeed Se-As bonds are shorter than Se-Se bonds we therefore expect the average bond length as seen from the Se K-edge to be reduced as As concentration increases. This might be somewhat evident in Figure 7.2, but there is too much variability between samples of the same type of material and too few samples with distinct As concentrations (especially between 19% and 40% As) to make definite conclusions on this matter.

reasonable conclusion, since this conclusion is obtained from the independent fitting of 37 different samples and holds true at both room and low temperatures. If we take the tSe reference sample as the standard for 2 neighbours the situation is even worse (although recall from Chapter 6 problems with the tSe measurements make drawing quantitative conclusions from the spectra questionable). It is possible that pin-hole or cracks in the samples could cause an anomalous spread in NS_0^2, but given the breadth of these measurements it is questionable that *all* of them had the same problem. It is possible that the coordination of aSe is simply a lot more variable and sensitive to preparation method than previously thought.

The bond lengths reported here are a bit shorter than those found in literature (see Table 7.2). One possible explanation could be that the energy scale used in my spectra is incorrect. Since the radial distance is effectively the "frequency" of the $\chi(k)$ EXAFS oscillations, if what is measured as a 1 eV step is actually, for example, a 1.1 eV step, the apparent "frequency" of the $\chi(k)$ oscillations will be reduced producing a corresponding reduction in bond length. It is also possible that my results are *more* accurate than those reported in the literature, since the most recent result is from 2001. Beamlines for EXAFS and XRD have greatly improved since then, as have methods for fitting data. In any event, the discrepancy is less than 0.1 Å.

As an aside, I did try fitting the number of nearest arsenic and selenium neighbours. This was done by assuming that the Se in As_2Se_3 had exactly 2 As neighbours, the As in As_2S_3 had exactly 3 Se neighbours, and the Se in pSe had exactly 2 Se neighbours. From this assumption I calculated S_0^2 for the cases of Se-Se, Se-As, and As-Se scattering using the previously found values in Table 7.1. S_0^2 was then held constant for all datasets, as was the Se-Se and Se-As bondlengths (also found in Table 7.1). For the Se K-edge EXAFS measurements the Debye-Waller factor σ^2, the energy shift ΔE_0, and the number of Se and As neighbours N_{Se} and N_{As} were floated. For the As K-edge measurements the Debye-Waller factor σ^2, the energy shift ΔE_0, and the number of Se neighbours N were floated[2]. These fits showed

[2]Since As_2Se_3 has no As-As bonds, and since all other samples have even lower concentrations

Table 7.2: Summary of available bond lengths for various forms of pure Se. Under "method" RMC refers to a reverse Monte Carlo study on thermal relaxation data, and MD refers to a molecular dynamics calculation. Note that Takahashi conducted an X-ray photoemission spectroscopy (XPS) study and while his paper reported bond lengths, there was no explanation of how they were found or any reference to other works. Further note that Majid reported bond lengths for three different temperatures.

Author	tSe [Å]	mSe [Å]	aSe [Å]	Method
this work	2.27 ± 0.01	—	2.30 ± 0.01	EXAFS
Wyckoff [28]	2.32	2.34	—	XRD
Buchanan [20]	2.44	2.43	—	EXAFS
Bruning [38]	—	—	2.354 ± 0.002	RMC
Cherin [22, 111]	2.373 ± 0.005	2.336 ± 6	—	XRD
Hohl [112]	2.37 ± 0.02	2.34 ± 2	2.32 - 2.36	MD
Kaplow [37]	2.32	2.34	2.34	XRD
Kolobov [8]	2.36 ± 0.10	—	2.32 ± 0.01	EXAFS
Kolobov [113]	2.370	—	2.339 - 2.358	EXAFS
Majid [114] (26 K)	2.371	—	2.341	EXAFS
(80 K)	2.370	—	2.340	EXAFS
(300 K)	2.365	—	2.341	EXAFS
Takahashi [27]	2.36	2.34	—	XPS?
Zhao [115]	2.36 ± 0.01	—	2.32 ± 0.01	EXAFS

absolutely no consistent trend, and the $\mathcal{R}$-factors were generally worse than those of the normal first shell fits given in Table 7.1. This is not unexpected; since As has essentially the same X-ray scattering factors as Se and since the possible difference in bond length is only on the order of ∼0.06 Å. For two possible and almost identical models for the first scattering shell *any* combination of coordination numbers adding to the appropriate total (i.e. $\sum_i N_i \sim 2$) provide the same quality of fit — and this includes negative (and unphysical) coordination numbers.

7.2 Crystallization Effects: EXAFS

As previously mentioned, several amorphous films were annealed to induce crystallinity after an initial measurement (see Appendix A for details). Even with fully crystalline Se there is no observed long range order at room temperature in agreement with previous studies [107, 114], but at low temperature the long range order is clear.

The low temperature Se EXAFS for pure Se annealed at 60° C for 14 hours fits the theoretical tSe crystal quite well. This is expected, since it is known that tSe is the most stable phase of selenium [22, 34, 111, 116]. FEFF6L was used to generate the single and multiple scattering paths for an ideal tSe crystal. Of all the possible scattering paths, there were 9 which gave a statistically significant contribution to $\chi(R)$ at distances below 5 Å. These paths are shown in Figure 7.3, note that all Se sites in tSe are equivalent, so the same scattering paths can be constructed from any Se atom in the crystal. All but two of the paths are single scattering; that is they involve only the core atom and one scattering atom. Two paths are multiple scattering; these involve two additional scattering atoms along with the core atom. The shortest of these paths (path 4, marked in red in Figure 7.3) involves an electron scattering from the nearest neighbour to the third atom in the chain and then back to the core (or the reverse of this). The second multiple scattering path (path 7, marked in yellow in Figure 7.3) involves scattering to the nearest neighbour, back to

of As, it is reasonable to assume that there is no As-As clustering

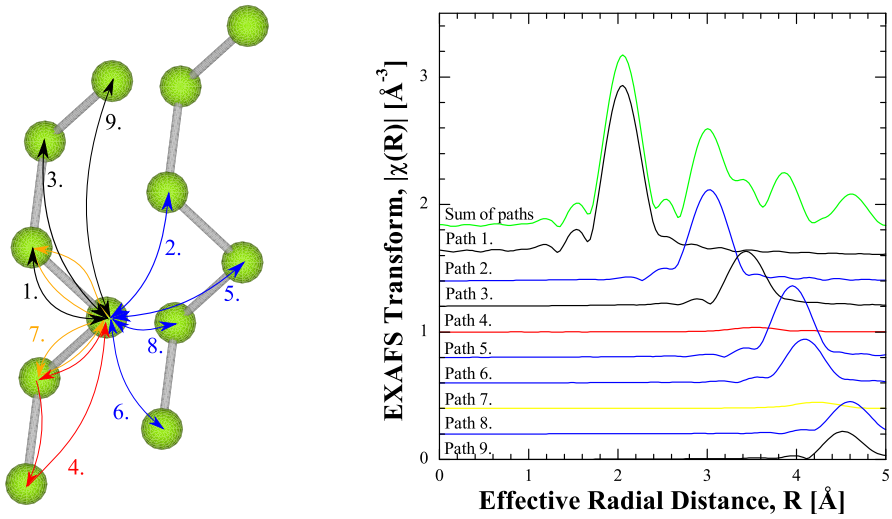

Figure 7.3: The 9 significant scattering paths in tSe. The left-most figure shows the physical scattering paths; black arrows are use to represent the paths along the same chain, blue arrows represent scattering paths between chains, and red and yellow arrows represent the two multiple scattering paths, respectively. The same colour scheme is used in the right-most figure, which shows the $|\chi(R)|$ contribution from each path to the total $|\chi(R)|$. The paths are numbered in ascending order by total distance travelled.

Table 7.3: The variables used for each scattering path. Each path had the same S_0^2 and ΔE_0 variable. Note that r_b is the ideal bond length, and θ_b is the ideal bond angle.

	Degeneracy	Debye-Waller	Path Length
Path 1	2	σ_1^2	Δr_1
Path 2	4	σ_2^2	Δr_2
Path 3	2	σ_1^2	$2\Delta r_1 \sin\left(\frac{\theta_b}{2}\right) + r_b \cos\left(\frac{\theta_b}{2}\right) \Delta\theta_b$
Path 4	4	$2\sigma_1^2$	$\Delta r_1 \sin\left(\frac{\theta_b}{2}\right) + \frac{r_b}{2} \cos\left(\frac{\theta_b}{2}\right) \Delta\theta_b + \Delta r_1$
Path 5	6	σ_2^2	Δr_3
Path 6	4	σ_2^2	Δr_4
Path 7	2	$2\sigma_1^2$	$2\Delta r_1$
Path 8	4	σ_2^2	Δr_5
Path 9	2	σ_1^2	Δr_6

the core atom, to the nearest neighbour on the opposite side, and then back to the core atom. The model for this structure used 11 variables, while the pSe data set had 22 independent data points. The S_0^2 and ΔE_0 variables were kept consistent for all paths, but the Debye-Waller factors and changes to the ideal path length were dependent on the path geometry. The expressions for these variables are given in Table 7.3 for each fitting path. Note that E_0 was increased by 8 eV to 12 666 eV, as suggested by the ΔE_0 in Table 7.1, to make the fitted ΔE_0 more precise.

The fitting model given in Table 7.3 is justified as follows. I assumed that there were two disorder parameters, one *intrachain* (denoted by σ_1^2), and one *interchain* (denoted by σ_2^2). Within a chain the atoms share strong covalent bonds with one another, while between the chains there are only van der Waals bonds. Therefore it is reasonable to guess that there is a different amount of disorder between the arrangements of chains than there is between the positions of atoms inside a single chain. Note also that scattering paths 4 and 7 experience roughly double the disorder that the other intrachain paths do, since they involve scattering off an additional

Table 7.4: Best fit parameters from fitting pSe data to the tSe structure. Recall that $E_0 = 12\,666$ eV. The errors listed are estimated by IFEFFIT from the statistics of the data.

	i = 1,	2,	3,	4,	5,	6
S_0^2	0.64 ± 0.09					
E_0 [eV]	0.6 ± 1.7					
σ_i^2 [$\times 10^{-3}$ Å^2]	1.1 ± 0.8	5 ± 1				
Δr_i [$\times 10^{-2}$ Å]	6.3 ± 0.7	-8 ± 2	1 ± 3	-4 ± 5	4 ± 3	-5 ± 3
$\Delta\theta_b$ [mrad]	6 ± 7					

atom. In a similar manner, the adjustments to path lengths Δr_i are chosen in a way to maximize the amount of structural information obtained. In particular Δr_1 indicates the change in bond length, and Δr_2 indicates change in the interchain distance. Since paths 3 and 4 involve scattering across a vertex in the chain, an expression involving adjustments to the bond angle θ_b as well as to the bond length r_b is used. The other paths (apart from path 7, which is simply double nearest-neighbour scattering) involve independent Δr_i. While it is possible to express these distances in terms of bond lengths, interchain distances, bond angles, dihedral angles [3], and other components, such expressions would be very complicated. Since the long-range paths become increasingly less significant with distance an accurate expression for the path is unlikely to improve the fit, or yield any additional physical insight.

The fitting was performed in R-space with a k-weight of 1 between the k range of 4.820 Å^{-1} to 14.097 Å^{-1} and the R range of 1.2 Å to 5.0 Å. The pSe data and the final fit are shown in Figure 7.4. The $\mathcal{R}$-factor was 0.034, which is pretty good, and certainly acceptable for our purposes of verifying that pSe does indeed have a tSe-like structure. The best-fit parameters are listed in Table 7.4.

There are a few things to note from Table 7.4. First, including longer scattering paths reduces the amplitude NS_0^2 for the first shell (note that I fixed $N = 2$ so $NS_0^2 =$

[3]The "dihedral" angle is the angle made between the planes of two adjacent bond angles.

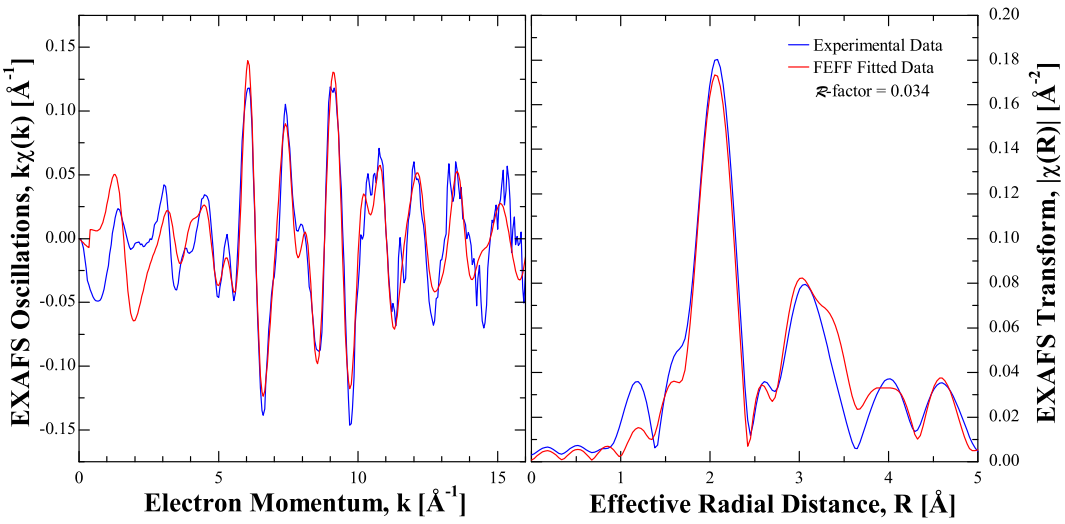

Figure 7.4: Comparison between pSe data and the best fit from tSe structure. Fitting was performed in R-space with a k-weight of 1. A k range of 2 to 15 was used for the $|\chi(R)|$ transform.

1.28, while Table 7.1 suggests $NS_0^2 = 1.8$ for this system). This is because the longer scattering paths still contribute slightly to the amplitude at low R. It is possible that the long range scattering in amorphous materials, while decoherent at longer wavelengths, might somehow add coherently to the first shell amplitude, increasing the apparent NS_0^2 obtained from first shell fitting. However without additional information this contribution is impossible to determine.

Secondly, fitting the entire crystal increases the bond length to ∼2.38 Å, which is closer to those previously reported (see Table 7.2) than the bond length obtained by first shell fitting (see Table 7.1). The fit suggests that the bond angle θ_b is essentially the "ideal" value, and that all other distances are within 0.1 Å of their ideal values. Finally, as we might expect, the interchain disorder indicated by σ_2^2 is greater than the intrachain disorder indicated by σ_1^2. In short these results show that aSe does indeed crystallize into a tSe-like form.

Long range order is present in the low temperature Se K-edge EXAFS of the annealed samples with 0.2%, 0.5%, and 2% arsenic concentration as well, as shown in Figure 7.5. Like pure Se, this order resembles the structure of trigonal Se. Even

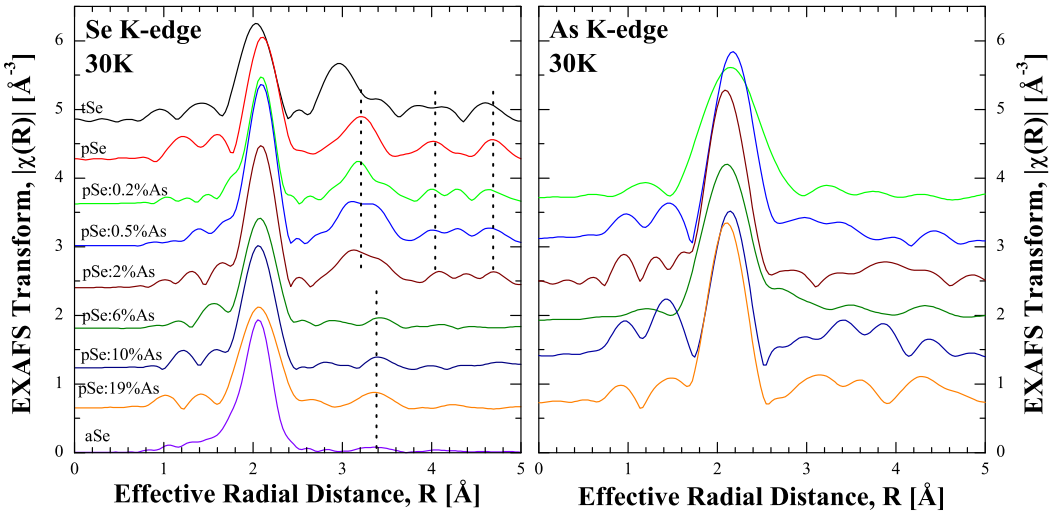

Figure 7.5: Low temperature Se and As K-edge $|\chi(R)|$ from k^2-weighted EXAFS. Note that crystalline order disappears for As concentrations greater than 2%. The Se K-edge k-range was from 2 to 14, 15, and 18 for tSe, pSe, and all others, respectively. The As K-edge k-range was from 2 to 10.8, 11.9, 12.6, 12.4, 13.1, and 11.0 for 0.2%, 0.5%, 2%, 6%, 10%, and 19% As, respectively.

after extensive annealing, no order is present in the Se K-edge EXAFS of samples with greater than 2% arsenic concentration. This clearly shows the suppressive effects arsenic has on the process of crystallization. Further, there is no long range order in any As K-edge EXAFS for any sample. Therefore even in the "mostly crystalline" Se:0.2%As sample the arsenic dopants do not have any preferred position in the selenium matrix. Note that, as previously mentioned, the As K-edge data is over a shorter range than the Se K-edge data. The low concentrations of As and the distortion at high k caused by the proximity to the Se K-edge make the As K-edge EXAFS data of much lower quality than the Se K-edge EXAFS, as shown in Figure 7.6. Still, the lack of long range order in *any* spectra is indicative that the environment local to As dopants is highly variable.

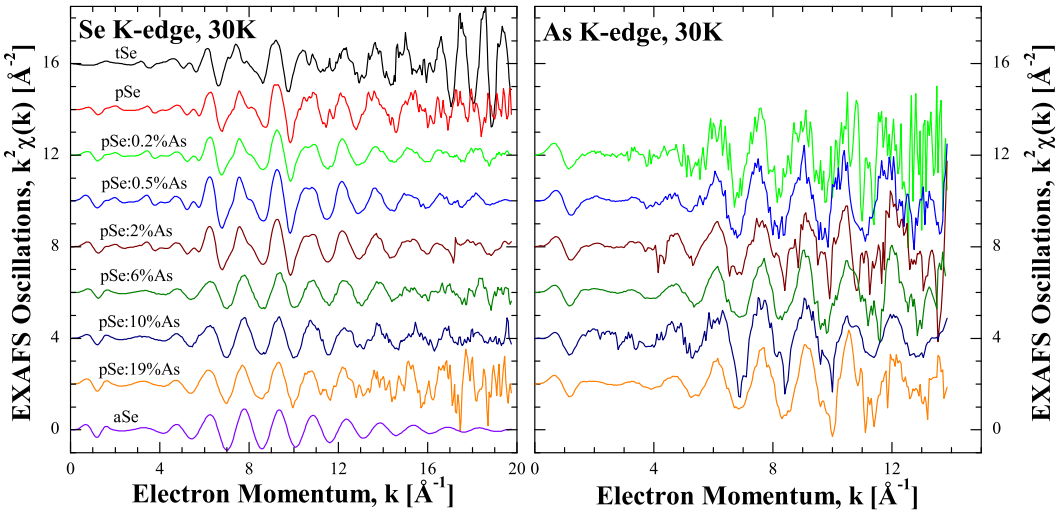

Figure 7.6: Low temperature Se and As K-edge $k^2\chi(k)$ EXAFS for pSe:x%As. Note the shorter range and greater noise in the As K-edge data. Note also the significant noise and high k artifacts in the tSe data, caused by sample inhomogeneity.

7.3 Crystallization Effects: XANES

Both the Se and As K-edge XANES are dominated by a characteristic white line[4] at the absorption edge near 12660 eV and 11868 eV, respectively. There is also a secondary feature above the Se and As K-edge at $\sim$ 12668 eV and 11876 eV, respectively. For the Se K-edge, both these features are common to the amorphous, trigonal, and monoclinic phase selenium [20]. As shown in Figure 7.7, there is a tertiary XANES feature in the Se K-edge which develops concurrently with annealing to a crystalline phase. This feature is present in annealed samples with long range order in the low-temperature Se K-edge EXAFS (namely Se, Se:0.2%As, Se:0.5%As, and Se:2%As) but the feature vanishes in samples without this long range order (namely the samples with greater than 2% arsenic concentrations). Unlike the EXAFS, however, the XANES feature is present independent of measurement temperature.

[4]The term "white line" dates back to the early days of using phosphor film to record X-ray spectra; intense features showed up as white lines on the film

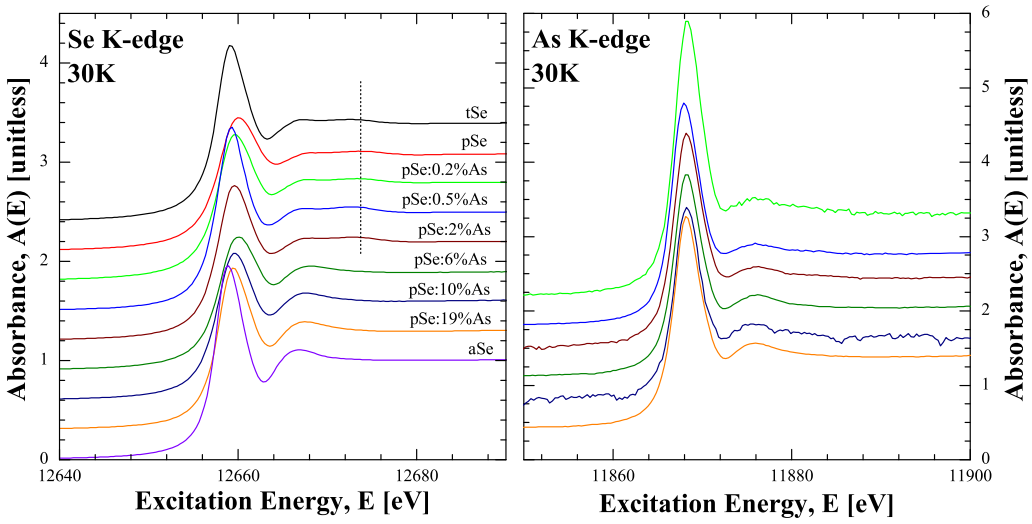

Figure 7.7: Low temperature Se and As K-edge $\mu(E)$ XANES for pSe:x%As. Note the weak tertiary figure indicated by the dotted line which occurs in samples with less than 6% As.

This tertiary feature in the Se K-edge XANES does not have an analogous feature in the As K-edge XANES, which is again commensurate with the As K-edge EXAFS showing no long-range structural order. Unlike long-range order in EXAFS, this tertiary feature in the Se K-edge XANES is present at room temperature as well as low temperature. To study this feature I measured the Se K-edge XANES of an aSe sample at room temperature, then annealed the aSe sample at 60° C for 3 hours and remeasured the Se K-edge. This procedure was repeated after annealing the same sample at 80° C and then 100° C for 3 hours each. As shown in Figure 7.8, these XANES measurements show the gradual development of this tertiary feature - which presumably is indicative of the crystallinity of the sample.

This tertiary feature has previously been reported for tSe, but not aSe or mSe [20], and the spectra I have measured agree with those in the literature. Note that while the measured mSe K-edge XANES in Figure 7.8 suffer from severe pin-hole effects which greatly suppress the intensities of the spectral features, they do not remove them entirely so the mSe spectra is useful as a qualitative guide. Since both my study of crystallization in aSe, and most of the literature suggest that the structure

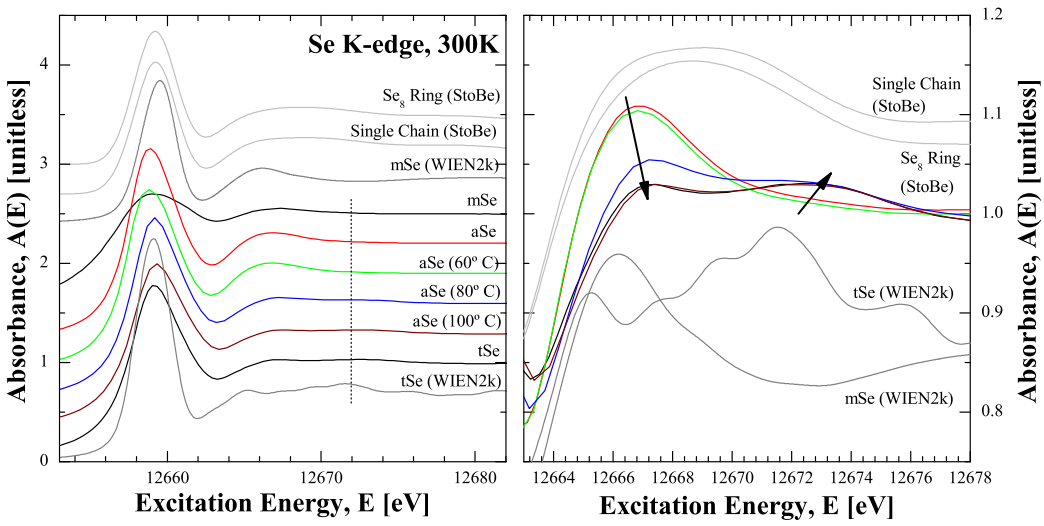

Figure 7.8: The effect of progressive annealing on the Se K-edge XANES of aSe at room temperature. Reference aSe, tSe, and mSe and several calculated XANES spectra are also shown. In the right-most plot, the arrows indicate the changes in spectral features with increasing annealing temperature.

of aSe is closer to that of tSe than mSe [36, 40, 117], the similarity between the XANES spectra of mSe and aSe should be regarded as a coincidence rather than an indication of structural similarity between aSe and mSe. This is the first time a study of the gradual development of this feature has been performed, and this is the first time evidence linking this feature to crystallinity, rather than allotrope (tSe-like or mSe-like) has been found. To further probe the relevance of this feature I calculated the Se K-edge XANES of tSe and mSe using WIEN2k. To probe the possible connection to partial crystallinity, I used StoBe to calculate the Se K-edge XANES of a lone Se_8 ring and lone Se_n helical chain, these spectra are also shown in Figure 7.8. The spectra calculated with WIEN2k agree quite well with the mSe and tSe measurements. Both StoBe calculations of partial crystal structures are essentially identical and indeed fall in between the extremes represented by the fully crystalline WIEN2k calculations. I therefore conclude that the magnitude of the tertiary feature in the Se K-edge may be used as a "fingerprint" of the crystalline order in aSe, even at room temperature.

7.4 Possible Pin-Hole Effects

It was previously mentioned that the spread in the NS_0^2 values obtained from first shell fitting was quite a bit larger than that reported in the literature, and pin-holes or cracks in the sample were a potential culprit. It has been established that inhomogeneous sample thickness can reduce the observed coordination number [118].

A large inhomogeneity in the sample thickness causes a local discontinuity in the absorbance of the incident beam. As described in Chapter 3, this causes the observed transmission intensity to be a summation of the weighted "real" transmission intensity with the incident X-ray intensity. Therefore the effect from pin-holes should be visible throughout the spectrum, not just in the EXAFS range. In particular, the intense white line in the Se K-edge XANES spectrum should be strongly effected by pin-holes. The white line height and the fitted first shell NS_0^2 parameter are shown in Figure 7.9, plotted against arsenic concentration and by individual measurement. There is no strong correlation between either the white line height or NS_0^2 and arsenic concentration. Further, while there is some correlation between NS_0^2 and white line height the trend is not consistent. For example, the scaled coordination number of room-temperature aSe is fairly constant, while the white line height shows considerably greater variation. However for room-temperature pSe the scaled coordination number shows greater variation than the white line height. These observations suggest that while pin-holes may be causing some problems with a few measurements, they are probably not responsible for all the NS_0^2 discrepancies.

Recall the expression for the effect of pin-holes, given by Equation 3.8 in Chapter 3. The pin-hole effect is given by the parameter α, and there is no reason why α cannot be a function of energy [119]. The EXAFS oscillations are different for surface atoms than bulk atoms and therefore in a sample with many micro pores and hairline cracks there might be a significant number of surface atoms making α a strong function of energy.

If the "true" absorbance $\mu(E)$ is somehow known, then it is possible to use equation 3.8 to calculate the pin-hole effect α. Of course it is very rare that the

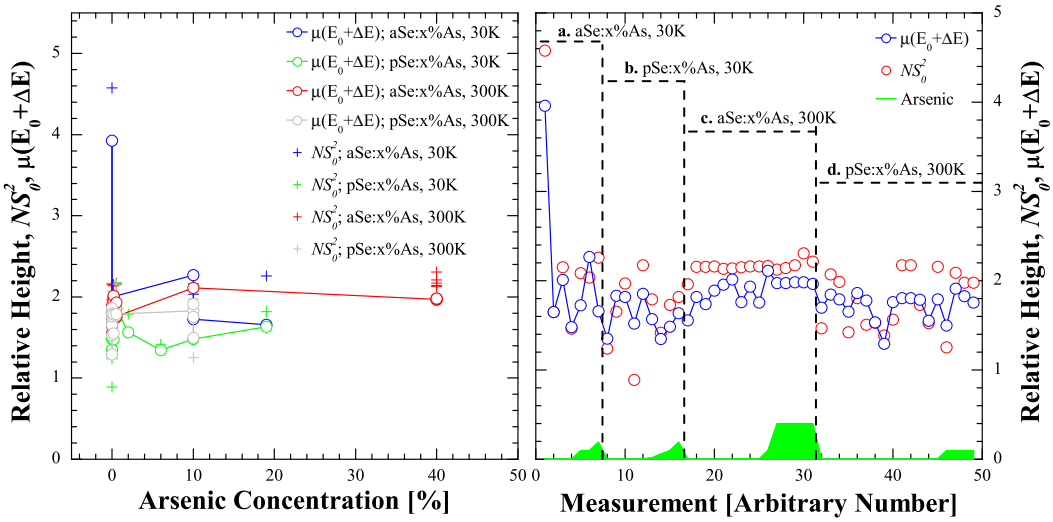

Figure 7.9: The scaled coordination number NS_0^2, and the white line height $\mu(E_0 + \Delta E)$ plotted against arsenic concentration and the individual measurement. For the white line height the spectra were normalized so that the post-edge absorbance was 1.0, while the pre-edge absorbance was 0. Note the arsenic concentration also given in the right hand panel as a fraction of total atoms.

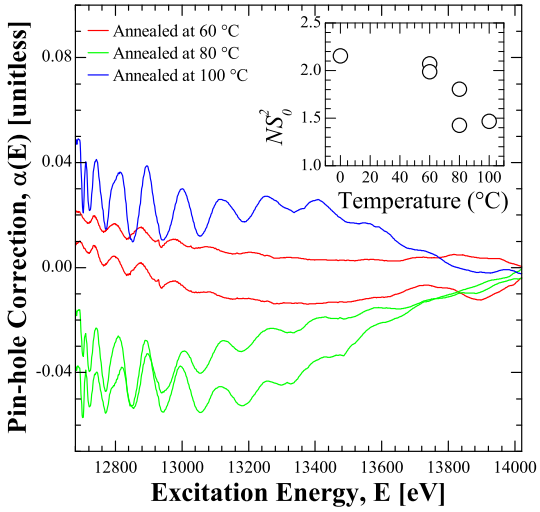

Figure 7.10: The pin-hole effect α(E) extracted using the initial aSe measurement as the "true" absorbance. The fitted scaled coordination numbers NS_0^2 from the first-shell fit of the normal EXAFS measurements are plotted in the inset for reference.

"true" absorbance is known, and therefore trying to correct for pin-holes is not good experimental practice. That being said, in the context of this experiment there is some value in attempting to calculate the pin-hole effect α simply to see what form it potentially takes.

This approach is best conducted with a series of measurements performed on an aSe film at room temperature, where the aSe film was gradually annealed at higher and higher temperatures (as described in the previous section). The measurements after annealing showed lower weighted coordination numbers NS_0^2 than found in the original amorphous film. It is possible that annealing is causing the creation of micro pores in the selenium film, but recall that EXAFS fitting on low temperature measurements of a separately annealed pSe film matched the theoretical standard for tSe. It is unlikely that one annealed film develops a substantial number of micro pores while another annealed film turns into a "good" crystal structure.

If the initial aSe film is taken as a measure of the "true" absorbance, the pin-hole effect α can be extracted from the Se K-edge XANES and EXAFS measurements of the same aSe film after progressive annealing. The pin-hole effect is shown in Figure 7.10, it is clearly a function of energy. Note that two separate films were annealed at 60° and 80° C, and the initial spectra from the amorphous films before annealing were essentially identical. This similarity in initial results, the fact that at room temperature even tSe shows no long-range EXAFS order, and the fact that we expect the coordination number to change by only about $\sim 5\%$ provide a reasonable justification for using aSe as the "true" absorbance - if indeed the differences between the spectra are due only to thickness inhomogeneities.

As shown in Figure 7.10, there is no trend in α(E) for different annealing temperatures, although the measurements with the same annealing temperature are fairly consistent. Secondly, the deviations of α(E) from the pin-hole-free case are not consistent with the spread in NS_0^2. Since the influence from a pin-hole should reduce the white line height and the scaled coordination number in tandem [118], this is further evidence that pin-holes alone cannot account for all the discrepancies between the calculated NS_0^2 and those present in the literature.

Chapter 8

Electronic Structure of Selenium

While the electronic information obtained from XES and XANES spectra of aSe, tSe, and mSe does not have any direct connection to the physical structure of these materials, the electronic structure is the key factor in determining many physical properties. Since I had ample opportunity to take high-resolution soft X-ray spectroscopy measurements of these materials, it is worthwhile to examine the basic electronic structure of these materials. The following sections briefly describe the results of this study.

8.1 Historical Approaches

The electronic structure of aSe was initially studied to determine electron and hole mobilities and the position of charge traps in the bandgap [2]. In the early 1970s Kramer calculated the electronic structure of selenium with various degrees of disorder using an atomic pseudopotential method (not a self-consistent method however; Kramer's model was based on measured data from reference standards) [5]. Kramer's calculation suggested a triplet feature below the primary band in the valence level, which was not observed in a ultra-violet photoemission (UPS) study by Nielsen [120] (in an interesting twist Nielsen actually managed to publish *before* Kramer, although his work is based on Kramer's study). Immediately thereafter Shevchik *et al.* measured the valence band of aSe with UPS, and found better agreement with Kramer's model, and concluded that the discrepancies with theory were due to a poor choice of structural model by Kramer [121]. Shevchick followed his experimental study with a theory that aSe was formed of helical chains, but the disorder was due to a reduction

in the average dihedral angle rather than an increase in interchain separation [122]. In contrast to Shevchik's findings, Laude, Kramer and Maschke performed UPS studies of aSe and made the radical conclusion that aSe was *six*-fold coordinated with a bondlength of 3.1 Å [6] — a conclusion that has since been totally refuted by subsequent EXAFS studies (see Chapter 7).

In the early 1980s Takahashi performed several UPS and XPS studies of aSe [27,39,123,124]. The first of these involved aSe deposited in vacuum on cold substrate (77 K), and the spectra appeared to show greater disorder than the aforementioned studies where aSe was deposited at room temperature [39]. In the subsequent papers Takahashi noted valence structures related to what he identified as "lone pair" and bonding *4p*-states [123]. He further identified features in the bonding *4p*-states ∼5 eV below the Fermi level and the *4s*-states ∼12 eV below the Fermi that were unique to the amorphous, trigonal, monoclinic phases [124], and rhombohedral [27] phases.

While technically all Se K-edge XANES studies are related to the conduction band electronic structure (although distorted by the core-hole effect), the available resolution at the K-edge is not sufficient to identify any detailed electronic structure. However due to the rather odd binding energies of selenium (and arsenic, for that matter) there was only one study on the $M_{4,5}$-edge XANES [106]. This study merely identified the $M_{4,5}$ splitting, no other analysis of the spectrum was conducted. Further the signal-to-noise ratio of the data was very poor. Finally, to my knowledge, there is no literature available on the $M_{4,5}$-edge XES.

8.2 The *4p*-states of Selenium

The Se $M_{4,5}$-edge XES was measured at BL8, and the Se $M_{4,5}$-edge XANES was measured at the PGM, as described in Chapter 6. The Se $M_{4,5}$-edge XES do not show very much fine detail, even in the case of tSe although the predicted partial DOS does have some prominent fine structure [5]. This is not unexpected, however, since the extremely short lifetime of the core-hole adds considerable broadening to the XES measurements. The lifetime broadening is also the reason why the M_4 and M_5 edges

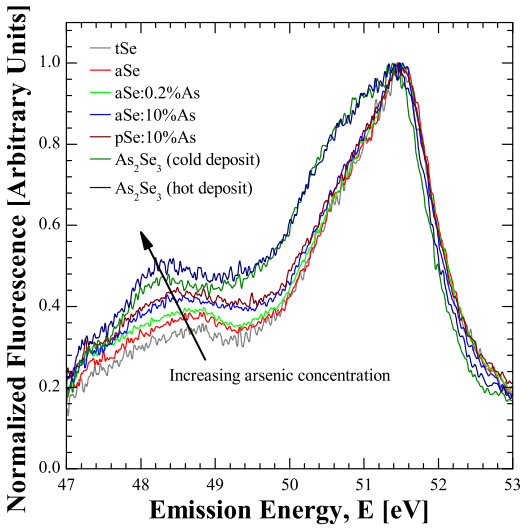

Figure 8.1: The Se $M_{4,5}$-edge XES for several samples. The primary and secondary emission bands at 51.5 and 48.5 eV, respectively, have the same separation as the "lone pair" and bonding *4p*-states observed by Takahashi. Note that the energy calibration was estimated from the elastic scattering of 3rd order light, but the calibration could still easily be off by as much as 1 eV.

are not resolved, they should be less than 1 eV apart [100]. As shown in Figure 8.1, there does appear to be a small trend in the secondary emission band at 48.5 which is commensurate with increasing arsenic concentration and/or increasing disorder. The spacing between the secondary emission band and the primary emission band is equivalent to the spacing between the "lone pair" and bonding *4p*-states identified by Takahashi [123]. (Note: the "lone pair" is the two *4p* electrons which do not participate in chemical bonding.) The increased width in the main emission band of As_2Se_3 casts some doubt on whether the feature is really due to a lone pair. If it is, then Se bonded to As has a significant effect on the lone pair.

Since the Se $M_{4,5}$ edge was already at the extreme low end of BL8's range the As $M_{4,5}$-edge XES could not be measured. The $M_{4,5}$-edge XANES could be measured for both edges, however, at the VLS-PGM beamline. Like the K-edge XANES, the As and Se $M_{4,5}$ edges are quite similar in shape, which is somewhat expected since both measurements probe roughly the same *4p*-states. The fact that the K- and

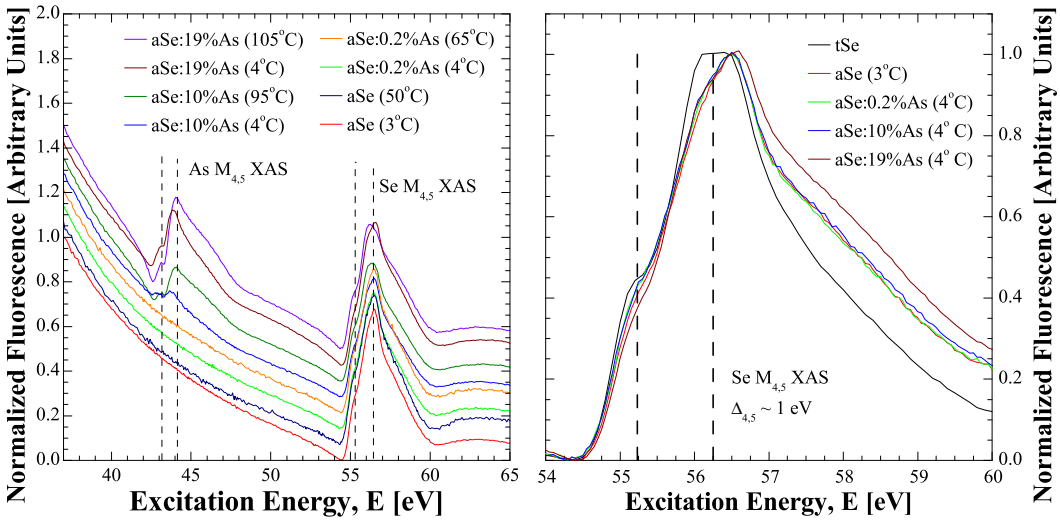

Figure 8.2: The As and Se $M_{4,5}$-edge XANES for several samples. Note the significant Gaussian-like background in the spectra. The temperature of the substrate is indicated.

$M_{4,5}$-edge XANES are so similar suggests that the core-hole effect may not distort the conduction band states very much, since a core-hole in the semi-valent *3d*-states should have less of an effect than a core-hole in the *1s*-states. The $M_{4,5}$-edge XANES taken at the VLS-PGM for a variety of aSe:x%As alloys is shown in Figure 8.2. Note that there is a significant non-linear background to the measurements. Like the $M_{4,5}$-edge XES, the $M_{4,5}$-edge XANES of tSe does not show very much fine structure. The tSe spectrum is consistent with those measured by Givens [106].

The tSe DOS calculated with WIEN2k [80] using the Perdew-Burke-Ernzerhoff GGA functional [91] is fairly consistent with Kramer's early calculations for both aSe and tSe, although my calculations show a doublet rather than triplet feature in the band from -3 to -6 eV [5]. From the WIEN2k calculations, the M_5 XES and XANES spectra were calculated by multiplying the matrix of the allowed dipole transitions, a radial transition probability, and the *4p* DOS [94] (for the XANES spectra an M_5 core-hole was introduced and an extra valence electron was added). The calculated spectra were broadened by a Gaussian function with a width of 0.33 eV, and a Lorentzian function with a width of 0.25 eV for XANES (just core-level lifetime

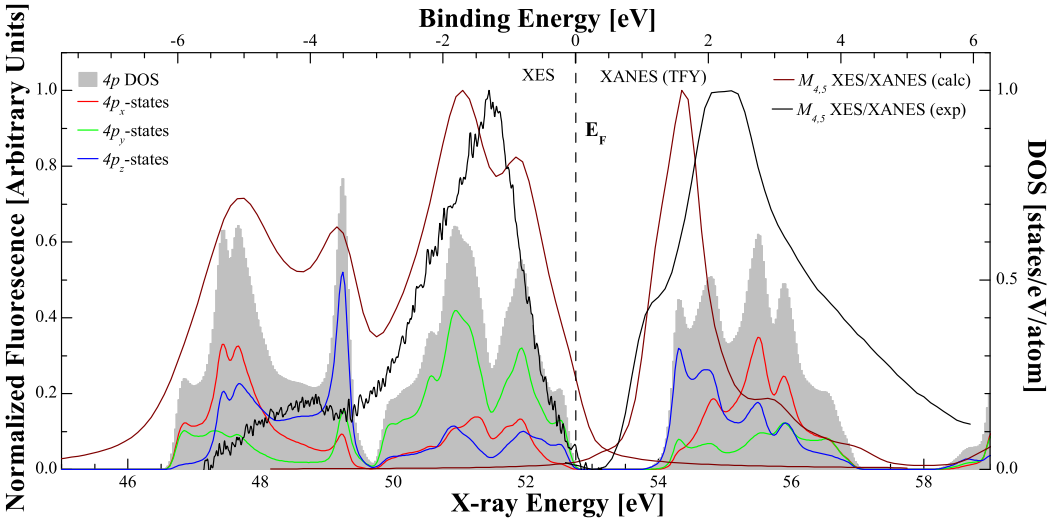

Figure 8.3: Calculated *4p* DOS and calculated and measured $M_{4,5}$-edge XES and XANES for tSe. For the symmetry-dependent *4p* states the z-axis is along the helical chain. Recall there are six chains, at the vertices of a regular hexagon, surrounding a central chain. From this perspective the x-axis is directed through the edge of the hexagon (i.e. between two chains), and the y-axis is directed towards a vertex (i.e. at one of the chains). Recall that the energy alignment of the measured $M_{4,5}$-edge XES and XANES may not be completely accurate, and therefore the $M_{4,5}$-edge XANES has been shifted to slightly lower energies to match the calculation.

broadening) or 0.55 eV for XES (an additional 0.30 eV valence lifetime broadening) to roughly match the experimental resolution.

As shown in Figure 8.3, the calculated spectra agree qualitatively with the measured spectra. However, note that it is clear that the life-time broadening is at least comparable to that applied to the calculations, and the calculated spectra show considerably more fine structure than the measurements. For example if the calculation is accurate then the primary emission band at 51.5 eV should at least show the double feature evident in the calculated emission band. Further the calculated XANES spectrum does not match the measured XANES spectrum very well, although this could be due to choosing a fairly small supercell (only $2 \times 2 \times 2$ unit cells). Note that the unoccupied DOS in Figure 8.3 is the true unoccupied DOS without the core-hole distortion (although the calculated XANES did include the effect of the

core-hole). One possible explanation for the discrepancies between measured and calculated spectra could be due to poor local symmetry in actual tSe. Note that, for example, in the valence band a particular symmetry of *4p* states are the main component of each sharp feature — the first two are from $4p_y$-states, the third is from $4p_z$-states, and the fourth is from $4p_x$-states. Since even tSe is a "poor" crystal — it has a considerable amount of internal degrees of freedom, and therefore lattice periodicity can easily be destroyed — it is possible that individual Se sites have enough local structural variation to break the symmetry enough to smear out all of these distinct features in the ideal structure. It is worthwhile to note that low temperature (∼30 K) $M_{4,5}$-edge XES measurements were performed on tSe (and various aSe:x%As alloys), and no additional fine structure was observed. This suggests that DFT calculations on structures with periodic boundary conditions may not be the best approach to study selenium-arsenic alloys.

Chapter 9

Structural Distortions

The room temperature and low temperature EXAFS leave no doubt that there is no consistent long range structure in aSe. Further, as previously mentioned, past studies on aSe suggest that the structure of aSe is related to the structure of tSe, or a combination of tSe and mSe. The following sections illustrate different attempts at incorporating structural disorder into the form of tSe to reproduce the observed aSe spectra.

9.1 Trigonal Crystal Structure

As previously mentioned, trigonal selenium is the most stable allotrope of selenium at ambient conditions. The structure of tSe consists of a six-fold arrangement of helical chains. In the ideal crystal structure each selenium atom is bonded to two neighbours, the bond length is constant for all atoms, and the angle between the two bonds is constant. Finally the dihedral angle - the angle between the planes of two adjacent bond angles - is constant. The structure of a single helical chain in tSe is shown in Figure 9.1. For the purposes of the following discussion I will use the crystallographic values found by Wyckoff [28], where the bond length, b, is 2.32409 Å, the bond angle, θ, is 104.8263°, and the dihedral angle, ϕ, is 101.756°. These values are excessively precise, and the accuracy might be off by as much as 5% (for example, refer back to Table 7.2 for a comparison of various bond lengths found in literature). However since the crystal structure has the same symmetry for any consistent choice of the above values, and since each value will be varied and/or fitted, the starting point is somewhat arbitrary. Since Wyckoff provides the most

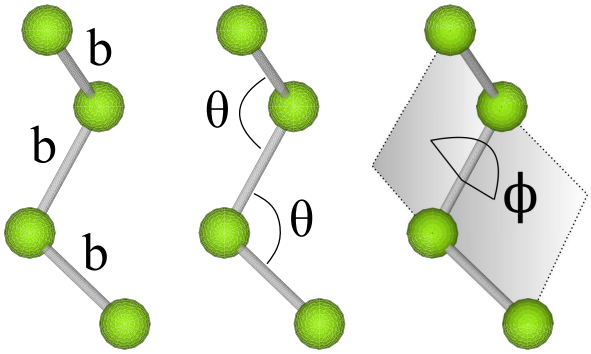

Figure 9.1: Three short helical chains of tSe. The bond length b, bond angle θ, and dihedral angle ϕ are indicated.

extensive study of the crystallography of tSe, I have chosen his values to start with.

Introducing disorder into the tSe structure can be achieved by changing the orientation and alignment of the helical chains, or by changing the arrangement of atoms within a chain.

9.2 Thermal Disorder

The EXAFS spectra of tSe do not have any long range order at room temperature, although this order becomes apparent at low temperatures. This suggests that tSe has significant thermal disorder. It is reasonable to expect that this thermal disorder can manifest as a random variation in atomic position (a "microstate" disorder), or as a random distortion in the arrangement of chains (a "macrostate" disorder). The time scale of EXAFS is much faster than the actual thermal vibration of atoms [125], so each EXAFS spectrum represents an average "snap shot" of the atomic positions. In this context the "macrostate" disorder can be modeled by adjusting the long-range structure. The "microstate" disorder can be modeled by either adding random displacements to atomic positions, or by examining the fitted Debye-Waller factor σ^2 since the Debye-Waller factor represents the mean squared relative displacement of the scattering atoms with respect to their ideal positions [56].

While the Debye-Waller factor σ^2 is often simply a fitted value, it can be calcu-

lated from a model of phonon modes in matter. In particular, FEFF6L is designed to calculate Debye-Waller factors using either a correlated Einstein model, or a correlated Debye model [126]. In the former case, the Debye-Waller factor is estimated using the expression in Equation 9.1, where Θ_E is the "Einstein temperature", m is the atomic mass, and T is the temperature. In the latter case the Debye-Waller factor is estimated using the expression in Equation 9.2, where Θ_D is the "Debye temperature" and ρ is the density of the material.

$$\sigma_E^2 = \frac{\hbar}{m\omega_E} \coth\left(\frac{h\omega_E}{2k_BT}\right) \tag{9.1}$$
$$\omega_E = \frac{k_B}{\hbar}\Theta_E$$
$$\sigma_D^2 = \frac{\hbar}{m}\int_0^{\omega_D} d\omega \frac{3\omega}{\omega_D}\left(1 - \frac{\omega_D}{\omega R k_D}\sin\left(\frac{\omega R k_D}{\omega_D}\right)\right)\coth\left(\frac{h\omega}{2k_BT}\right) \tag{9.2}$$
$$\omega_D = \frac{k_B}{\hbar}\Theta_D$$
$$k_D = \left(6\pi^2\rho\right)^{\frac{1}{3}}$$

If the thermal disorder in room-temperature tSe is responsible for the lack of long-range order in the EXAFS spectra, then the model used in Chapter 7 to fit the structure of pSe should be applicable for room temperature pSe with an increased σ^2 parameter. With this in mind, I used the scattering paths defined for the fit in Chapter 7 to fit the data for room temperature and low temperature pSe simultaneously. In this slightly revised fitting model the structural parameters (bond lengths, bond angles, etc.) were forced to be consistent in both fits and the Debye-Waller factor σ^2 had a thermal component based on the measurement temperature (300 K or 30 K, as appropriate) and a fitted Θ_x (where $x = E$ for the Einstein model and $x = D$ for the Debye model, as appropriate). The energy correction E_0 and EXAFS amplitude S_0^2 were freely floated for both datasets.

The fit of room temperature and low temperature pSe to the Einstein and Debye models of thermal disorder are shown in Figure 9.2. Neither of the two methods of calculating thermal disorder produce a very good fit; the Einstein fit has an $\mathcal{R}$-factor of 0.15, and the Debye fit has an $\mathcal{R}$-factor of 0.13. The fitted Einstein temperature

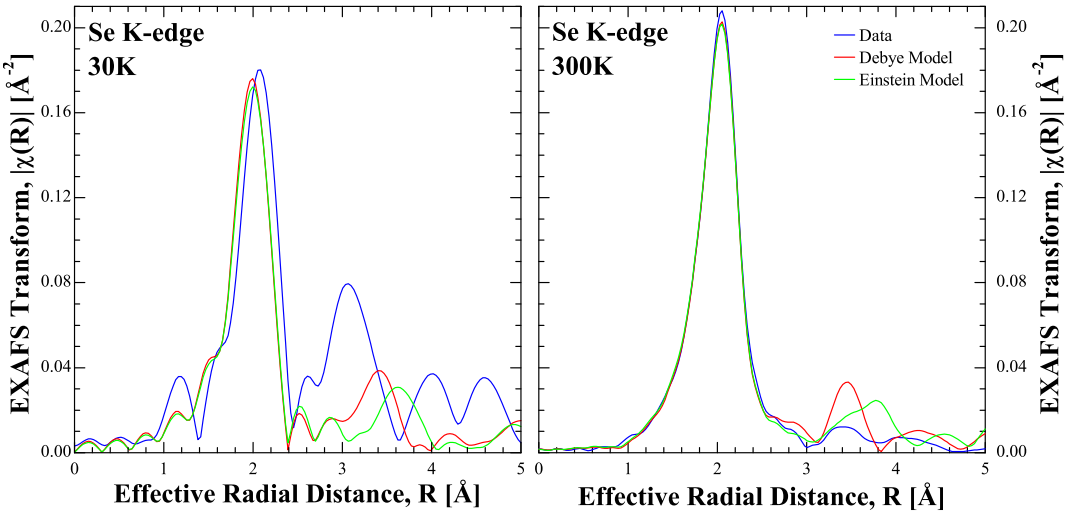

Figure 9.2: Low temperature and room temperature pSe measurements simultaneously fitted to the structure of tSe using the Einstein and Debye models for thermal disorder.

is $\Theta_E = 303 \pm 13$ K, and the fitted Debye temperature is $\Theta_D = 366 \pm 14$ K. Since tSe is monoatomic and our measurements go down to fairly low temperatures, we expect the Debye model to provide the best results [127], and judging by the $\mathcal{R}$-factors this is the case - albeit by a narrow margin. The Debye temperature for tSe is estimated as ~ 150 K from heat capacity and elastic constants [128], however calculations from heat capacity measurements suggest that the Debye temperature for intrachain phonon modes is ~ 350 K, while the Debye temperature for interchain phonon modes is ~ 140 K [128]. In this regard my calculation is consistent with the intrachain Debye temperature.

It is still apparent, however, that since neither the Debye nor Einstein models provide a good fit to the experimental data, the disorder present in room temperature tSe cannot be accounted for by a simple application of harmonic thermal disorder. In a sense this is to be expected, the structure of tSe is not conducive to spherically symmetric atomic distortions, and thermal variations in the relative positions of neighbouring chains are probably much greater than thermal variations in the relative position of neighbouring atoms.

9.3 Regular Disorder

It seems reasonable to assume that at room temperature the chain-like structure of tSe is still present. The helical chains in tSe are, after all, quasi-molecular with fairly strong covalent bonds so it is doubtful that the transition from room temperature to 30 K is sufficient to significantly modify the positions of atoms within a chain. The arrangement of the chains, however, is probably subject to considerably greater variation.

With the above argument in mind, I used FEFF6L to calculate the EXAFS from a variety of distorted tSe clusters. I assumed that the chains were approximately straight on a 12 Å scale. The central chain, with the absorbing atom, was fixed and the position of the six surrounding chains was randomly varied. These variations included rotations of up to 180° around the crystal *c*-axis, rotations of up to 5° around the crystal *a*- and *b*-axes (centered at the level of the absorbing atom), and displacements of up to 50% of the unit cell length along the *c*-axis and 10% of the unit cell length along the *a*- and *b*-axes. The EXAFS from 1000 of these random structures were calculated and averaged together to approximate the environment throughout the material.

The averaged calculated EXAFS suggests that the interchain order is very easily washed out by random displacements. Indeed, Figure 9.3 suggests that any combination of two or more types of interchain distortion essentially removes all interchain order. The only remaining order is within the central chain, indicated as the second, third, and fourth nearest neighbours along the chain. Further, note that even though the fitted Debye temperature matches that of the calculated intrachain vibrational modes, the intrachain features at ∼3.3 Å and ∼4.8 Å in disordered EXAFS in Figure 9.3 are still present in the fitted thermal disorder EXAFS of Figure 9.2. This suggests that either the intrachain distortion is anisotropic, the calculated Debye temperature for intrachain modes is incorrect, or even in tSe the chains become twisted and bent at room temperature - implying significant relaxations in atomic positions after cooling to 30 K. Of these three possible causes the first case seems the most likely, and

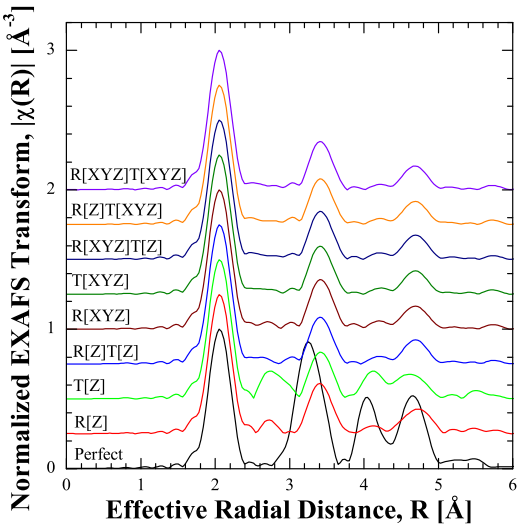

Figure 9.3: Average calculated EXAFS for 1000 random structural models for different types of disorder. The label R[] denotes that neighbouring chains were randomly rotationed around the specified axes and the label T[] denotes that neighbouring chains were randomly translated along the specified axes. The undistorted calculated tSe structure is indicated in black at the bottom.

additional calculations investigating this possibility will be performed in the future.

9.4 Irregular Disorder

The ideal bond lengths, bond angles, and dihedral angles in a selenium chain are determined by the atomic properties of selenium. Obviously these quantities can deviate from their ideal 0 K equilibrium values due to finite temperatures and external stresses, however these deviations should be minimal. Indeed, all the experimental data both in this research and in the literature support the conclusion that the Se—Se bond length at room temperature is within 5% of the ideal bond length at most, and the fit of pSe to the structure of tSe conducted in Chapter 7 suggests that the bond angle is very close to the ideal value. There is one degree of freedom in constructing a selenium chain, though; the sign of the dihedral angle. As shown in Figure 9.1, it takes 4 atoms to define the dihedral angle. The fifth atom added to this chain will define a second dihedral angle using the 3 most adjacent existing atoms.

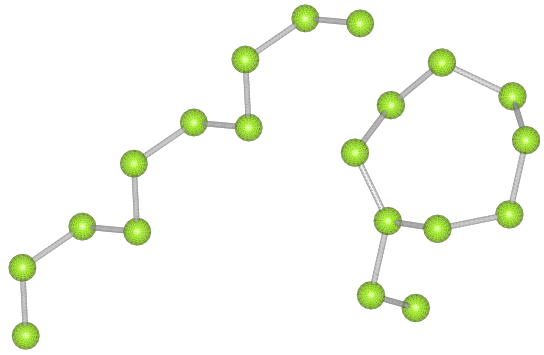

Figure 9.4: The difference between constant and alternating dihedral angles. Each structure is formed from 10 Se atoms, the bond lengths, bond angles, and magnitude of the dihedral angles are the same in each. The chain on the left has a constant dihedral angle sign, the ring on the right has an alternating dihedral angle sign after the first two dihedral angles (the initial atoms form the "stem" at the bottom).

If adjacent dihedral angles have the same sign relative to each other the chain will form the conventional helical shape found in tSe. If adjacent dihedral angles have opposite signs relative to each other the chain will approximately form an 8-element ring, similar to the structure found in mSe. These structures are shown in Figure 9.4.

Since past studies have suggested that aSe has something in common structurally with tSe and mSe (see, for example, References [6, 37]), and since the ring structure of mSe can be approximated by an 8-element chain with alternating dihedral angles, a common model for the structure of aSe is a collection of tangled chains where the sign of the dihedral angle is random [29], as shown in Figure 9.5. A sufficient density of these tangled chains would then hopefully reproduce the low temperature EXAFS data for aSe.

To test this model for the structure of aSe I implemented the following model: generate a random chain, and choose the 6th atom as the absorbing atom for EXAFS. Continue to generate this chain until it extends 10 Å beyond the absorbing atom. These numbers are somewhat arbitrary, since I only calculate the EXAFS to a radial distance of 6 Å, I simply wanted to make sure that the starting and ending points

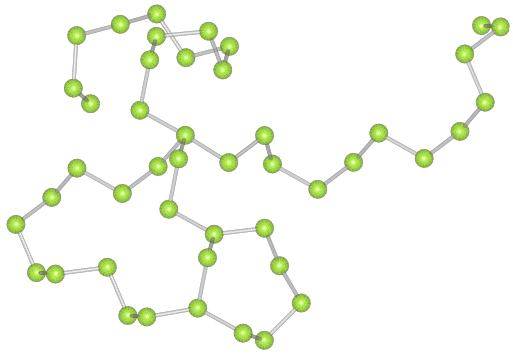

Figure 9.5: A tangled chain created by randomly choosing the relative sign of the dihedral angle. "Defect sites" can be formed in places where the chain loops back on itself, in this case there is a 4-coordinate Se "defect" site roughly in the centre of the chain. At this site only two of the bond angles are close to the ideal value.

of the chains were outside the region of interest. Once the initial chain is created then start generating chains from random points on a 20 × 20 × 20 Å cube with the absorbing atom at the centre. These chains are "grown" inwards until they exit the cube, or until they collide with an existing chain. A "collision" is defined as trying to place an atom closer than 90% of the ideal bond length to another atom. If an atom collides with an existing chain, the position with the alternate dihedral angle sign is tested for placement. If that position also fails, the chain is terminated at that point and a new chain is started. This process is ideally repeated until the appropriate density is reached. See Appendices C for more detail. A sample cluster is shown in Figure 9.6.

To model the spectra of aSe I averaged the calculated EXAFS from several hundred of these random chain structures together. The average EXAFS from four different runs are very consistent, suggesting that a few hundred iterations is sufficient to average out the disorder in the clusters. The width of the of average EXAFS features are quite similar to that of the measured aSe features, suggesting the disorder in the calculated EXAFS is quite similar to the thermal distortions in room-temperature aSe EXAFS. As shown in Figure 9.7, the calculated EXAFS still reveals some long range structure similar to that found in the thermal disordered

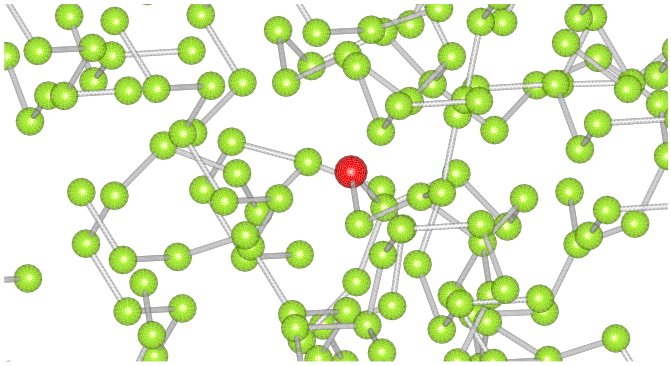

Figure 9.6: A sample cluster of Se atoms, modeling the aSe structure. The scattering atom is shown in the centre, in red.

calculations in Figure 9.2 and the regular chain disorder in Figure 9.3. This long range structure is again due to intrachain scattering. This is a bit surprising, since otherwise these calculations compare very favourably with the measured data: the height of the first EXAFS peak is very close to the measured data, suggesting that the average coordination number and the bond length used are very close to the actual values in aSe. Further, the position of the second EXAFS peak at ∼3.3 Å is quite close (although of much greater amplitude) to the peak in the experimental data, suggesting that the bond angle used in the calculation is very close to the actual value. Finally, both secondary features have similar widths, suggesting that there is not a large variation in the bond angles.

There are a few problems with this model for aSe. For one thing, the density of these clusters is quite low. The average cluster density is ∼3.2 g/cm^3, while the actual density of aSe is ∼4.3 g/cm^3 [29]. Since the packing fraction in the calculated clusters is not high enough, it is quite possible that there are not enough interchain neighbours to smooth out the regular presence of the third and fourth intrachain neighbour, respectively. The second problem is that defect sites are not handled very well. The only constraint on atom placement is proximity to atoms in other chains, not on the bond angle that would be created after placing the atom within the bond distance of that other chain. Since aSe is a relatively soft material, it is unlikely that the extra bonds on 3- or 4-coordinate selenium would occur at an arbitrary

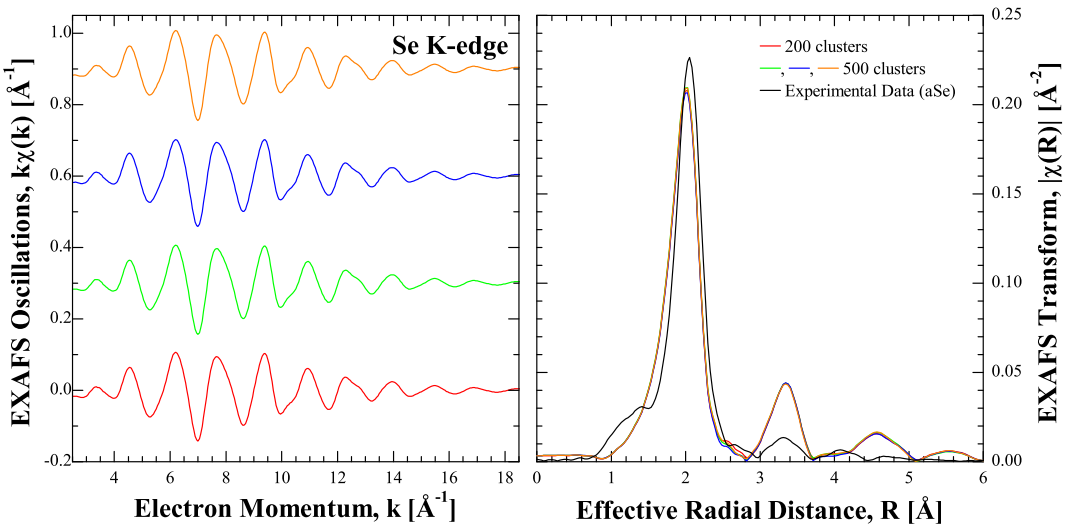

Figure 9.7: The average EXAFS from several hundred cluster calculations compared to experimental room-temperature aSe EXAFS.

angle. Further, calculations suggest that the lowest energy defective site is a pair of single coordinated Se^{-} and triple coordinated Se^{+} atoms in close proximity [29]. While both single and triple coordinated Se sites are possible in my model, there is no mechanism to encourage them to occur close to one another. Finally, apart from random chance there is no mechanism to discourage 4- or higher coordinate selenium sites. Chemically a 4-coordinate selenium site would require a rather bizarre charge distribution, and 5- or 6-coordinate sites are even worse. In my calculations 11.2% of the sites were single-coordinate, 70.9% of the sites were 2-coordinate, 16.0% of the sites were 3-coordinate, and 1.8% of the sites were 4-coordinate. Out of the 1700 structures there were a handful of 5-coordinate sites ($\sim$ 0.13% of the sites), and a single structure had a 6-coordinate site.

The first problem might be caused by the rectilinear nature of creating new chains. When a new chain is created outside the boundary it can only growing along one of the Cartesian axes. Although the chain will eventually bend away from this axis, it may still be difficult to create the right chain to fill a void near the centre of the cluster. A model where chains can start growing along arbitrary directions is currently

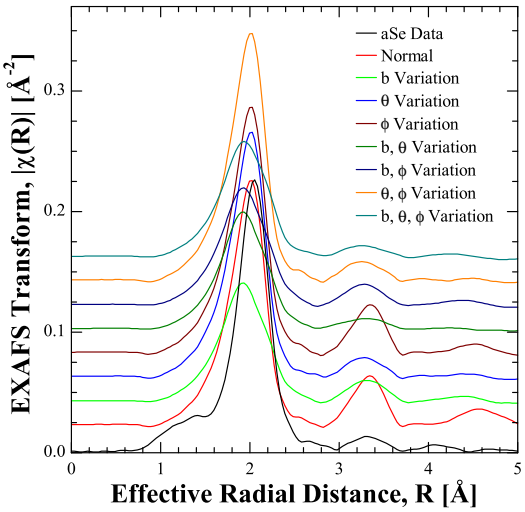

Figure 9.8: The average EXAFS from 500 hundred cluster calculations where the bond length, b, bond angle θ, and dihedral angle ϕ are randomly altered. Experimental room-temperature aSe EXAFS data is included for comparison.

under development. The second problem is more difficult to solve; it might require weighting the atomic placement by some sort of pseudopotential created by existing atoms and approximate charge densities. To incorporate those considerations an entirely different approach might be appropriate, and more study is needed.

The twisted chain model can also incorporate random variations in bond length, bond angle, and dihedral angle as the chain is grown. Even though, as mentioned above, there is little indication in the experimental data that the bond lengths, bond angles, and dihedral angles in aSe vary significantly from the ideal values, adding a bit of variation to these parameters is useful for comparison purposes. Figure 9.8 shows the average EXAFS from 500 structures with varied parameters. Each bond length, bond angle, and dihedral angle in each of the 500 distinct structures was within $\pm 5\%$ of the ideal value. It is immediately apparent that the bond length in the actual aSe varies by less than 5% of the ideal value; since adding a 5% variation to the structure increases the width and decreases the height of the first EXAFS peak by a considerable amount. Secondly the ratio between the first and second EXAFS peaks is still too high to match the measured data. Changing the dihedral angle

only has an effect on the third EXAFS peak - so it is unclear whether or not aSe has large changes in this parameter. Varying the bond angle gives the best results; the secondary peak is considerably suppressed - albeit a bit wider than it appears in the measured data - while the first peak is unaffected. It is unclear whether a moderate variation in bond angle is actually present in aSe, but it does not seem unreasonable.

Chapter 10

Reverse Monte Carlo Calculations

One of the ultimate tests of crystal structure is reverse Monte Carlo (RMC) modeling. If a guided random process can recreate the same structure that was deduced by a more explicit method, then it is fairly probable that not only is the structure correct, it is also unique.

10.1 Reverse Monte Carlo EXAFS Modeling

RMC modeling can be done to reconstruct EXAFS measurements. In this approach only the density and the chemical composition of the material need be specified, the actual structure is generated by randomly distorting an arbitrary initial structure [129]. With that in mind, RMC is an attractive, albeit inefficient, means of providing verification of the twisted chain model described in Chapter 9.

The algorithm for RMC calculations is quite simple. The code under development in this research uses the following algorithm, adapted from Reference [129].

1. Create an initial arrangement of N atoms in a volume V, where the atoms consist of the appropriate stoichiometry for the material of interest, and N and V reflect the correct density.

2. Displace a random atom by a random amount, subject to a few physical constraints.

3. Calculate the average EXAFS from all relevant sites in the material.

4. Compare the average EXAFS with the experimental data.

5. If the calculated EXAFS is a better match to experiment than the calculated EXAFS from the previous iteration, keep the atomic displacement.

6. If the calculated EXAFS is a worse match to experiment than the calculated EXAFS from the previous iteration, keep the atomic displacement with a probability proportional to $\exp(\xi_n - \xi_{n-1})$, where ξ_i represents the $\mathcal{R}$-factor for iteration i. Otherwise the atom is moved back to its previous position.

7. Loop back to step 2 until the $\mathcal{R}$-factor is small enough to indicate that the calculated EXAFS is a good fit to the experimental data.

For the purposes of this research, the physical constraints for displacing an atom is listed only to keeping a minimum distance between atoms, although a general RMC algorithm can incorporate preferences for specific geometries as well [130].

An RMC approach for determining the structure of aSe was tried as early as 1968 by Kaplow *et al.*, although they modeled XRD rather than EXAFS data [37]. Recently Jóvári *et al.* studied the structure of aSe with RMC used to model the structure factor obtained from neutron diffraction [36]. Kaplow's study concluded that aSe was primarily composed of Se_8 rings [37], a result which later studies indicated was incorrect [40, 117]. The fact that the RMC algorithm used by Kaplow *et al.* only accepted "better" atomic displacements may have caused their code to converge to local minima, rather than the global optimum [36]. This emphasizes why the use of random chance in modifying the structure, in an manner which improves the overall fit, is necessary to be confident that the best RMC solution is the globally optimum one. In addition Kaplow *et al.* only used 100 atoms in their simulation. Jóvári's study used between 4000 and 16 000 atoms, and concluded that aSe was likely formed of helical chains, but that diffraction data alone could not accurately distinguish between a disordered ring-like or a disordered chain-like structure. Therefore an RMC approach using EXAFS data is of interest not only to help validate the twisted chain model used in Chapter 9, but also to compare to diffraction based RMC studies.

10.2 Implementation and Preliminary Results

An in-depth RMC model for EXAFS data would require that the average EXAFS from an arrangement of several thousand atoms match the experimental data. Since the "correct" arrangement of these atoms can only be determined by brute force, several hundred thousand, if not million, iterations may be required to optimize the structure. Obviously this is fairly computationally intensive. To obtain some preliminary results, I attempted to use RMC to model the structure of aSe starting with an $8 \times 8 \times 8$ cubic lattice of Se, but after two weeks of calculation the structure had not converged much at all, and the calculation was terminated so the computing resources could be used for more fruitful ends.

The main problem with the RMC code is that it relies on FEFF6L to calculate the EXAFS for every distinct lattice site. FEFF6L is quite fast; only taking about half a second to run, but compared to the rest of the RMC program this is the slowest step. Further, after displacing an atom the EXAFS must be recalculated not only for the displaced atom but also for every atom within 6 Å of that atom. Given the density of aSe, there are roughly 25 to 30 neighbours within a 6 Å radius of a given atom, so recalculating the EXAFS from a single displacement can take on the order of 15 seconds. Two weeks is therefore be sufficient for only a hundred thousand iterations; probably not enough to accurately resolve the structure of aSe. To write an efficient RMC code it might be necessary to use a custom, and probably less accurate, EXAFS calculation to drive the structural displacements and only rely on FEFF6L for occasional checks.

As an intermediate measure, I wrote an RMC program to model the structure around a single absorbing atom. In a sense this is similar to the approach used in the twisted chain model described in Chapter 9, although it is far less accurate. Since an EXAFS measurement only samples a few atoms in the structure - the X-ray intensity is only $\sim 10^{15}$ photons/cm^2, while the areal density of a 30 μm aSe film is $\sim 10^{20}$ atoms/cm^2 - as long as each atom has roughly the same local environment we are justified in only selecting a few. In the twisted chain model this is the case;

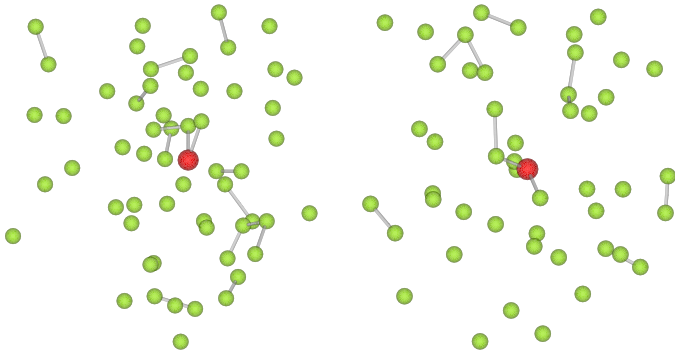

Figure 10.1: A sample cluster RMC calculation in an effort to reproduce the structure of pSe. The left hand structure started from a simple cubic arrangement, the right hand structure started from the ideal tSe arrangement.

consistent bond lengths, bond angles, and dihedral angles are required for each atom. In the RMC approach this might not be the case; since only overlapping atoms are avoided the final result may mean that neighbouring atoms may have very different local structure than the chosen core atom.

Despite the above objections, using RMC to reproduce the EXAFS from a single site is of interest in seeing how many different geometries might be possible. Further, a robust and generic single-site RMC code is useful for modeling doping sites when no other structural data is available[1]. With this in mind, I modeled the EXAFS from low temperature pSe from two sets of initial conditions: a simple cubic lattice and the normal tSe crystal structure. The first structure involved 125 atoms, the second only involved 49 atoms. Each structure was cycled through 60 000 distortions; by that point the $\mathcal{R}$-factor was more or less stable but it was still not low enough to reflect an optimum atomic arrangement.

The final structures for the simple cubic and tSe initial conditions are shown in Figure 10.1. It is surprising how much the initial tSe structure was distorted by the RMC calculation, very few bonding pairs remain. Of course one of the drawbacks of

[1]In the present case, although we have As dopants, since we still have Se EXAFS data the best approach is to fill a box with the proper ratio of As and Se atoms and use RMC to solve for both simultaneously. I am, however, participating in some other projects involving rare-earth doped glasses where only EXAFS from the rare-earth is available.

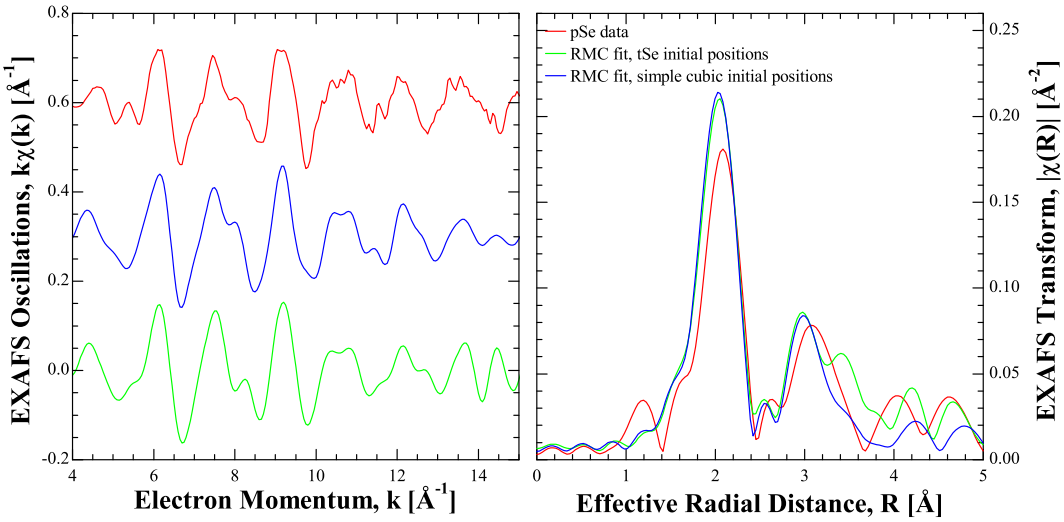

Figure 10.2: The calculated EXAFS from RMC modeling of pSe with tSe and simple cubic initial conditions compared to the actual data.

a cluster RMC approach is that only the position of the outer atoms relative to the core atom has any impact on the calculated EXAFS. The cluster calculated from an initial simple cubic lattice is qualitatively the same as that from the tSe lattice. This is a good check on the implementation of the RMC algorithm: the final result of an RMC calculation should be independent of the initial conditions.

The calculated EXAFS from these structures is shown in Figure 10.2. It is obvious that the fit leaves something to be desired. In a sense this simply demonstrates that it is futile to try to represent a low-symmetry crystal like pSe with a single site; however since the structure of tSe was fit quite successfully to the pSe data (refer back to Chapter 7) I expected better results. This may suggest that the RMC code needs to be tweaked, for example the average atomic displacement may be too large (or too small) to converge. Certainly when starting from the tSe structure, since the pSe fit in Chapter 7 suggested that the maximum deviation from the ideal lattice position was about 0.5 Å, choosing a random displacement from a uniform distribution of relative coordinates with a maximum of $\pm$ 0.5 Å might be too large, and easily cause the calculation to overshoot the ideal position.

In short, I expect RMC to be a useful tool in calculating the structure of aSe:x%As. The cluster approach is useful for testing the effectiveness of the RMC code, and suggests that my algorithm needs some adjustments. Once a single site can be efficiently fit to the EXAFS data, a proper model that attempts to fit *all* sites can be implemented.

Chapter 11

Conclusions

11.1 Summary of Results

In the course of this research I have acquired X-ray spectroscopy measurements of aSe, tSe, mSe, and aSe:x%As for x = 0.2%, 0.5%, 2%, 6%, 10%, 19%, and 39% (the last is As_2Se_3) from all available selenium edges (K-, $L_{2,3}$-, and $M_{4,5}$-edges), and several arsenic edges (K- and $M_{4,5}$-edges). The XANES and XES measurements have probed the valence and conduction band DOS, which is qualitatively consistent with DFT electronic structure calculations. I have identified a valence band feature which matches the bonding electrons and has a dependence on arsenic concentration. I have also identified a weak conduction band feature which identifies the degree of crystallization in aSe and aSe:x%As, even at room temperature.

The EXAFS data from the As and Se K-edges probes the physical structure of the material, and from that I have found bond lengths and estimated the average number of nearest neighbours. The selenium measurements are consistent with the reported spectra for aSe and tSe. The arsenic measurements show considerable structural deviations, in particular the local disorder and the number of nearest neighbours. The arsenic — selenium bond length is a bit shorter (by about 0.8 Å) than a selenium — selenium bond.

I have acquired a wide range of spectra in various measurement modes (transmission and fluorescence), at various temperatures (room temperature and ~ 30 K), and at various stages of crystallization (fresh deposit, after short annealing, after prolonged annealing). This set of spectra show a surprising range of variation in the white line height and the number of nearest neighbours. This range of variation

does not appear to be consistent with the effects of simple pin-holes or cracks in the samples.

The long range structure of polycrystalline selenium films is visible at low temperatures, but not at room temperatures. This structure was found to be consistent with the structure of tSe, as expected. However the standard impact of thermal effects on the low temperature structure is insufficient to remove all long range order at room temperature. It is also not possible for regular distortion of the tSe structure to remove the long range order. This suggests that the thermal disorder in selenium is anharmonic, and probably also asymmetric.

Polycrystallinity was induced in samples with up to 2% arsenic. These materials also appear to crystallize in the tSe form, but no long range order is seen from As edge. The regular bond length and higher coordination number of arsenic (as expected from basic chemistry) strongly suggests that arsenic is incorporated into the Se chain-like structure, rather than located in interstitial sites. The lack of long range order directly shows the retarding effect arsenic has on selenium crystallization.

Finally the structure of aSe appears to be consistent with the twisted chain model, although it is possible that the bond angles have around 5% variation from the ideal value throughout the structure. Reverse Monte Carlo modeling seems to also be a viable method for determining the structure of aSe, although additional work is needed to fine tune the algorithm.

11.2 Future Work

Obviously many parts of this thesis are still "work in progress", and additional fine-tuning of the distorted chain structural model and the RMC calculations are necessary to produce useful results for aSe:x%As. Given the scope of this project, and the likelihood of my future involvement in spectroscopic studies of glasses - in particular rare-earth doped chalcogenide and ZBLAN glasses - I would like to make these models as robust and generic as possible, so they may easily be extended different materials.

There are two immediate follow-up projects underway; one involving the XANES "fingerprint" of crystallization, the other the XES "fingerprint" of arsenic concentration. After conversations with Dr. Alex Kolobov the past summer, we are collaborating on investigating further the XANES feature which tracks the degree of crystallization. Dr. Kolobov has recently (November, 2009) performed measurements of gradually annealed aSe at SPring-8 and has reproduced my findings (refer back to Chapter 7). He was able to heat the samples *in situ*, and therefore he has even more measurements than I have and the gradual change from aSe to tSe is very clear. We are planning on conducting additional measurements at SPring-8 (which I hope to attend) this summer, where the crystallization of aSe:x%As and the effect of different substrates will be examined.

Finally, Prof. Kasap is interested in measuring the sensitivity of the bonding-pair *4p* electrons probed by the Se $M_{4,5}$-edge XES to substrate temperature. In particular he would like me to acquire measurements of As_2Se_3 deposited on substrates far above and far below the glass transition temperature. This research will probably be conducted this April at the ALS.

References

[1] D. M. Pai and R. C. Enck. Onsager mechanism of photogeneration in amorphous selenium. *Physical Review B*, 11(12):5163, 1975.

[2] J. L. Hartke. Drift mobilities of electrons and holes and space-charge-limited currents in amorphous selenium films. *Physical Review*, 125(4):1177, 1962.

[3] M. D. Tabak and P. J. Warter. Field-controlled photogeneration and free-carrier transport in amorphous selenium films. *Physical Review*, 137(3):899, 1968.

[4] H. P. Grunwald and R. M. Blakney. Electron and hole drift mobilities in vitreous selenium. *Physical Review*, 165(3):1006, 1968.

[5] B. Kramer, K. Maschke, and L. D. Laude. Electronic spectra of trigonal and disordered phases of tellurium and selenium, I. Theory. *Physical Review B*, 8(12):5781, 1973.

[6] L. D. Laude, B. Kramer, and K. Maschke. Electronic spectra of trigonal and disordered phases of tellurium and selenium, II. Experiment. *Physical Review B*, 8(12):5794, 1973.

[7] Y. Katayama, M. Yao, Y. Ajiro, M. Inui, and H. Endo. Photo-induced phenomena in isolated selenium chains. *Journal of the Physical Society of Japan*, 58(5):1811, 1989.

[8] A. V. Kolobov, H. Oyanagi, K. Tanaka, and Ke. Tanaka. Structural study of amorphous selenium by *in situ* EXAFS: Observation of photoinduced bond alternation. *Physical Review B*, 55:726, 1997.

[9] I. M. Blevis, D. C. Hunt, and J. A. Rowlands. Measurement of X-ray photogeneration in amorphous selenium. *Journal of Applied Physics*, 85(11):7958, 1999.

[10] W. D. Oliphant. Xeroradiography I. Apparatus and method of use. *British Journal of Radiology*, 28:543, 1955.

[11] P. B. Sewell. Electron-image recording by xerography. *Nature*, 179:773, 1957.

[12] J. A. Rowlands and S. O. Kasap. Amorphous semiconductors usher in digital X-ray imaging. *Physics Today*, 50:24, 1997.

[13] D. C. Hunt, O. Tousignant, Y. Demers, L. Laperriere, and J. A. Rowlands. Imaging performace of an amorphous selenium flat-panel detector for digital fluoroscopy. In M. J. Yaffe and L. E. Antonuk, editors, *Medical Imaging 2003 Proceedings of SPIE*, volume 5030, page 226. SPIE, 2003.

[14] O. Tousignant, Y. Demers, and L. Laperriere. a-Se flat panel detectors for medical applications. In *Sensors Applications Symposium*, San Diego, CA, 2007. Instrumentation and Measurement Society, IEEE.

[15] S. O. Kasap, M. Zahangir Kabir, and J. A. Rowlands. Recent advances in X-ray photoconductors for direct conversion X-ray image detectors. *Current Applied Physics*, 6:288, 2006.

[16] S. O. Kasap and J. A. Rowlands. Direct-conversion flat-panel X-ray image sensors for digital radiography. *Proceedings of the IEEE*, 90(4):591, 2002.

[17] W. Que and J. A. Rowlands. X-ray imaging using amorphous selenium: inherent spatial resolution. *Medical Physics*, 22(4):365, 1995.

[18] V. Loustauneau, M. Bissonnette, S. Cadieux, M. Hansroul, E. Masson, S. Savard, B. Polischuk, and M. Lehtimäki. Imaging performance of a clinical selenium flat-panel detector for advanced applications in full-field digital mammography. In M. J. Yaffe and L. E. Antonuk, editors, *Medical Imaging 2003 Proceedings of SPIE*, volume 5030, page 1010. SPIE, 2003.

[19] ANRAD Corporation. The smam digital detector product information. http://www.anrad.com, Saint-Laurent, QC, 2004. Technical datasheet.

[20] B. B. Buchanan, J. J. Bucher, D. E. Carlson, N. M. Edelstein, E. A. Hudson, N. Kaltsoyannis, T. Leighton, W. Lukens, D. K. Shuh, H. Nitsche, T. Reich, K. Roberts, P. Torretto, J. Woicik, W.-S. Yang, A. Yee, and B. C. Yee. A XANES and EXAFS investigation of the speciation of selenite following bacterial metabolization. *Inorganic Chemistry*, 34:1617, 1995.

[21] J. D. Joannopoulos, M. Schlüter, and M. L. Cohen. Electronic structure of trigonal and amorphous Se and Te. *Physical Review B*, 11(6):2186, 1975.

[22] P. Cherin and P. Unger. The crystal structure of trigonal selenium. *Inorganic Chemistry*, 6(8):1589, 1967.

[23] O. Foss and V. Janickis. X-ray crystal structure of a new red, monoclinic form of cyclo-octaselenium, Se_8. *Journal of the chemical Society, Chemical Communications*, page 834, 1977.

[24] W. E. Spear. Carrier mobility and charge transport in monoclinic Se crystals. *Journal of Physics and Chemistry of Solids*, 21(1/2):110, 1995.

[25] K. E. Murphy, M. B. Altman, and B. Wunderlich. The monoclinic-to-trigonal transformation in selenium. *Journal of Applied Physics*, 48(10):4122, 1977.

[26] Y. Miyamoto. Growth of trigonal selenium from CS_2 solution. *Japanese Journal of Applied Physics*, 16(12):2257, 1977.

[27] T. Takahashi, K. Murano, K. Nagata, and Y. Miyamoto. X-ray photoemission study of a new allotrope of solid selenium (rhombohedral Se consisting of Se_6 ring molecules. *Physical Review B*, 28(8):4893, 1983.

[28] R. W. G. Wyckoff. *Crystal Structures 1*, chapter 7-83. Interscience Publishers, New York, 2^{nd} edition, 1963.

[29] S. O. Kasap. *Handbook of Imaging Materials*, chapter 9. Marcel Dekker, Inc., New York, 2^{nd} edition, 2002.

[30] S. O. Kasap. X-ray sensitivity of photoconductors: application to stabilized a-Se. *Journal of Physics D: Applied Physics*, 33:2853, 2000.

[31] S. Chand, G. D. Sharma, R. C. Batheja, and S. Chandra. Photostructural defect states and residual potential in chlorine and arsenic doped amorphous selenium films. *Applied Physics Letters*, 61(16):1915, 1992.

[32] G. Belev and S. O. Kasap. Amorphous selenium as an X-ray photoconductor. *Journal of Non-Crystalline Solids*, 345,346:484, 2004.

[33] R. Parthasarathy, P. R. Sarode, and K. J. Rao. An EXAFS study of amorphous selenium. *Journal of Materials Science*, 16(11):3222, 1981.

[34] B. A. Vaid and K. C. Sharma. Structural disorder model for amorphous semiconductors: a-Se. *physica status solidi (b)*, 137:433, 1986.

[35] D. Caprion and H. R. Schober. Structure and relaxation in liquid and amorphous selenium. *Physical Review B*, 62(6):3709, 2000.

[36] P. Jóvári, R. G. Delaplane, and L. Pusztai. Structural models of amorphous selenium. *Physical Review B*, 67:172201, 2003.

[37] R. Kaplow, T. A. Rowe, and B. L. Averbach. Atomic arrangement in vitreous selenium. *Physical Review*, 168(3):1068, 1968.

[38] R. Brüning, E. Irving, and G. LeBlanc. Reverse monte carlo study of structural relaxation in vitreous selenium. *Journal of Applied Physics*, 89(6):3215, 2001.

[39] T. Takahashi, K. Ohno, and Y. Harada. Highly disordered amorphous selenium studied by ultraviolet photoemission spectroscopy. *Physical Review B*, 21(8):3399, 1980.

[40] A. A. Baganich, V. I. Mikla, D. G. Semak, A. P. Sokolov, and A. P. Shebanin. Raman scattering in amorphous selenium. *physica status solidi (b)*, 166:297, 1991.

[41] C. C. Lo, B. Taylor, H. Lancaster, and J. Guigli. Advanced light source linac subharmonic buncher cavities. In *Particle Accelerator Conference, Proceedings of the IEEE*, volume 2, page 956, 1989.

[42] L. O. Dallin and R. M. Silzer. *Booster Ring*. Canadian Light Source Incorporated, 1999. http://www.lightsource.ca/operations/pdf/CLS.Design.2.1.28.pdf.

[43] J. Tanabe, J. Krupnick, E. Hoyer, and A. Paterson. Magnet costs for the advanced light source. In *Proceedings of the 1993 Particle Accelerator Conference*, volume 4, page 2850. IEEE, 1993.

[44] J. Hinkson. Advanced light source beam position monitor. In *Proceedings of the Accelerator Instrumentation Workshop*, 1991. OSTI ID: 1013499, http://www.osti.gov/.

[45] L. Dallin, I. Blomqvist, M. de Jong, D. Lowe, and M. Silzer. The Canadian Light Source. In *Proceedings of the 2003 Particle Accelerator Conference*, page 220, 2003.

[46] Advanced Light Source. *ALS Storage Ring Parameters*. Lawrence Berkeley National Laboratory, 2006. http://www.als.lbl.gov/als/techspecs/srparameters.html.

[47] D. T. Jiang, N. Chen, and W. Sheng. Wiggler-base hard X-ray spectroscopy beamline at CLS. In *AIP Conference Proceedings*, volume 879, page 800, 2007.

[48] T. Regier, J. Paulsen, G. Wright, I. Coulthard, K. Tan, T. K. Sham, and R. I. R. Blyth. Comissioning of the spherical grating monochromator soft X-ray spectroscopy beamline at the canadian light source. In *AIP Conference Proceedings*, volume 879, page 473, 2007.

[49] T. Regier, J. Krochak, T. K. Sham, Y. F. Hu, J. Thompson, and R. I. R. Blyth. Performance and capabilities of the Canadian Dragon: The SGM beamline at the Canadian Light Source. *Nuclear Instruments and Methods in Physics Research A*, 582:93, 2007.

[50] Y. F. Hu, L. Zuin, G. Wright, R. Igarashi, M. McKibben, T. Wilson, S. Y. Chen, T. Johnson, D. Maxwell, B. W. Yates, T. K. Sham, and R. Reininger. Commissioning and performance of the variable line spacing plane grating monochromator beamline at the Canadian Light Source. *Review of Scientific Instruments*, 78:083109, 2007.

[51] R. Reininger, K. Tan, and I. Couthard. An insertion device beamline for 5-250 eV at the Canadian Light Source. *Review of Scientific Instruments*, 73(3):1489, 2002.

[52] J. J. Jia, T. A. Callcott, J. Yurkas, A. W. Ellis, F. J. Himpsel, M. G. Samant, J. Stöhr, D. L. Ederer, J. A. Carlisle, E. A. Hudson, L. J. Terminello, D. K. Shuh, and R. C. C. Perera. First experimental results from EM/TENN/TULANE/LLNL/LBL beamline at the advanced light source. *Review of Scientific Instruments*, 66:1394, 1995.

[53] D. Attwood. *Soft X-rays and Extreme Ultraviolet Radiation*, chapter 1. Cambridge University Press, New York, 1999.

[54] E.A. Stern and K. Kim. Thickness effect on the extended-x-ray-absorption-fine-structure amplitude. *Physical Review B*, 23(8):3781, 1981.

[55] B. L. Henke, E. M. Gullikson, and J. C. Davis. X-ray interactions: photoabsorption, scattering, transmission, and reflection at E=50-30000 eV, Z=1-92. *Atomic Data and Nuclear Data Tables*, 54(2):181, 1993. http://henke.lbl.gov/optical_constants/.

[56] D. E. Sayers, E. A. Stern, and F. W. Lytle. New technique for investigating noncrystalline structures: Fourier analysis of the extended X-ray-absorption fine structure. *Physical Review Letters*, 27(18):1204, 1971.

[57] E. A. Stern. Theory of the extended x-ray-absorption fine structure. *Physical Review B*, 10(8):3027, 1974.

[58] F. W. Lytle, D. E. Sayers, and E. A. Stern. Extended x-ray-absorption fine-structure technique. II. Experimental practice and selected results. *Physical Review B*, 11(12):4825, 1975.

[59] E. A. Stern, D. E. Sayers, and F. W. Lytle. Extended x-ray-absorption fine-structure technique. III. Determination of physical parameters. *Physical Review B*, 11(12):4836, 1975.

[60] H. Bethe and E. Saltpeter. *Quantum Mechanics of One and Two Electron Systems*, chapter 59, 69. Springer-Verlag, Berlin, 1957.

[61] C. A. Ashley and S. Doniach. Theory of extended x-ray absorption edge fine structure (EXAFS) in crystalline solids. *Physical Review B*, 11(4):1279, 1975.

[62] L. S. Rodberg and R. M. Thaler. *Introduction to the Quantum Theory of Scattering*, page 118. Academic, New York, 1967.

[63] S. Kelly, R. Ingalls, F. Wang, B. Ravel, and D. Haskel. X-ray-absorption fine-structure study of the B1-to-B2 phase transition in RbCl. *Physical Review B*, 57(13):7543, 1998.

[64] P. A. Lee and J. B. Pendry. Theory of the extended x-ray absorption fine structure. *Physical Review B*, 11(8):2795, 1975.

[65] J. L. Beeby. The diffraction of low-energy electrons by crystals. *Journal of Physics C*, 1(1):82, 1968.

[66] J. B. Pendry. Ion core scattering and low energy electron diffraction - I. *Journal of Physics C*, 4(16):2501, 1971.

[67] P. A. Lee and G. Beni. New method for calculation of atomic phase shifts: Application to extended X-ray absorption fine structure (EXAFS) in molecules and crystals. *Physical Review B*, 15(6):2862, 1977.

[68] J. J. Rehr, J. Mustre de Leon, S. I. Zabinsky, and R. C. Albers. Theoretical X-ray absorption fine structure standards. *Journal of the American Chemical Society*, 113(14):5135, 1991.

[69] J. J. Rehr and R. C. Albers. Theoretical approaches to x-ray absorption fine structure. *Review of Modern Physics*, 72(3):621, 2000.

[70] S. I. Zabinsky, J. J. Rehr, A. Ankudinov, R. C. Albers, and M. J. Eller. Multiple-scattering calculations of x-ray-absorption spectra. *Physical Review B*, 52(4):2995, 1995.

[71] J. J. Kas, A. P. Sorini, M. P. Prange, L. W. Campbell, J. A. Soininen, and J. J. Rehr. Many-pole model of inelastic losses in x-ray absorption spectra. *Physical Review B*, 76:195116, 2007.

[72] M. Newville, B. Ravel, D. Haskel, J. J. Rehr, E. A. Stern, and Y. Yacoby. Analysis of multiple-scattering XAFS data using theoretical standards. *Physica B*, 208,209:154, 1995.

[73] M. Newville. IFEFFIT: interactive XAFS analysis and FEFF fitting. *Journal of Synchrotron Radiation*, 8:322, 2001.

[74] B. Ravel and M. Newville. ATHENA, ARTEMIS, HEPHAESTUS: data analysis for X-ray absorption spectroscopy using IFEFFIT. *Journal of Synchrotron Radiation*, 12:537, 2005.

[75] M. Newville. FEFFIT: Using FEFF to model XAFS data. http://cars9.uchicago.edu/ifeffit/Documentation, 1998.

[76] E. A. Stern. The future of XAFS. *Japanese Journal of Applied Physics*, 32(2):851, 1993.

[77] J. A. Victoreen. Probable X-ray mass absorption coefficients for wave-lengths shorter than the ıK critical absorption wave-length. *Journal of Applied Physics*, 14:95, 1943.

[78] J. A. Victoreen. Atomic absorption coefficient for X-rays. *Physical Review Letters*, 72:869, 1947.

[79] M. Newville, P. Līviņš, Y. Yacoby, J. J. Rehr, and E. A. Stern. Near-edge X-ray-absorption fine structure of Pb: A comparison of theory and experiment. *Physical Review B*, 47(21):14126, 1993.

[80] P. Blaha, K. Schwarz, G. K. H. Madsen, D. Kvasnicka, and J. Luitz. ***WIEN2k***, *An Augmented Plane Wave + Local Orbitals Program for Calculating Crystal Properties*. Karlheinz Schwarz, Technische Universität Wien, Austria, 2001. ISBN 3-9501031-1-2.

[81] K. Hermann, L. G. M. Pettersson, M. E. Casida, C. Daul, A. Goursot, A. Koester, E. Proynov, A. St-Amant, and D. R. Salahub. Stobe-demon version 3.0. Contributing Authors: V. Carravetta, H. Duarte, C. Friedrich, N. Godbout, J. Guan, C. Jamorski, M. Leboeuf, M. Leetmaa, M. Nyberg, S. Patchkovskii, L. Pedocchi, F. Sim, L. Triguero, and A. Vela, 2009.

[82] S. Cottenier. *Density Functional Theory and the family of (L)APW-methods: a step-by-step introduction*. Instituut voor Kern- en Stralingsfysica, K. U. Leuven, Belgium, 2004. ISBN 90-807215-1-4.

[83] D. S. Sholl and J. A. Steckel. *Density Functional Theory: A Practical Introduction*, chapter 1. John Wiley & Sons, Inc., Hoboken, New Jersey, 2009.

[84] R. M. Martin. *Electronic Structure: Basic Theory and Practical Methods*, chapter 2, 6, 7, 8. Cambridge University Press, Cambridge, 2004.

[85] P. Hohenberg and W. Kohn. Inhomogeneous electron gas. *Physical Review*, 136(3B):864, 1964.

[86] N. D. Mermin. Thermal properties of the inhomogeneous electron gas. *Physical Review*, 137(5A):1441, 1965.

[87] W. Kohn and L. J. Sham. Self-consistent equations including exchange and correlation effects. *Physical Review*, 140(4A):1133, 1965.

[88] F. Herman, J. P. Van Dyke, and I. B. Ortenburger. Improved statistical exchange approximation for inhomogeneous many-electron systems. *Physical Review Letters*, 22:807, 1969.

[89] A. D. Becke. Density-functional exchange-energy approximation with correct asymptotic behaviour. *Physical Review A*, 38:3098, 1988.

[90] J. P. Perdew and Y. Wang. Accurate and simple analytic representation of the electron-gas correlation energy. *Physical Review B*, 45:13244, 1992.

[91] J. P. Perdew, K. Burke, and M. Ernzerhof. Generalized gradient approximation made simple. *Physical Review Letters*, 77:3865, 1996.

[92] S. F. Boys. Electronic wave functions. 1. A general method of calculation for the stationary states of any molecular system. *Proceedings of the Royal Society of London. Series A, Mathematical and Physical Sciences*, 200(1063):542, 1950.

[93] J. P. Perdew. Density-functional approximation for the correlation energy of the inhomogeneous electron gas. *Physical Review B*, 33:8822, 1986.

[94] K. Schwarz, A. Neckel, and J. Nordgren. On the X-ray emission spectra from FeAl. *Journal of Physics F: Metal Physics*, 9:2509, 1979.

[95] S. O. Kasap, K. V. Koughia, B. Fogal, G. Belev, and R. E. Johanson. The influence of deposition conditions and alloying on the electronic properties of amorphous selenium. *Semiconductors*, 37(7):789, 2003.

[96] K. Y. Rajpure, C. D. Lokhande, and C. H. Bhosale. Effect of the substrate temperature on the properties of spray deposited Sb-Se thin films from non-aqueous medium. *Thin Solid Films*, 311:114, 1997.

[97] F. C. Brown. The crystal forms of metallic selenium and some of their physical properties. *Physical Review*, 4(2):85, 1914.

[98] H. P. Grunwald. Crystalline growth of monoclinic selenium. *Materials Research Bulletin*, 7(10):1093, 1973.

[99] F. Q. Guo and K. Lu. Amorphous-nanocrystalline-amorphous phase transformations in Se induced by mechanical attrition. *Philosophy Magazine Letters*, 77(4):181, 98.

[100] W. T. Elam, B. Ravel, and J. R. Sieber. A new atomic database for X-ray spectroscopic calculations. *Radiation Physics and Chemistry*, 63:121, 2002.

[101] W. H. McMaster, N. Kerr Del Grande, J. H. Mallett, and J. H. Hubbell. *Lawrence Livermore National Laboratory Report: Compilation of X-ray Cross Sections*. National Bureau of Standards, 1969.

[102] C. T. Chantler. X-ray form factor, attenuation, and scattering tables. *Journal of Physical and Chemical Reference Data*, 24:71, 1995. http://physics.nist.gov/PhysRefData/FFast/html/form.html.

[103] S. Brennan and P. L. Cowen. A suite of programs for calculating X-ray absorption, reflection, and diffraction performance for a variety of materials at arbitrary wavelengths. *Review of Scientific Instruments*, 63:850, 1992.

[104] A. Wolska and R. Bacewicz. X-ray absorption near-edge structure of selenium in the Cu-In-Se system. *Journal of Physics: Condensed Matter*, 13:4457, 2001.

[105] B. Akabayov, C. J. Doonan, I. J. Pickering, G. N. George, and I. Sagi. Using softer X-ray absorption spectroscopy to probe biological systems. *Journal of Synchrotron Radiation*, 12:392, 2005.

[106] M. P. Givens and W. P. Siegmund. The absorption of selenium in the soft X-ray region. *Physical Review*, 85(2):313, 1952.

[107] H. Bertagnolli and T. S. Ertel. X-ray absorption spectroscopy of amorphous solids, liquids, and catalytic and biochemical systems - capabilities and limitations. *Agnewandte Chemistry International Edition (English)*, 33:45, 1994.

[108] J. C. Phillips, C. A. Beevers, and S. E. B. Gould. Molecular structure of As_2Se_3 glass. *Physical Review B*, 21(12):5724, 1980.

[109] B. Ravel and S. D. Kelly. The difficult chore of measuring coordination by EXAFS. In B. Hedman and P. Pianetta, editors, *Proceedings of the X-ray Absorption Fine Structure 13th International Conference*, 2006. SLAC eConf C060709, http://www.slac.standford.edu/econf/C060709/proceedings.htm.

[110] N. Dimakis and G. Bunker. *Ab initio* single- and multiple-scattering EXAFS debye-waller factors: Raman and infrared data. *Physical Review B*, 58(5):2467, 1998.

[111] P. Cherin and P. Unger. Refinement of the crystal structure of α-monoclinic Se. *Acta Crystallography*, B28:313, 1971.

[112] D. Hohl and R. O. Jones. First-principles molecular-dynamics simulation of liquid and amorphous selenium. *Physical Review B*, 43(5):3856, 1991.

[113] A. V. Kolobov, H. Oyanagi, and K. Tanaka. *In situ* X-ray absorption fine structure detection of reversible photoinduced anisotropy in amorphous selenium. *Physical Review Letters*, 87(14):145502, 2001.

[114] M. Majid, S. Bénazeth, C. Souleau, and J. Purans. XAFS study of interchain and intrachain order in $Se_{1-x}Te_x$ glasses: Nearest neighbours. *Physical Review B*, 58:6104, 1998.

[115] Y. H. Zhao, K. Lu, and T. Liu. EXAFS study of structural characteristics of nanocrystalline selenium with different grain sizes. *Physical Review B*, 59(17):11117, 1999.

[116] M. F. Kotkata. Phase-property study of semiconductor selenium: Part ii double-phase system. *Journal of Materials Science*, 27:4858, 1992.

[117] M. F. Kotkata. Phase-property study of semiconductor selenium. *Journal of Material Science*, 27:4847, 1992.

[118] E. A. Stern, R. W. Siegel, M. Newville, P. G. Sanders, and D. Haskel. Are nanophase grain boundaries anomalous? *Physical Review Letters*, 75(21):3874, 1995.

[119] E. Voronina, D. Guy, and T. Miyanaga. Thickness effect correction in XAFS-spectroscopy: Temperature measurement approach. *Nuclear Instruments and Methods in Physics Research B*, 215:525, 2004.

[120] P. Nielsen. Density of states of amorphous selenium by vacuum photoemission. *Physical Review B*, 6(10):3739, 1972.

[121] N. J. Shevchik, M. Cardona, and J. Tejeda. X-ray and far-uv photoemission from amorphous and crystalline films of Se and Te. *Physical Review B*, 8(6):2833, 1973.

[122] N. J. Shevchik. Newer interpretation of the photoemission spectra of amorphous and trigonal selenium films. *Physical Review Letters*, 33(26):1572, 1974.

[123] T. Takahashi. Comparative X-ray-photoemission study of monoclinic, trigonal, and amorphous selenium. *Physical Review B*, 26(10):5963, 1982.

[124] T. Takahashi and T. Sagawa. Highly disordered amorphous selenium studied by X-ray photoemission spectroscopy. *Physical Review B*, 26(12):7039, 1982.

[125] G. Dalba and P. Fornasini. EXAFS debye-waller factor and thermal vibrations of crystals. *Journal of Synchrotron Radiation*, 4:243, 1997.

[126] E. Sevillano, H. Meuth, and J. J. Rehr. Extended X-ray absorption fine structure debye-waller factors. I. Monatomic crystals. *Physical Review B*, 20(12):4908, 1979.

[127] C. Kittel. *Introduction to Solid State Physics*, chapter 5. John Wiley & Sons, Inc., Hoboken, NJ, 7^{th} edition, 1953.

[128] O. Madelung, U. Rössler, and M. Schulz, editors. *Non-Tetrahedrally Bonded Elements and Binary Compounds I*, volume 41C of *Landolt-Börstein - Group III Condensed Matter*, chapter Selenium (Se) Debye temperature, heat capacity, density, melting point, trigonal Se. Springer-Verlag, 1998.

[129] S. J. Gurman and R. L. McGreevy. Reverse Monte Carlo simulation for the analysis of EXAFS data. *Journal of Physics: Condensed Matter*, 2:9463, 1990.

[130] M. A. Howe, R. L. McGreevy, L. Pusztai, and I. Borzsák. Determination of three body correlation in simple liquids by RMC modelling of diffraction data. II. Elemental liquids. *Physics and Chemistry of Liquids*, 25:205, 1993.

Appendix A

Summary of X-ray Spectra

The following is a summary of the X-ray measurements performed in the context of this thesis. The beamline, beamline settings, measurement technique, and samples measured are all briefly described.

1. **October 2007**: Room temperature measurements taken at BL8. Low energy monochromator and low energy spectrometer gratings were used. The ALS ring was at 1.9 GeV with peak operating current of 400 mA. Se $M_{4,5}$-edge XES measurements of aSe, aSe:0.2%As, and Se:0.5%As were taken. Some of the aSe:0.5%As had 10, 11, and 40 ppm Cl added. These spectra are not very useful, there is significant low-energy noise. Most of the emission was excited at 168 eV, one measurement was excited at 100 eV. The only difference between the spectra taken at the two excitation energies is the counting statistics, results were generally a bit better at 168 eV excitation.

2. **November 2007**: Room temperature measurements taken at the HXMA beamline with an Si(111) monochromator crystal and an Rh-plated mirror. The wiggler was at 1.9 T, and the primary slit at 1.0 × 5.0 mm. The CLS ring was at 2.9 GeV with peak operating current of 250 mA. Transmission mode XANES and EXAFS measurements were taken of the Se K-edge for aSe and aSe:0.5%As, and Se and Se:0.5%As annealed at 60° C for 14 hours. Fluorescent mode XANES and EXAFS measurements with the 32-element germanium spectrometer were taken of the As K-edge for aSe:0.5%As and Se:0.5%As annealed at 60° C for 14 hours.

3. **December 2007**: Room temperature measurements taken at the HXMA beamline with an Si(220) monochromator crystal and an Rh-plated mirror. The wiggler was at 1.9 T, and the primary slit at 1.5 × 1.5 mm. The CLS ring was at 2.9 GeV with peak operating current of 250 mA. Transmission mode XANES and EXAFS measurements were taken of the Se K-edge for aSe:0.2%As, aSe:10%As, and Se:0.2%As annealed at 80° C for 16 hours. Fluorescent mode XANES and EXAFS measurements with the Saturn-Vortex spectrometer were taken of the As K-edge for aSe:0.2%As, aSe:0.5%As, aSe:2%As, aSe:6%As, aSe:10%As, and Se:0.2%As annealed at 80° C for 16 hours.

4. **January 2008**: Room temperature measurements taken at the SGM beamline. The high energy grating and the third undulator harmonic were used, the slits were set to 250 μm/20 μm. Se $L_{2,3}$-edge XANES measurements of aSe, aSe:0.2%As, aSe:0.5%As, aSe:2%As, aSe:6%As, aSe:10%As, SeO_2, and tSe were taken. Data are not very interesting.

5. **February 2008**: Room temperature measurements taken at the HXMA beamline with an Si(220) monochromator crystal and an Rh-plated mirror. The wiggler was at 1.9 T, and the primary slit at 1.5 × 1.5 mm. The CLS ring was at 2.9 GeV with peak operating current of 250 mA. Transmission mode XANES and EXAFS measurements were taken of the Se K-edge for aSe, aSe progressively annealed at 60° C, 80° C, and finally 100° C for 3 hours each, aSe:0.2%as, aSe:10%As progressively annealed at 60° C, 80° C, and finally 100° C for 3 hours each, SeO_2, tSe, and As_2Se_3. Transmission mode XANES and EXAFS measurements were taken of the As K-edge for As_2Se_3.

6. **April 2008**: Room temperature and low temperature (∼30 K) measurements taken at BL8. The ALS ring was at 1.9 GeV with peak operating current of 400 mA. Low energy monochromator and low energy spectrometer gratings were used. A liquid helium cryostat was used to bring the sample down to ∼30 K while in UHV. Se $M_{4,5}$-edge XES measurements of aSe, aSe:0.2%As, aSe:10%As, SeO_2, tSe, and As_2Se_3 were taken. A strange high-energy low temperature feature is inconsistently present in some measurements.

7. **September 2008**: Room temperature measurements taken at the PGM beamline. Medium energy grating, 50 μm entrance and exit slit, and 1s dwell time. The CLS ring was at 2.9 GeV with peak operating current of 250 mA. Se $M_{4,5}$-edge XANES in TEY and TFY mode measurements of aSe, aSe:0.2%As, aSe:2%As, aSe:6%As, aSe10%As, tSe, SeO_2, and As_2Se_3 were taken. As $M_{4,5}$-edge XANES in TEY and TFY mode measurements of As_2Se_3 were taken. Some of the aSe measurements appear to show progressive radiation damage in the ratios of the M_4, M_5 peaks. This was measured repeatedly by opening the slits to 250 μm for a brief period, then measuring the sample with 5 μm slits.

8. **October 2008**: Room temperature and low temperature (∼30 K) measurements taken at BL8. The ALS ring was at 1.9 GeV with peak operating current of 500 mA. Low energy monochromator and low energy spectrometer gratings were used. A liquid helium cryostat was used to bring the sample down to ∼30 K while in UHV. Se $M_{4,5}$-edge XES measurements of aSe, aSe:0.2%As, aSe:0.5%As, aSe:2%As, aSe:6%As, aSe:10%As, and As_2Se_3 were taken. The previously noted low temperature feature is no longer visible.

9. **November 2008**: Low temperature measurements taken at the HXMA beamline with an Si(220) monochromator crystal and an Rh-plated mirror. The wiggler was at 1.9 T, and the primary slit at 1.5 × 1.5 mm. The CLS ring was at 2.9 GeV with peak operating current of 250 mA. A liquid helium cryostat with beryllium windows was used to cool the samples to ∼30 K. Se K-edge transmission XANES and EXAFS were taken of aSe, pSe, tSe, mSe, aSe:0.2%As, pSe:0.2%As, and aSe:10%As. As K-edge transmission XANES and EXAFS were taken of aSe:0.2%As and aSe:10%As.

10. **January 2009**: Low temperature measurements taken at the HXMA beamline with an Si(220) monochromator crystal and an Rh-plated mirror. The wiggler was at 1.9 T, and the primary slit at 1.5 × 1.5 mm. The CLS ring was at 2.9 GeV with peak operating current of 250 mA. A liquid helium cryostat with beryllium windows was used to cool the samples to ∼30 K. Se K-edge transmission XANES and EXAFS measurements were taken of aSe, pSe, aSe:0.5%As, pSe:0.5%As, aSe:2%As, pSe:2%As, aSe:6%As, pSe:6%As, aSe10%As, pSe:10%As, aSe:19%As, and pSe:19%As. As K-edge transmission XANES and EXAFS measurements were taken of pSe:2%As, pSe:6%As, aSe:10%As, pSe:10%As, aSe:19%As, and pSe:19%As. Fluorescence XANES and EXAFs measurements of pSe:0.5%As were taken with the 32-element Ge detector, and of aSe:0.2%As and pSe:0.2%As with the Saturn-Vortex detector. The pSe:x%As were annealed at 100° C for 24 hours for x $\leq$ 6, and at 110° C for 100 hours for x $<$ 6. Although listed as "polycrystalline", for x $>$ 2% no long range order was present.

Appendix B

EXAFS Data Processing Procedure

The EXAFS data files were calibrated and treated according to the following steps.

1. If applicable, the relevant channels from the 32-element Ge detectors are summed.
2. The data points in regions where there is a monochromator glitch are removed.
3. The energy is calibrated using Bragg's law.
4. The deglitched and calibrated data is imported into Athena.
5. Athena is used to align the derivatives of the repeated spectra (this is a correction only on the order of ~ 0.1 eV), and the repeated spectra are summed together.
6. Athena is used to remove the background (using AUTOBK [79]), and extract the EXAFS oscillations $\chi(k)$.

Often some channels on the 32-element Ge detector were burnt out (frequently channel 13 had problems) and these channels were discarded.

Monochromator glitches were identified from the I_0 current of several different scans. Data points falling in this energy range were removed entirely. These glitch regions are listed in Table B.1.

The calibration energies were chosen somewhat arbitrarily. The reference spectra were calibrated to literature values at the peak in the first derivative on the absorption edge (the "absorption threshold"). The calibrated energy scale was calculated by comparing the measured absorption threshold E_{meas} with a theoretical standard E_{cal}. For this research, $E_{cal} = 12658.0$ eV for the Se K-edge, and $E_{cal} = 11919.0$

Table B.1: Monochromator glitches for an Si(111) and Si(220) crystal in the As to Se K-edge energy range.

Si(111) Crystal [eV]	Si(220) Crystal [eV]
12045.0 — 12055.0	12298.0 — 12323.0
12122.0 — 12129.0	1250.0 — 12560.0
12254.0 — 12303.0	12930.0 — 12940.0
12490.0 — 12500.0	13250.0 — 13270.0
14053.0 — 14076.0	13650.0 — 13670.0
14112.0 — 14135.0	14165.0 — 14185.0

for the Au L_3-edge (used as the reference standard for the As K-edge measurements) [100]. The correction factor to the monochromator angle was calculated as follows:

$$\Delta\phi = \sin^{-1}\left(\frac{hc}{2E_{meas}d}\right) - \sin^{-1}\left(\frac{hc}{2E_{cal}d}\right) \tag{B.1}$$

Where d is the distance between crystal planes in the monochromator, h is Planck's constant, and c is the speed of light. For an Si(111) crystal, $d = 3.1356$ Å and for an Si(220) crystal, $d = 1.9102$ Å. The monochromator angle correction is then used to calculate the calibrated energy scale E':

$$E' = \frac{hc}{2d\sin\left(\sin^{-1}\left(\frac{hc}{Ed}\right) - \Delta\phi\right)} \tag{B.2}$$

Although deglitching will leave "holes" in the energy scale, Athena automatically interpolates $\chi(k)$ onto a regular grid. Since even with missing data points $\chi(k)$ oscillates very slowly compared to the measured energy steps this interpolation is quite accurate.

Appendix C

Construction of Selenium Chain

Calculating the possible positions of atoms in a Se chain with a specified bond length b, bond angle θ, and dihedral angle ϕ is fairly straightforward. However since the equations are rather long, I will explicitly derive the result.

The position of a single Se atom is obviously completely arbitrary. To construct a chain, the second atom placed has a single constraint: it must be a specific distance (the bond length) from the first atom. The second atom can therefore be located anywhere on the surface of a sphere of radius b with the first atom at the centre.

The third atom then has two constraints: it must have the correct bond length from with the second atom and the second atom must be the vertex of the correct bond angle. The second atom can therefore be located anywhere on the perimeter of a circle of radius $b\sin(\theta)$ that is $-b\cos(\theta)$ above the second angle in the plane formed by the normal vector pointing from the first atom to the second atom.

While the placement of the first three atoms all involve a fair amount of freedom, the actual relative arrangement of these atoms are not unique. Any set of valid positions for the above three atoms can be mapped into another set of valid positions through translations and 3D rotations. The fourth atom, however, with the dihedral angle added as a constraint, breaks the degeneracy of the three atom arrangement. For a given dihedral angle there are at most two positions for the fourth atom (if the dihedral angle is 0 or π there is only one position, obviously).

For the following derivation I will assume that the position of the first three atoms, denoted by $\vec{R}_1$, $\vec{R}_2$, and $\vec{R}_3$, are known, and the position of the fourth atom $\vec{R}_4$ is unknown (see Figure C.1). To make the notation more convenient, the following relative vectors will be used:

$$\begin{aligned}
\vec{r}_1 &= \vec{R}_1 - \vec{R}_0 \\
&= x_1\hat{i} + y_1\hat{j} + z_1\hat{k} \\
\vec{r}_2 &= \vec{R}_1 - \vec{R}_0 \\
&= x_2\hat{i} + y_2\hat{j} + z_2\hat{k} \\
\vec{r}_3 &= \vec{R}_3 - \vec{R}_2 \\
&= x_3\hat{i} + y_3\hat{j} + z_3\hat{k}
\end{aligned}$$

I am therefore solving for $\vec{r}_3$. To make this derivation more general, I assume that the bond lengths and bond angles are not necessarily constant. We therefore have:

$$\begin{aligned}
|\vec{r}_1| &= b_1 \\
|\vec{r}_2| &= b_2 \\
\vec{r}_1 \cdot \vec{r}_2 &= -b_1 b_2 \cos\theta_1
\end{aligned}$$

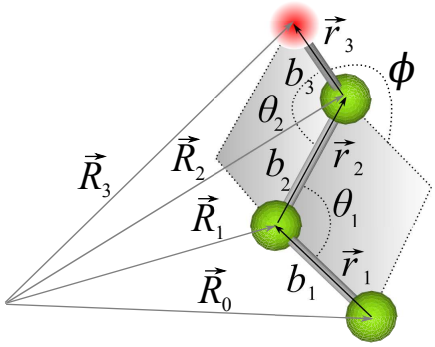

Figure C.1: A pictorial representation of the variables used in the following derivation. We assume that the locations ($\vec{R}_1$, $\vec{R}_2$, $\vec{R}_3$) of the three green atoms are known. The fourth atom, shown in red, is at an unknown position $\vec{R}_4$, however we do know the bond lengths b_i, bond angles θ_i, and the dihedral angle ϕ.

The final bond length b_3, bond angle θ_2, and dihedral angle ϕ are known values. The possible values for $\vec{r}_3$ are therefore solutions to the following equations:

$$|\vec{r}_3| = b_3 \tag{C.1}$$

$$\vec{r}_2 \cdot \vec{r}_3 = -b_2 b_3 \cos\theta_2 \tag{C.2}$$

$$(\vec{r}_1 \times \vec{r}_2) \cdot (\vec{r}_3 \times \vec{r}_2) = -b_1 b_2^2 b_3 \sin\theta_1 \sin\theta_2 \cos\phi \tag{C.3}$$

Expanding Equation C.3 in terms of Cartesian coordinates yields:

$$\begin{aligned}
\vec{r}_1 \times \vec{r}_2 &= (y_1 z_2 - z_1 y_2)\,\hat{i} + (z_1 x_2 - x_1 z_2)\,\hat{j} + (x_1 y_2 - y_1 x_2)\,\hat{k} \\
\vec{r}_3 \times \vec{r}_2 &= (z_2 y_3 - y_2 z_3)\,\hat{i} + (x_2 z_3 - z_2 x_3)\,\hat{j} + (y_2 x_3 - x_2 y_3)\,\hat{k} \\
(\vec{r}_1 \times \vec{r}_2) \cdot (\vec{r}_3 \times \vec{r}_2) &= y_1 z_2^2 y_3 - y_1 y_2 z_2 z_3 - z_1 z_2 y_2 y_3 + z_1 y_2^2 z_3 \\
&\quad + z_1 x_2^2 z_3 - z_1 z_2 x_2 x_3 - x_1 x_2 z_2 z_3 + x_1 z_2^2 x_3 \\
&\quad + x_1 y_2^2 x_3 - x_1 x_2 y_2 y_3 - y_1 y_2 x_2 x_3 + y_1 x_2^2 y_3 \\
&= \left(x_1\left(y_2^2 + z_2^2\right) - x_2\left(y_1 y_2 + z_1 z_2\right)\right) x_3 \\
&\quad + \left(y_1\left(x_2^2 + z_2^2\right) - y_2\left(x_1 x_2 + z_1 z_2\right)\right) y_3 \\
&\quad + \left(z_1\left(x_2^2 + y_2^2\right) - z_2\left(x_1 x_2 + y_1 y_2\right)\right) z_3 \\
&= \left(x_1\left(b_2^2 - x_2^2\right) + x_2\left(b_1 b_2 \cos\theta_1 + x_1 x_2\right)\right) x_3 \\
&\quad + \left(y_1\left(b_2^2 - y_2^2\right) + y_2\left(b_1 b_2 \cos\theta_1 + y_1 y_2\right)\right) y_3 \\
&\quad + \left(z_1\left(b_2^2 - z_2^2\right) + z_2\left(b_1 b_2 \cos\theta_1 + z_1 z_2\right)\right) z_3 \\
&= \left(b_2^2 x_1 + b_1 b_2 \cos\theta_1 x_2\right) x_3 + \left(b_2^2 y_1 + b_1 b_2 \cos\theta_1 y_2\right) y_3 \\
&\quad + \left(b_2^2 z_1 + b_1 b_2 \cos\theta_1 z_2\right) z_3
\end{aligned}$$

Using Equation C.2 we define x_3 as the following:

$$x_3 = -\frac{b_1 b_2}{x_3}\cos\theta_2 - \frac{y_2}{x_2}y_3 - \frac{z_2}{x_2}z_3 \tag{C.4}$$

We therefore have:

$$\begin{aligned}
-b_1 b_2^2 b_3 \sin\theta_1 \sin\theta_2 \cos\phi =& -\left(b_2^2 x_1 + b_1 b_2 \cos\theta_1 x_2\right)\left(\frac{b_1 b_2}{x_3}\cos\theta_2 + \frac{y_2}{x_2}y_3 + \frac{z_2}{x_2}z_3\right) \\
&+ \left(b_2^2 y_1 + b_1 b_2 \cos\theta_1 y_2\right) y_3 \\
&+ \left(b_2^2 z_1 + b_1 b_2 \cos\theta_1 z_2\right) z_3 \\
-b_1 b_2^2 b_3 \sin\theta_1 \sin\theta_2 \cos\phi x_2 =& -b_2^3 b_2 \cos\theta_2 x_1 - b_2^2 x_1 y_2 y_3 - b_2^2 x_1 z_2 z_3 \\
&- b_1 b_2^2 b_3 \cos\theta_1 \cos\theta_2 x_2 - b_1 b_2 \cos\theta_1 x_2 y_2 y_3 \\
&- b_1 b_2 \cos\theta_1 x_2 z_2 z_3 + b_2^2 y_1 x_2 y_3 \\
&+ b_1 b_2 \cos\theta_1 x_2 y_2 y_3 + b_2^2 z_1 x_2 z_3 + b_1 b_2 \cos\theta_1 x_2 z_2 z_3 \\
\left(y_1 x_2 - x_1 y_2\right) y_3 + \left(z_1 x_2 - x_1 z_2\right) z_3 =& \left(b_1 b_3 \left(\cos\theta_1 \cos\theta_2 - \sin\theta_1 \sin\theta_2 \cos\phi\right) x_2 + b_2 b_3 \cos\theta_2 x_1\right)
\end{aligned}$$

We then define y_3 as the following;

$$\begin{aligned}
y_3 =& \left(\frac{b_1 b_3 \left(\cos\theta_1 \cos\theta_2 - \sin\theta_1 \sin\theta_2 \cos\phi\right) x_2 + b_2 b_3 \cos\theta_2 x_1}{y_1 x_2 - x_1 y_2}\right) + \left(\frac{x_1 z_2 - z_1 x_2}{y_1 x_2 - x_1 y_2}\right) z_3 \\
=& c_3 + c_4 z_3 \ ,
\end{aligned} \tag{C.5}$$

and use Equations C.4 and C.5 to define x_3 as the following:

$$\begin{aligned}
x_3 =& \left(\frac{b_1 b_3 \left(\sin\theta_1 \sin\theta_2 \cos\phi - \cos\theta_1 \cos\theta_2\right) y_2 - b_2 b_3 \cos\theta_2 y_1}{y_1 x_2 - x_1 y_2}\right) + \left(\frac{z_1 y_2 - y_1 z_2}{y_1 x_2 - x_1 y_2}\right) z_3 \\
=& c_1 + c_2 z_3
\end{aligned} \tag{C.6}$$

Substituting Equations C.5 and C.6 into Equation C.1, we have:

$$\begin{aligned}
b_3^2 &= \left(c_1 + c_2 z_3\right)^2 + \left(c_3 + c_4 z_3\right)^2 + z_3^2 \\
z_3 &= -\left(\frac{c_1 c_2 + c_3 c_4}{c_2^2 + c_4^2 + 1}\right) \pm \sqrt{\left(\frac{c_1 c_2 + c_3 c_4}{c_2^2 + c_4^2 + 1}\right)^2 - \frac{c_1^2 + c_3^2 - b_3^2}{c_2^2 + c_4^2 + 1}}
\end{aligned} \tag{C.7}$$

In Equation C.7 the choice of plus or minus in the expression for z_3 determines the "sign" of the dihedral angle. If the sign is chosen consistently as plus (or minus) a helical chain-like structure will be generated, if the sign is alternated than an approximation of a ring structure will be generated (if the bond lengths, bond angles, and dihedral angles of tSe are used the ninth atom in the ring will almost completely, but not perfectly, overlap the position of the first atom).

Note that the definition used in Equation C.4 requires $x_2 \neq 0$. Since the equations are symmetric under exchange of x, y, z, if $x_2 = 0$ the above expressions can still be used simply by swapping the variables as appropriate. Obviously for a non-zero bond length at least one of the components of $\vec{r}_2$ will be greater than zero, so the above method is not exclusive to a particular geometry.